Effect of swift heavy ions irradiation on the migration behaviour of xenon implanted into spark plasma sintered titanium nitride and titanium carbide

by

Henry Apele Vasco

Submitted in partial fulfilment of the requirements for the degree of

DOCTOR OF PHILOSOPHY (PhD) IN PHYSICS

In the Faculty of Natural and Agricultural Sciences at University of Pretoria

April…….2021

Supervisor: Prof T.T Hlatshwayo

Co- supervisor: Dr. M. Mlambo

DECLARATION

I, Henry Apele Vasco, declare that the thesis which I hereby submit for the degree of PhD in University of Pretoria, is my own work and has not been submitted by for a degree at this or any other tertiary institution.

Signature: …….

Date: …….

SUMMARY

Owing to their superior properties, TiN and TiC have been proposed as potential fuel cladding materials for the proposed generation IV (Gen IV) nuclear energy systems. In this application they will be exposed to irradiation at elevated temperatures and should be able to retain fission products under these conditions. Xenon -135 is an unstable isotope of xenon (Xe) with a half-life of 9.2 hours and is one of the abundant fission products (FPs) of uranium in the nuclear reactor. About 5% of ^{135}Xe is produced as FP, while 95% comes from Iodine- 135 decay. Hence its migration into fuel cladding material is vital for the success of the proposed reactors. Some investigations have been carried out on the radiation tolerance and migration behaviour of Xenon in TiN and TiC. To get more insight in the migration behaviour of Xe in TiN and TiC, the influence of irradiation needs to be understood. In this study, the effect of swift heavy ion (SHI) irradiation in the migration behaviour of Xe implanted into spark plasma sintered TiN and TiC was investigated. TiN and TiC powders were sintered by spark plasma sintering (SPS) at 1900 °C. Some of the as-sintered samples were implanted with Xe-360 keV ions to a fluence of 1.1×10^{16} cm^{-2} at room temperature (RT), and others were first irradiated with Xe-167 MeV ions to a fluence of 3.4×10^{14} cm^{-2} at RT then implanted with Xe-360 keV ions to a fluence of 1.1×10^{16} cm^{-2} also at RT. Both implanted and irradiated then implanted samples were isochronally annealed at temperatures ranging from 1100-1600 °C in steps of 100 °C for 5 hours under vacuum. Raman spectroscopy (RS), X-ray photoelectron spectroscopy (XPS), scanning electron microscopy (SEM) and X-ray diffraction (XRD) were used to characterize the as-sintered samples while the implanted and the irradiated then implanted and annealed samples were additionally characterised by Rutherford backscattering spectrometry (RBS). SEM and XRD confirmed the successful sintering of the powders while RS and XPS revealed that the as-sintered TiC and TiN had vacancies (Frenkel defects) and had oxidized on the surface.

.

Both implantation and irradiation then implantation caused no amorphization of TiN and TiC samples. Annealing caused progressive annealing of defects in both TiN and TiC samples.

Migration of implanted Xe in TiN was governed by trapping and de-trapping of implanted Xe through defects in the implanted samples annealed at the temperatures below 1200 °C and was mainly through grain boundary diffusion towards the surface accompanied by loss at temperatures above 1200 °C. About 90% of implanted Xe was lost after annealing at 1600 °C. In the irradiated then implanted samples, the migration of Xe was mainly via fast grain boundary diffusion towards the surface accompanied by a loss at all annealing temperatures. Almost all implanted Xe was lost after annealing at 1600 °C. The diffusion of Xe in the implanted TiN samples was measured at temperatures ranging from 1100 to 1400 °C and yielded to an activation energy of $Ea = (2.2 \pm 0.5) \times 10^{-19}$ J = 1.4 eV and pre-exponential factor of $D_o = (1.4 \pm 0.5) \times 10^{-16}$ m^2/s.

The migration of implanted Xe was governed by trapping and de-trapping of implanted Xe through defects in the implanted TiC samples at annealing temperature below 1200 °C and a fast grain boundary diffusion towards the surface accompanied by loss at temperatures above 1200 °C. About 75% of implanted Xe was lost after annealing at 1600 °C. In the irradiated then implanted TiC samples, the migration of implanted Xe was due to grain boundary diffusion towards the surface accompanied by the loss throughout the annealing process. About 60% of implanted Xe was lost after annealing at 1600 °C. The diffusion of Xe in the implanted and irradiated then implanted TiC samples were determined at temperatures ranging from 1200 to 1500 °C and yielded to an activation energy of 1.4 eV and pre-exponential factor (D_o) of 5.2×10^{-17} m^2s^{-1} for implanted TiC and 1.6 eV and 5.2×10^{-16} m^2s^{-1} irradiated then implanted TiC.

ACKOWLEDGEMENTS

I would like to acknowledge the following people for their support and valuable contribution in the success of my study.

- My academic promoter, Prof. T.T. Hlatshwayo his tolerance, guidance, support, discussion during this study.
- My co- promoter Dr. M. Mlambo his tolerance, guidance, support, discussion during this study.
- Fellow students in the Physics department for all their help, encouragement, and moral support.
- My family for their endless love, support and encouragement throughout my studies and life.
- The financial support of the NRF is hereby acknowledged

TABLE OF CONTENTS

LIST OF FIGURES

LIST OF TABLES

LIST OF ABBREVIATIONS.

BSE - Backscattered Electrons

CCD- Charge Coupled Device

FEG - Field Emission Gun

FWHM- Full Width at Half Maximum

GFR - Gas Cooled Fast Reactor

GIF - Generation IV International Forum

ICDD - International Centre for Diffraction Data

LFR - Lead Cooled Fast Reactor

MCA - Multi-Channel Analyser

MSR - Molten Salt Cooled Reactor

RBS- Rutherford Backscattering Spectrometry

RS - Raman Spectroscopy

SE- Secondary Electrons

SEM- Scanning Electron Microscopy

SHI – Swift Heavy Ion

SRIM- Stopping and Range of Ions in Matter

XPS - X-ray Photoelectron Spectroscopy

XRD - X-Ray Diffraction

Chapter one

1. Introduction

1.1 Motivation for Generation IV nuclear reactors

The world is in energy crisis with the world's population approaching 10 billion in the next few years. There is need for production of more energy to sustain the fast-growing population. In the quest to produce more energy there are several challenges encountered, these includes the use of fossil fuels (oil and coal) which always comes at a price [1]. The use of fossil fuels as a source of energy has proven to be the main contributor to global warming. Therefore, the need for alternative methods of producing energy while emitting less/no greenhouse gases thus alleviating the problem of global warming is inevitable.

There are several forms of reliable sources of energy with no or less greenhouses gases emission that can be explored. These include solar, wind, hydro, bio and nuclear energy to mention a few. Out of these, prominent form of energy is nuclear energy. However, safety and nuclear waste storage have made it unpopular. Nuclear waste management is a major problem facing the nuclear power industry, due to its radiotoxicity that poses health hazard to the communities living near nuclear power plants during accident. For decades nuclear power plants have been supplying energy to many countries all over the globe [1]. The current fleet of nuclear power plants are about to reach their life span which usually is around 60 years and therefore there is a need to improve on the safety and reliability, efficiency, sustainability, and proliferation resistance. Due to hesitations about the future of nuclear power plants (Generation III nuclear power plants (1990-2010)) in the aftermath of the Fukushima Daiichi (Generation II (1970-1990)) accident has also added to challenges facing the current fleet as far as safety and reliability are concerned [2].

To address the safety and nuclear waste problems, 9 countries (namely Argentina, Brazil, Canada, France, Japan, the Republic of South Korea, the Republic of South Africa, the United

States of America and the United Kingdom) formed the Generation IV international Forum (GIF) to develop future nuclear energy systems in the year 2000. Generation IV nuclear energy systems comprise of a nuclear reactor and their energy conversion systems, including the fuel cycle extraction of waste disposal. GIF currently has 13 members, all of which are signatories of its founding document-the GIF Charter. It was subsequently signed by Switzerland in 2002, Euratom in 2003, and the People's Republic of China and Russian Federation in 2006. The main goals of GIF chatter are sustainability, safety and reliability, economics and proliferation resistance-physical protection. Sustainability focuses on generating energy sustainably, promoting long-term availability of nuclear fuel, minimising nuclear waste and reduce the long-term stewardship burden. Safety and reliability ensure a very low likelihood and degree of reactor core damage and eliminating the need for offsite emergency response. Economics focuses on having a life cycle cost advantage over other energy sources and having a level of financial risk comparable to other energy projects. Lastly proliferation resistance and physical protection focus on finding a very unattractive route for diversion or theft of weapon-usable materials and providing an increase in physical protection against acts of terrorism.

The first nuclear power station started operating about 70 years ago, and since then there has been challenges regarding the fleet that has been deployed, some of them have reached their life span. Table 1-1 shows the evolution of nuclear reactors including the proposed generation IV reactors.

Table 1-1: *Generations of nuclear reactors [2].*

	Generation I	Generation II	Generation III	Generation III+	Generation IV
Period of deployment	**1950-1960**	**1970-1990**	**1990-2010**	**After 2020**	**After 2030**
Examples	Shipping port, Dresden, Magnox	PWR and VVER, BWR, CANDU	ABWR, AES-92 AP1000, EPR		• Life-cycle economic advantage • Enhanced safety • Minimal waste • Proliferation resistant -
Comments	Early prototype Reactors	Large commercial power plants that are still operating	Advanced LWR	Evolutionary Designs offering economic and safety Features	
			One indication of being part of Generation III/III+ is certification by EUR (in Europe) or EPRI/URD (in the United States)		

1.2 The Technology Roadmap

The Technology Roadmap (2002), defined and planned the necessary Research and Development and associated timelines to achieve these goals and allow deployment of Generation IV energy systems after 2030. This road mapping exercise was a two-year effort by more than 100 international experts to select the most promising nuclear systems. In 2002, GIF selected six systems from nearly 100 concepts, as Generation IV systems. These are gas-cooled fast reactor (GFR), lead-cooled fast reactor (LFR), molten salt reactor (MSR) supercritical-water-cooled reactor (SCWR) and very-high-temperature reactor (VHTR).

The GFR system is a high-temperature helium-cooled fast-spectrum reactor with a closed fuel cycle. It combines the advantages of fast-spectrum systems for long-term sustainability of uranium resources and waste minimization. The advantages of the gas coolant are that it is chemically inert (allowing high temperature operation without corrosion and coolant radiotoxicity) and single phase (eliminating boiling), and it has low neutron moderation [1]. LFRs are Pb or Pb-Bi-alloy-cooled reactors operating at atmospheric pressure and at very high temperatures because of the very high boiling point of the coolant (up to 1743 °C). The core is characterized by a fast-neutron spectrum due to the scattering properties of lead [1].

The MSR is a class of nuclear fission reactors in which the primary coolant, or even the fuel itself, is a molten salt mixture. MSRs run at higher temperatures than water-cooled reactors for higher thermodynamic efficiency, while staying at low vapour pressure, liquid fuelled MSR has been focused on epithermal to thermal neutron spectrum [1].

The SFR is a Generation IV reactor project to design an advanced fast neutron reactor with the objective of producing a fast-spectrum, liquid sodium-cooled reactor. It allows a low-pressure coolant system and high-power-density operation with low coolant volume fraction in the core [1]. The SCWR is a high temperature, high-pressure, light water reactor that operates above the thermodynamic critical point of water (374°C, 22.1 MPa). The reactor core may have a

thermal or a fast-neutron spectrum, depending on the core design [1]. The VHTR is a next step in the evolutionary development of high-temperature gas-cooled reactors. It is a graphite-moderated, helium-cooled reactor with thermal neutron spectrum [1].

Among these selected Generation IV systems, the use of advanced nuclear ceramics or refractory ceramics as potential cladding materials has only been considered for GFR, SFR and VHTR [3].

Identification of a specific fuel type and fuel element/fuel assembly that is compatible with gas-cooled fast reactor GFR in-core service conditions is a key part of the overall goal of developing a practical version of a gas-cooled fast reactor. Current gas reactor fuel technology is not adaptable to a gas-cooled fast reactor. The categories of fuel with the highest potential for success are carbide and nitride-based composite-type fuels. These fuels consist of a fissile phase dispersed within a refractory matrix. The most promising candidates for GFR fuel matrix materials are ZrN, ZrC, TiN, TiC, and SiC. This is due to a combination of neutronic performance, thermal properties, chemical behaviour, crystal structure, and physical properties of these ceramics. These advanced ceramics are also considered as potential cladding material for SFR. Normally, an advanced BISO (Bistructural-isotropic) fuel particle is considered for GFRs. This type of fuel form has a fuel kernel and two ceramic outer layers. The central kernel consists of a spherical fuel particle (consists of UC or UN) surrounded by a ceramic coating (TiC, ZrC, TiN, ZrN or SiC) which provides structural integrity and containment of fission products. In between the coating and the fuel, there is a buffer layer, which is also supposed to be made of low density (TiC, ZrC, TiN, ZrN or SiC). Buffer allows for changes in thermal expansion, swelling, and fission gas release pressure without creating an unacceptable amount of stress on the outer containment coating [4].

The buffer layer is porous to reduce its stiffness and the resulting pressure on the coating and to accommodate released fission gases. It is composed of the same material as the coating. The

use of the same material for the buffer and coating reduces expansion mismatch and less chance of chemical incompatibilities. These advanced BISO fuel particle can be utilized by placing them in a ceramic matrix composed of the same material as the BISO fuel particles' outer ceramic coating. With this design, there is only one major interface of different materials: the fuel and the buffer. The typical cross-sectional schematic diagram of BISO fuel is shown in Figure. 1-1

The new BISO micro fuel particle materials must meet a variety of criteria. Coatings with significant neutron absorption cross-sections cannot be used, thus excluding many candidates. The potential coatings must have high melting points (excess of 2000 °C), adequate thermal conductivity (>10 W/m-K) and toughness (>12 MPa-$m^{1/2}$), and acceptable response to high dose neutron damage (swelling <2 % over service life (~80 dpa)). Thus, the categories of materials with the highest potential for success for the GFR are carbides and nitrides based ceramics [4,5].

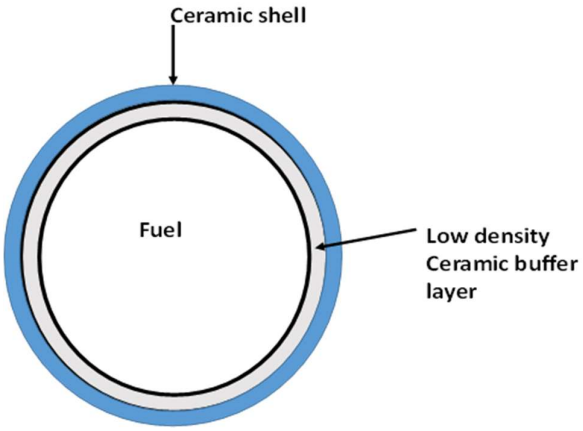

Figure.1-1: A *typical cross-sectional of BISO particle*.

Table 1-2: *Physical and electrical properties of Xenon.*

Atomic radius	1080 pm
Melting point	-111.75 °C
Boiling point	-1080.01 °C
Specific heat	158.32 J/(kg-K)
Thermal conductivity (25 °C)	5.65×10^{-3} W/(m-k)
Coefficient of thermal expansion (25 °C)	N/A
Electricity resistivity	N/A

1.3 Properties of Titanium Carbides and Nitrides

TiN and TiC are transition metal ceramics (group IV carbides and nitrides), they form a NaCl like structure or face-centred cubic *(fcc)* that provides octahedral sites large enough to be occupied by C and N atoms to form a stable compound. These compounds are also called interstitial carbide or nitrides due to the fact the C or N atoms occupy the interstitial sites. A typical NaCl structure is shown in Figure 1-2.

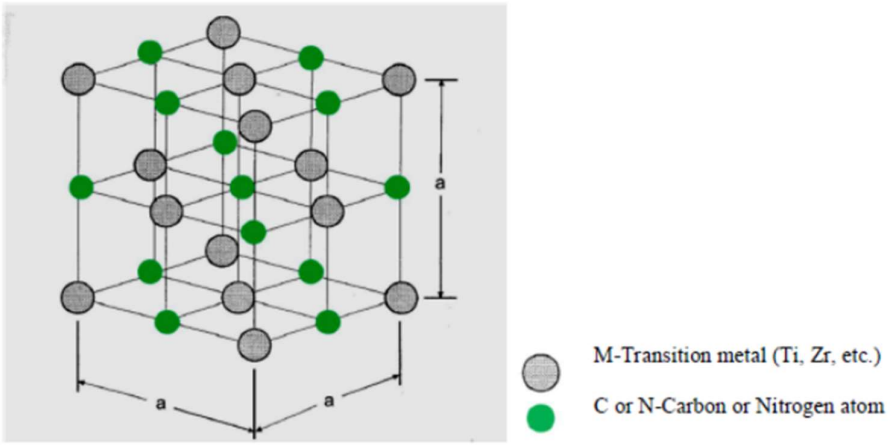

Figure 1-2: *A typical NaCl structure of transition metal carbide or nitride. Taken from [6].*

Theoretically $MC_{1.0}$ or $MN_{1.0}$ is expected, at stoichiometry that is 100 % occupancy of the sites, which is not always the case [8]. There are always vacancies that exists within the lattice which result into non-stoichiometry of the M/C or M/N ratio. These vacancies play an important role when it comes to some of the important properties of these ceramics, such mechanical, thermodynamic, electronic and magnetic properties.

The nitrogen or carbon atoms in interstitial nitrides or carbides are considered as isolated atoms nesting in a large complex structure of transition metal. In these arrangements there are no C-C or N-N bonds because there is not enough space to form interatomic bonds. The only bonds that exists are M-N, M-C and M-M bonds [8]. These bonds combine the following types of bonding:

i) Metallic bonding with finite density of states at the Fermi-energy level, E_f.

ii) Ionic bonding resulting from the transfer of electrons to the nitrogen or carbon from the metal atom.

iii) Covalent bonding between the d state from the metal and the p-states of carbon/ nitrogen, with some metal to metal interaction.

Due to this complex bonding transition metal carbides and nitrides have a unique array of properties over other ceramics.

1.3.1 Properties of TiN and TiC suitable for Gen IV reactor applications

The most important properties that qualifies TiN and TiC to be used in the Gen IV reactors are: high melting point (> 2000 °C), thermal conductivity (> 10 M/mk relatively high), toughness (> 12 MPa-$m^{1/2}$) and high tolerance to high neutron dose (swelling < 2 % over service life (about 80 dpa)) [7].

i) High melting temperature: TiN and TiC have high melting temperature compared to other ceramics hence they meet the requirements for cladding matrix

in the proposed Gen IV nuclear reactors. Table 1-3 compares the melting point of TiN, TiC and SiC.

Table 1-3: *Melting points of TiN, TiC and SiC*

Compound (ceramic)	**Temperature (°C)**
TiN	2950
TiC	3067
SiC	2730

ii) **Thermal conductivity**: Thermal conductivity k is the rate of heat transfer by conduction. Figure 1-3 shows the thermal conductivity of different carbides and nitrides as a function of temperature. Both TiC and TiN have higher thermal conductivity compared to other nitrides and carbides over the temperature range as seen in Figure 1-3. Their thermal conductivities increase with increase in temperature which is a good property for nuclear reactor application where these ceramics will be exposed to high temperatures and should be able to release heat faster [6].

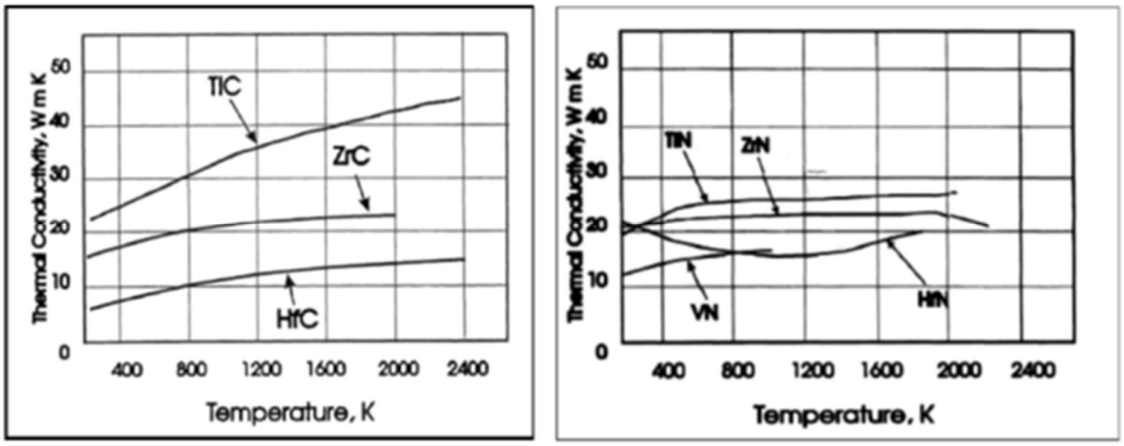

Figure 1-3: *Thermal conductivity of carbides and nitrides of transition metals. Taken from [6].*

iii) Hardness

Figure 1-4 shows the hardness of different carbides as function of temperature. Among these carbides, TiC is initially the hardest at 0 °C and its hardness decreases with increasing temperature. This indicates that TiC will withstand stress in high temperature environment. TiN and TiC are interstitial nitrides/carbides therefore their properties are similar. Hence, it'sworth mentioning that the two are isomorphs which means they almost behave in a similar behaviour under similar conditions. TiN is also a very hard ceramic with Vickers hardness of about 18 ~ 21 GPa. Therefore, it can be inferred from its isomorph that its hardness decreases with increasing temperature [7].

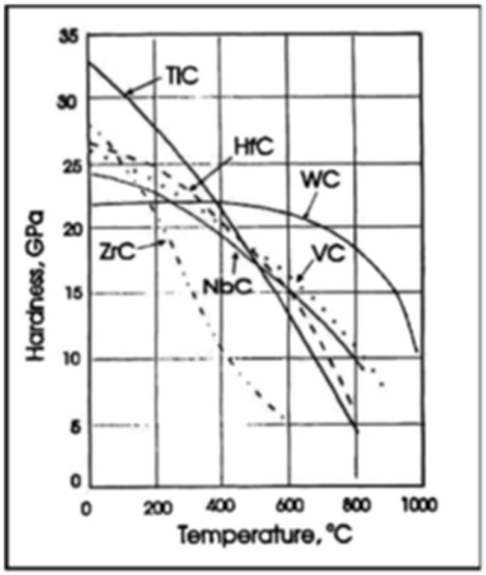

Figure 1-4: *The hardness of carbides as a function of temperature. Taken from [7].*

iv) Variation of properties with M-X ratio (M: Ti and X: C or N)

TiN and TiC are isomorphs, they can form solid solutions, and form TiCN which behaves comparably well with both TiN and TiC. It is not surprising that transition metal carbides and nitrides are stable on a wide range of stoichiometric ratios and exhibit almost the same behaviour under ion irradiation [7]. This due to their large number of vacancies and conservation of their structure.

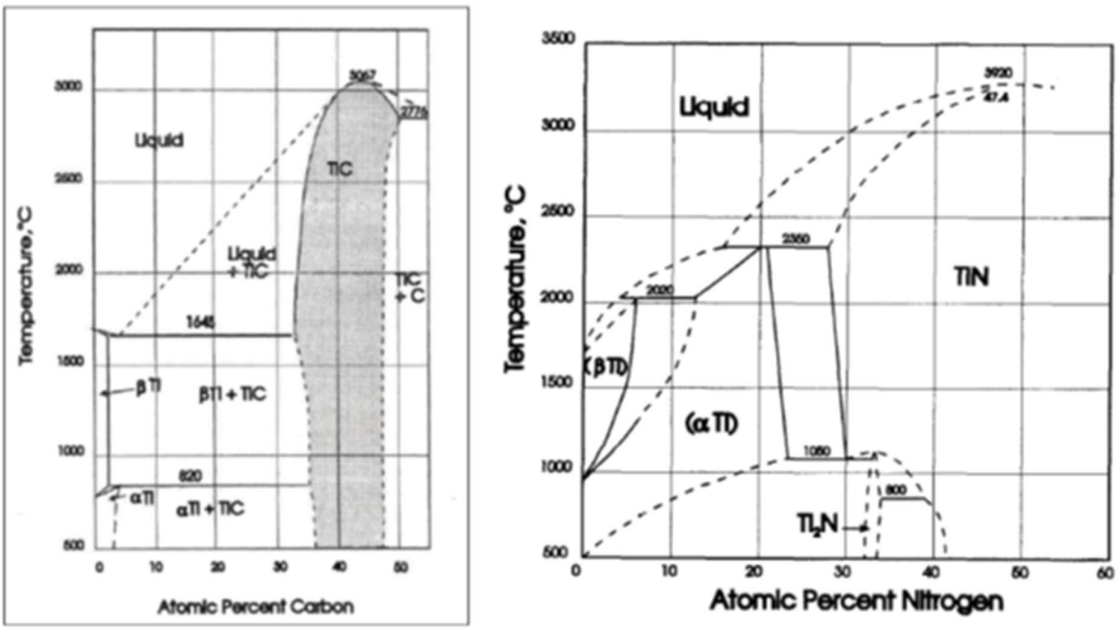

Figure 1-5: *The phase diagrams of TiC and TiN. Taken from [6].*

Figure 1-5 shows the phase diagrams of TiC and TiN, respectively. The extensive homogeneity range of TiC is the shaded part of the diagram. TiC is considered as defect structures due to wide range of stable compositions. TiN, just like TiC is also stable over a wide range of stoichiometry between 0.6 and 1.2. The equilibrium solid phases of the TiN system are the terminal hexagonal close packed (hcp) solid solution (α Ti), based on titanium below 882 °C, with a wide range of compositions. The terminal body centred cubic (bcc) solid solution (βTi), based on titanium above 882 °C, with a wide range of compositions and the tetragonal Ti_2N phase also referred to as the ε phase and the face-centered cubic also referred to as the δ phase [7].

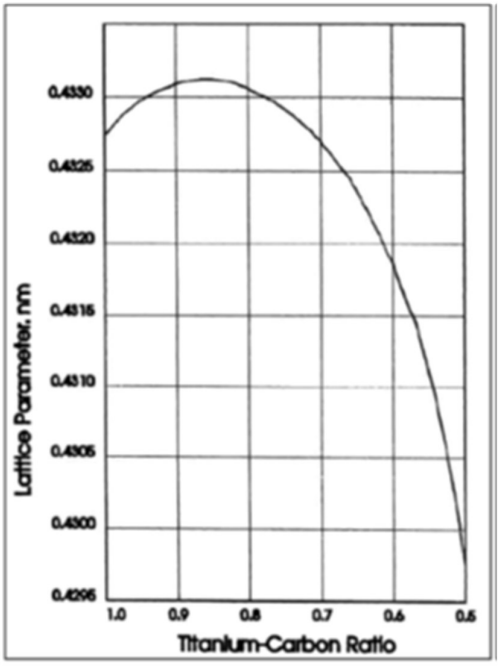

Figure 1-6: *Lattice parameter as a function of titanium – carbon ratio. Taken from [6].*

Figure 1-6 shows the variation of the lattice constant with Ti-C ratio for TiC. From the graph it can be deduced that the highest value of lattice parameter is at titanium-carbon ratio of approximately 0.85 and it should be noted that this is where the melting point is the highest. Since TiC is an isomorph to TiN the same conclusions drawn for TiC can be extended to TiN [6].

1.4 Previous studies

For successful use of TiC and TiN in GRFs their irradiation response and migration of important fission products need to be understood. This section discusses the investigations that have been done on TiN and TiC.

1.4.1 Previous studies on TiN

Irradiation response of TiN, ZrC and SiC was investigated by Weaver *et al.* [8]. TiN, ZrC and SiC were irradiated with 1MeV Kr ions to 10 and 70 dpa at 800 °C. The lattice parameter of TiN expanded by up to 2 % while that of ZrC expanded by 7 % after irradiation to 70 dpa at 800 °C by 1 MeV krypton ions. No changes were observed in SiC under the same irradiation conditions. This was due to recrystallization of SiC at high irradiation temperatures [8].

Wang *et al*. [9] investigated the microstructure of polycrystalline TiN thin films irradiated with ^{4}He ions at room temperature to a fluence of 1×10^{17} cm^{-2}. The authors observed that the grain boundaries, which are abundant in nanocrystals, acted as sinks for radiation induced Frenkel pairs, providing pathways for diffusion and annihilation, thus suggesting a certain degree of radiation tolerance.

Gavarini *et al.* [10] implanted 800 keV Xe ions into sintered TiN to a fluence of 5×10^{15} cm^{-2}. Post annealing at temperatures from1400 to 1650 °C for 1 and 3 hours resulted in the migration behaviour corresponding to a gas migration model dominated by surface directed transport, with a slight diffusion component.

The radiation performance of TiN films under Ar ion irradiation at room temperature has also been studied by Popovic *et al.* [11]. 120 keV Ar irradiation caused a decrease of the lattice parameter of TiN crystals from 0.427 to 0.423 nm which resulted in an increase of the strain in the film layer at fluences of 1×10^{16} cm^{-2}.

Popovic *et al.* [12] also investigated the microstructural properties of TiN/Si bilayers by irradiating with 200 keV Ar ions to a fluences of 5×10^{15} and 2×10^{16} cm^{-2}. The irradiations caused the microstructural changes in the TiN films but no amorphization up to the highest fluence of 2×10^{16} cm^{-2}. The decrease in mean crystallite size with increasing fluence was also observed.

In yet another study Popovic *et al.* [13] irradiated polycrystalline TiN with 80 keV V ions to fluences of 2×10^{15} cm^{-2} and with 200 keV Ar ions to a fluence between 5×10^{15} and 2×10^{16} cm^{-2} at RT. The variation of the electric and optical resistivity with irradiation was deduced.

Bes *et al.* [14] implanted sintered TiN with 800 keV Xe ions to a fluence of 5×10^{15} cm^{-2} at RT and were annealed at 1500 °C for 5 hours. The role of microstructure on the release of the implanted Xe and the crystalline orientation of each grain was identified as a key parameter in the morphological evolutions of the surface during annealing.

Uglov *et al*. [15] reported that small Zr additions into the TiN may increase its structural stability under heavy ion irradiation, but no post-irradiation microstructure analysis was performed by the authors.

Gavarini *et al.* [16] irradiated dense microstructures of TiN with 800 keV Xe ions to a fluence of $5\times10^{15}cm^{-2}$ at RT. Isothermal treatments were performed at temperature of 1500 °C for 1 hour, under several oxygen partial pressures between 10^{6} to 2×10^{-6} mbars. The results revealed that TiN showed the progressive apparition of oxides was corelated to the release of Xe. A correlation between the initial fine microstructure of TiN and the growing layer was suggested.

Xue et al. [17] observed dislocations and bubbles when TiN was irradiated with 100 keV Ar ions at 600 °C to a fluence of 3×10^{17} cm^{-2}. A slight expansion of the lattice parameter of 0.19 % was also observed Bubbles and dislocations were also observed. The expansion in lattice parameter could be attributed to the higher implantation temperature, as compared to RT implantation performed by Popovic *et al*. they observed a contraction in lattice parameter. In addition, RT implantation produces more disorder as compared to higher temperature implantation.

Bes *et al.* [18] irradiated sintered TiN with 800 keV Xe ion at fluence of 5×10^{15} cm^{-2} at RT followed by post annealing at temperatures from 1300 to 1500 °C. The results revealed that Xe concentration of about 0.4 at. % was sufficient to form bubbles in the TiN matrix. Xe massive release due to Xe interconnected bubble network was observed.

Xue *et al*. [19] irradiated TiN and $TiN_{0.07}$ using 100 keV Ar ion beam at 600 °C to a fluence of 3×10^{17} cm^{-2} at 600 °C. The results revealed the expansion of the lattice parameter for TiN sample while non-stoichiometric TiN revealed the shrinking of the lattice parameter.

Popovic *et al.* [20] irradiated TiN thin films with 400 keV Xe up to 2×10^{16} cm^{-2} at room temperature. XRD analysis of irradiated films exhibited a split in the (111) reflection indicating both phase transformations as well as contraction of the TiN lattice.

Wang *et al.* [21], irradiated TiSiN and TiN coatings with He ions of 50 keV to a fluence of $1\times10^{17}cm^{-2}$ at RT. The results revealed that TiSiN coating showed better irradiation tolerance than TiN coating, the amorphous interface introduced by Si acted as a defect annihilation could increase the irradiation tolerance of the TiN coating.

Tunes *et al*. [22] recently irradiated thin films of TiN with 134 keV Xe ions to a fluence of 6.5×10^{15} cm^{-2} at 473 K., Irradiation caused the thin films to surfer radiation induced segregation and suffered dislocation due to Xe bubbles.

1.4.2 Previous studies on TiC

Das *et al.* [23] irradiated a (100) $TiC_{0.93}$ thin foil with 100 keV electron beam at room temperature to a dose rate of $10^{19}/cm^2/s$ (0.002 dpa/s) for 215 min. The apparition of both an ordered cubic superstructure $TiC_{0.5}$ and graphite were observed after irradiation.

Hojou *et al.* [24,25] irradiated TiC with low-energy (20 – 25 keV) molecular ion beams of hydrogen and deuterium at temperatures of 12, 18, 28 K at different fluences. Microstructural

changes were monitored by in situ transmission electron microscopy (TEM). Amorphization was only observed for H_2^+ irradiation of 25 keV at fluences of $\sim 10^{17}$ cm^{-2}, while no amorphization was observed for D^{2+} irradiation at 4.5×10^{21} cm^{-2}. This was probably due to the difficulty to create Ti–D and/or C–D bonds while Ti-H and C–H chemical bonds prevented the recovery of irradiation defects, leading to amorphization.

In another work, Hojou *et al*. [26] irradiated TiC (pre- irradiated with 25 keV H_2^+) with 20 keV Helium ions from RT to 1423 K. Simultaneous irradiation of 25 keV H^+ and 20 keV He ion was also conducted. The He ion fluence was varied from 1.5 to 9×10^{17} cm^{-2}. No amorphization was observed under these conditions. Helium bubble formation occurred but the bubble growth was limited to 1–2 nm at RT and 7–8 nm at 1423 K.

TiC together with TiN, SiC, ZrN and ZrC were irradiated with 1 MeV Kr ions to 10 and 70 dpa at 800 °C. The results showed that the lattice parameter of TiC expanded by 2 %. In addition, there were voids in TiC which contributed to 0.01% void swelling were also observed [8].

Dickerson *et al*. [27] irradiated TiC with protons to 0.17, 0.34, and 0.80 dpa and 600 °C, 800 °C, and 900 °C) respectively. TEM was used to study the microstructural evolutions. Unfaulted loops aggregates defects and interstitial Frank-type dislocation loops were also observed. The loop sizes and densities versus temperature suggested an increase of the vacancy mobility above 800 °C due to carbon vacancy reordering in the Ti lattice.

Pellegrino *et al.* irradiated [28] single crystalline of SiC, TiC and ZrC at room temperature with 1.2 MeV of Au ions at 2.8×10^{14} cm^{-2} and 3.3×10^{15} cm^{-2}. SiC amorphized at the lowest fluence of Au ions (2.8×10^{14} cm^{-2}) while TiC and ZrC did not amorphized at the highest fluence of Au ions (3.3×10^{15} cm^{-2}). The lack of amorphization in TiC and ZrC compared to SiC was attributed to the differences in the chemical bonds of TiC and ZrC versus SiC.

Gavarini *et al.* [16] implanted TiC with 800 keV Xe ions to fluence of 5×10^{15} cm^{-2} and then annealed at 1500 °C for 1 hour under several degraded vacuums ranging from Po_2 10^{-6} to $2\times10^{-4}cm^{-2}$mbars. The results showed that TiC is resistant to oxidation and does not release Xe for $\leq 6\times10^{-6}$ mbars. Xe release related to the apparition of the different oxides of Ti at a degraded vacuum of $Po_2 = 2\times10^{-4}$ mbars was observed.

Gavarin *et al.* [29] irradiated the sintered TiC with 500 keV of $^{40}Ar^{+}$ or 800 keV $^{129}Xe^{++}$ to fluence varying from 6×10^{14} to 3.2×10^{17} cm^{-2} either at RT or at 1000 °C. Both Ar and Xe irradiations (at RT) resulted in the formation of microcracks and surface blistering at the highest fluences. The size, shape and the density of the blisters were proposed to depend on the crystallographic orientation of each grain. Ar high temperature (1000 °C) irradiations increased the surface roughness, with complete delamination of extended areas containing large grains and grain boundary abrasion with no blistering.

Quite recently, Pellegrino *et al.* [30], irradiated single crystalline of TiC and ZrC with 1.2 MeV Au ions of fluence ranging from 2×10^{13}-3×10^{16} $ions.cm^{-2}$ and polycrystalline of TiC and ZrC to fluences of between 2×10^{14}-4×10^{15} $ions.cm^{-2}$ at RT. No amorphization at the highest fluence for both carbides was observed, but extended defects like dislocation loops, point defects (vacancies and interstitials) were also observed.

1.5 Scope of the study

In nuclear reactors TiN and TiC will be exposed to a lot of irradiation including ion irradiation of different energies ranging from keV to 100 MeV (the swift heavy ions (SHI) energy regime). When SHIs penetrates solid materials, most of its energy is locally deposited to the electrons and finally transferred to the atoms by electron-electron and electron-atom interactions. These interactions may result in the formation of specific radiation damage the so-called latent tracks [32]. This phenomenon may result in the modification of material structure by changing the

charge state of the defects or annealing due to high intense heating [33]. Under these severe conditions, TiN and TiC must still act as a diffusion barrier to fission products. There is very limited data available on the migration behaviour of Xe in sintered TiN and TiC in literature [14,16–17]. Among these previous studies, the influence of irradiation on the migration behaviour of Xe in TiN and TiC have not been reported. In this study the effect of swift heavy ions irradiation on the migration behaviour of Xe in TiN and TiC. TiN and TiC powders were sintered by spark plasma sintering at temperature of 1900 °C in a vacuum of 100 mbar at 50 MPa maximum pressure. Sets of spark plasma sintered TiN and TiC were firstly irradiated with SHI of 167 MeV to a fluence of 3.4×10^{14} cm^{-2} followed by implantation with Xe ions of 360 keV ions to a fluence of 1.1×10^{16} cm^{-2} at RT. Others were only implanted with Xe 360 keV ions to a fluence of 1.1×10^{16} cm^{-2} at RT. The samples were then isochronally annealed at different temperatures ranging from 1100 °C up to 1600 °C at steps of 100 °C for 5 hours. Structural, and morphological changes of the samples before and after treatments were monitored by X-ray photoelectron spectroscopy (XPS), Raman spectroscopy (RS) and scanning electron microscopy (SEM) while the migration of implanted Xe was monitored by Rutherford backscattering spectrometry (RBS).

The rest of the thesis is organized as follows: Chapter 2 discusses spark plasma sintering (SPS). Chapter 3 discusses the theory of implantation and irradiation Chapter 4 is diffusion, Chapter 5 is the analytical techniques, chapter 6 is TiN results, chapter 7 TiC results and Chapter 8 are conclusions of the study and recommendations for future work.

1.6 References

[1] DoE, U.S., 2002. A technology roadmap for generation IV nuclear energy systems. *http://gif. inel. gov/roadmap/pdfs/gen_iv_roadmap.*

[2] Pioro, I.L., 2016. Introduction: Generation IV International Forum. In *Handbook of generation IV nuclear reactors* (pp. 37-54). Woodhead Publishing.

[3] Meyer, M.K., Fielding, R. and Gan, J., 2007. Fuel development for gas-cooled fast reactors. *Journal of nuclear materials*, *371*(1-3), pp.281-287.

[4] Nosek, A., Conzen, J., Doescher, H., Martin, C. and Blanchard, J., 2007. Thermomechanics of candidate coatings for advanced gas reactor fuels. *Journal of nuclear materials*, *371*(1-3), pp.288-303.

[5] Gan, J., Meyer, M.K., Birtcher, R.C. and Allen, T.R., 2006, January. Microstructure evolution in ZrC irradiated with Kr ions. In *Effects of Radiation on Materials: 22nd Symposium*. ASTM International.

[6] Agarwal, S., Trocellier, P., Serruys, Y., Vaubaillon, S. and Miro, S., 2014. Helium mobility in advanced nuclear ceramics. *Nuclear Instruments and Methods in Physics Research Section B: Beam Interactions with Materials and Atoms*, *327*, pp.117-120.

[7] Pierson, H.O., 1996. *Handbook of refractory carbides & nitrides: properties, characteristics, processing and applications*. William Andrew, pp.100-250.

[8] Gan, J., Yang, Y., Dickson, C. and Allen, T., 2009. Proton irradiation study of GFR candidate ceramics. *Journal of nuclear materials*, *389*(2), pp.317-325.

[9] Wang, H., Araujo, R., Swadener, J.G., Wang, Y.Q., Zhang, X., Fu, E.G. and Cagin, T., 2007. Ion irradiation effects in nanocrystalline TiN coatings. *Nuclear Instruments and*

Methods in Physics Research Section B: Beam Interactions with Materials and Atoms, *261*(1-2), pp.1162-1166.

[10] Gavarini, S., Toulhoat, N., Peaucelle, C., Martin, P., Mende, J., Pipon, Y. and Jaffrezic, H., 2007. Xenon migration behaviour in titanium nitride. *Journal of nuclear materials*, *362*(2-3), pp.364-373.

[11] Popović, M., Novaković, M. and Bibić, N., 2009. Structural characterization of TiN coatings on Si substrates irradiated with Ar ions. *Materials characterization*, *60*(12), pp.1463-1470.

[12] Popović, M., Novaković, M., Šiljegović, M. and Bibić, N., 2012. Effects of 200 keV argon ions irradiation on microstructural properties of titanium nitride films. *Nuclear Instruments and Methods in Physics Research Section B: Beam Interactions with Materials and Atoms*, *279*, pp.144-146.

[13] Popović, M., Novaković, M., Traverse, A., Zhang, K., Bibić, N., Hofsäss, H. and Lieb, K.P., 2013. Modifications of reactively sputtered titanium nitride films by argon and vanadium ion implantation: Microstructural and opto-electric properties. *Thin solid films*, *531*, pp.189-196.

[14] Bes, R., Millard-Pinard, N., Gavarini, S., Cardinal, S., Garnier, V., Khodja, H., Malchere, A., Martin, P. and Peaucelle, C., 2010. Study of xenon thermal migration in sintered titanium nitride using nuclear micro-probe. *Nuclear Instruments and Methods in Physics Research Section B: Beam Interactions with Materials and Atoms*, *268*(11-12), pp.1880-1883.

[15] Uglov, V.V., Rusalski, D.P., Zlotski, S.V., Sevriuk, A.V., Abadias, G., Kislitsin, S.B., Kadyrzhanov, K.K., Gorlachev, I.D. and Dub, S.N., 2010. Stability of Ti–Zr–N

coatings under Xe-ion irradiation. *Surface and Coatings Technology*, *204*(12-13), pp.2095-2098.

[16] Gavarini, S., Bes, R., Millard-Pinard, N., Cardinal, S., Peaucelle, C., Perrat-Mabilon, A., Garnier, V. and Gaillard, C., 2011. A comparative study of TiN and TiC: Oxidation resistance and retention of xenon at high temperature and under degraded vacuum. *Journal of Applied Physics*, *109*(1), p.014906.

[17] Bès, R., Gaillard, C., Millard-Pinard, N., Gavarini, S., Martin, P., Cardinal, S., Esnouf, C., Malchere, A. and Perrat-Mabilon, A., 2013. Xenon behavior in TiN: A coupled XAS/TEM study. *Journal of nuclear materials*, *434*(1-3), pp.56-64.

[18] Xue, J.X., Zhang, G.J., Xu, F.F., Zhang, H.B., Wang, X.G., Peng, S.M. and Long, X.G., 2013. Lattice expansion and microstructure evaluation of Ar ion-irradiated titanium nitride. *Nuclear Instruments and Methods in Physics Research Section B: Beam Interactions with Materials and Atoms*, *308*, pp.62-67.

[19] Xue, J.X., Zhang, G.J., Guo, L.P., Zhang, H.B., Wang, X.G., Zou, J., Peng, S.M. and Long, X.G., 2014. Improved radiation damage tolerance of titanium nitride ceramics by introduction of vacancy defects. *Journal of the European Ceramic Society*, *34*(3), pp.633-639.

[20] Popović, M., Novaković, M., Mitrić, M., Zhang, K., Rakočević, Z. and Bibić, N., 2017. Xenon implantation effects on the structural and optical properties of reactively sputtered titanium nitride thin films. *Materials Research Bulletin*, *91*, pp.36-41.

[21] Wan, Q., Yang, B., Liu, H.D., Mei, Q.S. and Chen, Y.M., 2016. Ion irradiation tolerance of TiSiN nanocomposite coating. *Surface and Coatings Technology*, *305*, pp.165-169.

[22] Tunes, M.A., Da Silva, F.C., Camara, O., Schön, C.G., Sagás, J.C., Fontana, L.C., Donnelly, S.E., Greaves, G. and Edmondson, P.D., 2018. Energetic particle irradiation study of TiN coatings: are these films appropriate for accident tolerant fuels?. *Journal of Nuclear Materials*, *512*, pp.239-245.

[23] Das, G., Chatterjee, D.K. and Lipsitt, H.A., 1981. Electron irradiation damage in TiC. *Journal of Materials Science*, *16*(12), pp.3283-3291.

[24] Hojou, K., Otsu, H., Furuno, S., Sasajima, N. and Izui, K., 1996. In situ observation of damage evolution in TiC during hydrogen and deuterium ion irradiation at low temperatures. *Journal of nuclear materials*, *239*, pp.279-283.

[25] Hojou, K., Otsu, H., Furuno, S., Sasajima, N. and Izui, K., 1997. Isotope effect between hydrogen and deuterium ion irradiation on titanium carbide (TiC) at low temperature. *Nuclear Instruments and Methods in Physics Research Section B: Beam Interactions with Materials and Atoms*, *127*, pp.203-207.

[26] Hojou, K., Otsu, H., Furuno, S., Kushita, K.N., Sasajima, N. and Izui, K., 1999. Damage evolution in TiC crystals during hydrogen and helium dual-ion beam irradiation. *Nuclear Instruments and Methods in Physics Research Section B: Beam Interactions with Materials and Atoms*, *148*(1-4), pp.720-725.

[27] Dickerson, C., Yang, Y. and Allen, T.R., 2012. Defects and microstructural evolution of proton irradiated titanium carbide. *Journal of nuclear materials*, *424*(1-3), pp.62-68.

[28] Pellegrino, S., Thomé, L., Debelle, A., Miro, S. and Trocellier, P., 2013. Damage production in carbide single crystals irradiated with MeV heavy ions. *Nuclear Instruments and Methods in Physics Research Section B: Beam Interactions with Materials and Atoms*, *307*, pp.294-298.

[29] Gavarini, S., Millard-Pinard, N., Garnier, V., Gherrab, M., Baillet, J., Dernoncourt, L., Peaucelle, C., Jaurand, X. and Douillard, T., 2015. Elaboration and behavior under extreme irradiation conditions of nano-and micro-structured TiC. *Nuclear Instruments and Methods in Physics Research Section B: Beam Interactions with Materials and Atoms*, *356*, pp.114-128.

[30] Pellegrino, S., Trocellier, P., Thomé, L., Miro, S., Costantini, J.M. and Jouanny, E., 2019. Raman investigation of ion irradiated TiC and ZrC. *Nuclear Instruments and Methods in Physics Research Section B: Beam Interactions with Materials and Atoms*, *454*, pp.61-67.

[31] Weaver, K.D., Sterbentz, J., Meyer, M., Lowden, R., Hoffman, E. and Wei, T.Y., 2004. *Gas-cooled Fast Reactor (GFR) fuel and In-Core Fuel Management*.

[32] Fleischer, R.L., Price, P.B., Walker, R.M. and Walker, R.M., 1975. *Nuclear tracks in solids: principles and applications*. Univ of California Press.

[33] Hlatshwayo, T.T., O'Connell, J.H., Skuratov, V.A., Msimanga, M., Kuhudzai, R.J., Njoroge, E.G. and Malherbe, J.B., 2015. Effect of Xe ion (167 MeV) irradiation on polycrystalline SiC implanted with Kr and Xe at room temperature. *Journal of Physics D: Applied Physics*, *48*(46), p.465306.

Chapter two

2. Sintering methods

Sintering is a process of heating powder to coalescence into solid/porous material. This is an ancient technique that has been used to consolidate powders. It is a complex chemical phenomenon, it causes loose particles to bond together resulting in shrinking, densification and grain growth. The characteristics of the powder govern to a great degree the physical and chemical property of the final product [1]. There are different types of sintering such as pressure less sintering, microwave sintering, liquid phase sintering, spark plasma sintering (SPS) just to mention a few. Among these methods SPS is the only method that is known to produce highly densified products. Hence it was used to sinter TiN and TiC powders in this study, and it is discussed in this chapter.

2.1 Spark plasma sintering (SPS)

Spark plasma sintering (SPS) is a sintering technique that utilizes uniaxial force and a pulsed direct electrical current under low atmospheric pressure to perform high speed consolidation of powders [2]. It provides rapid densification for different types of materials [3]. This direct way of heating allows the application of very high heating and cooling rates, enhancing densification over grain growth, promoting diffusion mechanisms thus allowing the maintenance of intrinsic properties of nano-powders in their fully dense products [2].

The pulsed current leads to so-called Joule heating of the sample and die, at rates as high as about 600 °C/min [4] or even more due to the development of recent sintering machines. Unlike conventional processes where specimens are heated from the outside, spark plasma sintering produces a unique temperature distribution whereby the temperature gradient increases radially from the centre of the sample to the outside [5] as the size of the die-punch increases.

Spark Plasma Sintering systems offer many advantages over conventional sintering systems such as hot press (HP) sintering, hot isostatic pressing (HIP) or atmospheric furnaces, including ease of operation and accurate control of sintering energy as well as high sintering speed, high reproducibility, safety and reliability. While similar in some respects to hot press, the spark plasma sintering process is characterized by the application of the electric current through a power supply, leading to very rapid and efficient heating. The heating rate during the spark plasma sintering process depends on the geometry of the sintering die, its thermal and electrical properties, and on the electric power supplier. Heating rates as high as 100 °C/min can be achieved in more recent equipment. Consequently, the processing time typically takes some minutes depending on the material, dimensions of the piece, configuration, and equipment [2].

In 1990, Sumitomo Heavy Industries Ltd. (Japan) developed the first commercially operated plasma activated sintering (PAS) and spark plasma sintering (SPS) machines with punches and dies made from electrically conductive graphite [6]. One of the noticeable features of these machines was that, in addition to electrically conductive powders, high density was also achieved in insulating materials. In plasma activated sintering process, a pulsed direct current is normally applied at room temperature for a short period of time followed by a constant DC applied during the remainder of the sintering process [7]. This procedure is often referred to as a single pulse cycle process. In the spark plasma sintering process, a pulsed direct current is applied repeatedly from the beginning to the end of the sintering cycle. In this case the procedure is referred to as a multiple pulse cycle process.

Figure 2-1 shows the schematic diagram of SPS. In this figure only the chamber is represented. The basic configuration of a typical spark plasma sintering system consists of a spark plasma sintering machine with vertical single-axis pressurization and built-in water-cooled special energizing mechanism, a water-cooled vacuum chamber, atmosphere controls, vacuum exhaust unit, special sintering direct current pulse generator and a spark plasma sinter controller. The

powder materials are stacked between the die and punch on the sintering stage in the chamber and held between the electrodes. Under pressure and pulse energized, the temperature can quickly rise from room temperature to 1000~2500 °C above the ambient temperature, resulting in the production of a high quality sintered compact in only a few minutes.

When a spark discharge appears in a gap or at the contact point between the particles of a material, a local high temperature-state of several to ten thousand of degrees centigrade is generated momentarily. This causes evaporation and melting on the surface of powder particles in the spark plasma sintering process, and necks are formed around the area of contact between particles. Grain growth is typically lower during densification by spark plasma sintering due to increased heating rates and the application of the external force, which leads to faster densification than conventional sintering or hot pressing [2].

It is regarded as a rapid sintering method in which the heating power is not only distributed over the volume of the powder compact homogeneously in a macroscopic scale, but more-over the heating power is dissipated exactly at the locations in the microscopic scale, where energy is required for the sintering process, namely at the contact points of the powder particles. This fact results in a favourable sintering behaviour with less grain growth and suppressed powder decomposition. Depending on the type of the powder, additional advantageous effects at the contact points are assumed by a couple of authors [9,10].

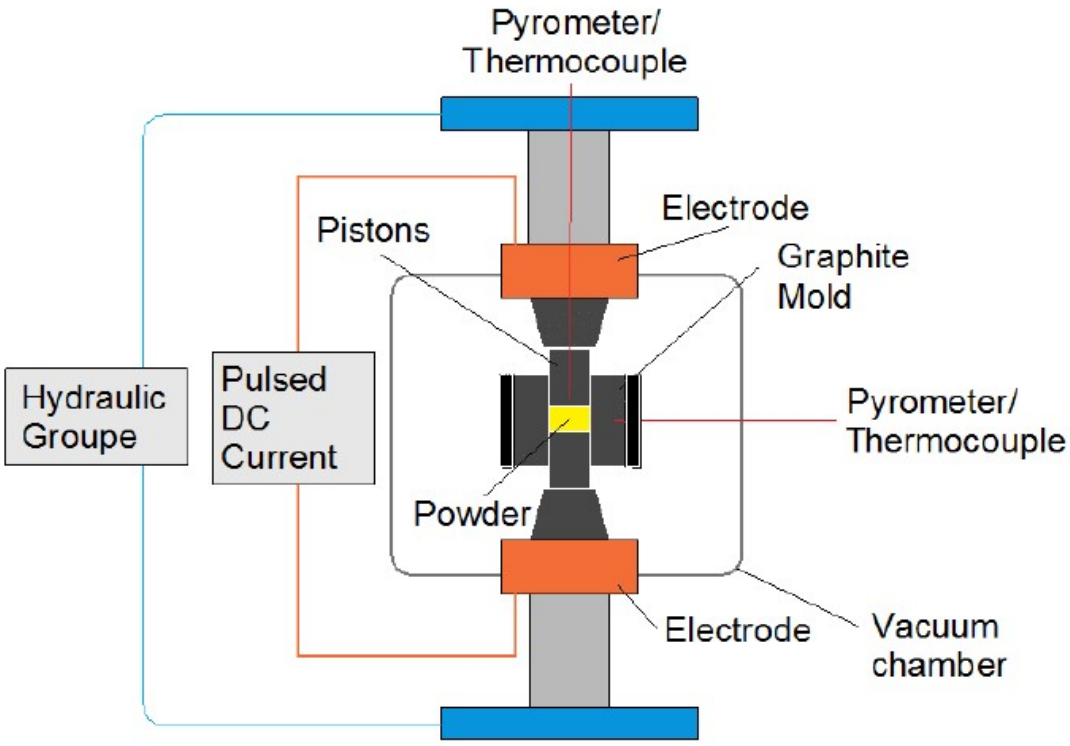

Figure 2-1: *Schematic diagram of SPS [11].*

To optimize the properties of the final product, the powder should have the following characteristics:

(i) Small particles

(ii) Equiaxed particle shape

(iii) Narrow size distribution

(iv) High purity

In this work spark plasma sintering (SPS) was employed to sinter TiN and TiC powders. Due to their high melting points (TiC and TiN), SPS was preferred over other sintering methods. Some advantages of SPS include: fast sintering, low grain growth, uniform sintering, cements are not necessary, compaction and sintering are combined in one stage, high energy efficiency,

better purification and activation of the powder particles, easy operation and ability of processing different materials. Some disadvantages of SPS include: its limitation to only simple symmetrical shapes and an expensive pulsed DC generator is required.

In this work sintering of powders was achieved by, model- H-HPD 25, manufactured by FCT Sytem, GmBH Germany. The powders were filled in a 20 mm inner diameter graphite die, with a 0,2 mm thick graphite foil thickness placed between the die and powder for easy removal and reduction in temperature inhomogeneity. The outside of the graphite die was covered with an insulating felt to reduce radiation loss and temperature gradient. Sintering was conducted in vacuum of 0,05 mbar, at a holding temperature of 1900 °C which was measured and controlled by an optical pyrometer and a pressure of 50 MPa with a 10 min holding time at sintering temperature. The heating rate for all the sintering experiments was 100 °C/min. At the end of the sintering cycle, the specimens were rapidly cooled to room temperature. Specimens of 20 mm diameter and approximately 5 mm in thickness were attained.

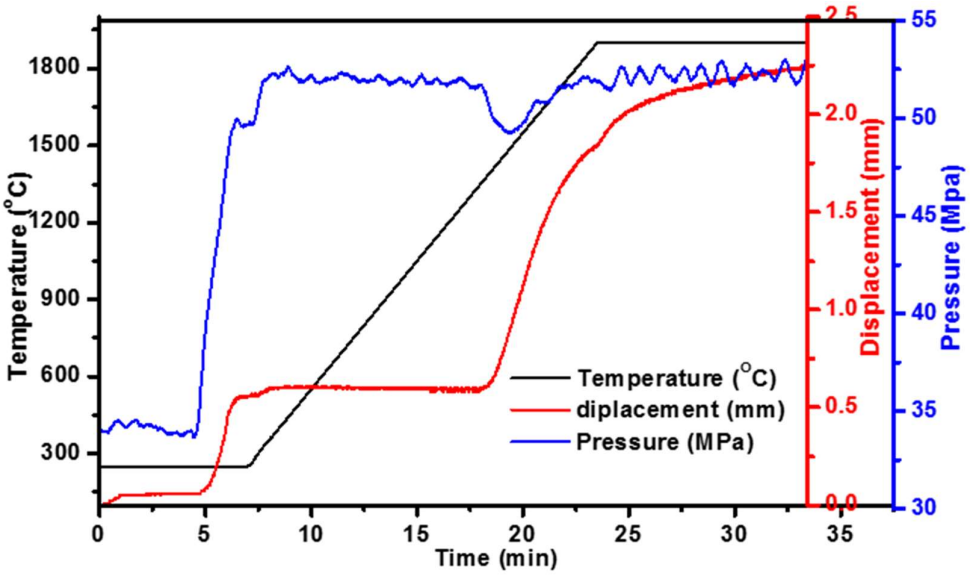

Figure 2-2: *The variation of temperature, pressure and the displacement of the lower punch, with respect to time in minutes.*

Figure 2-2 shows the variation of temperature, pressure and the displacement of the lower punch with respect to time. The densification behaviour of the powder (TiN/TiC) was derived from the lower punch relative displacement curve. The displacement curve is of the SPS process heating rate of 100 °C/min and corresponds to the positive direction movement of the lower piston as the sample undergoes densification at elevated temperature and thermal contraction during cooling. As mentioned earlier the inside pyrometer measures temperatures above 250 °C. After the first 5 minutes during sintering the chamber has reached a temperature of 250 °C, the powder starts to densify as the pressure is maintained at 50 MPa. For the next 10 minutes or so the piston was stationary due the expansion of the powder. Suddenly the displacement increases causing the axial pressure to dip and the increase again due to inertia. This is the point where the densification of the powder starts at 1500 °C. The displacement then increases and starts to decrease and comes to a stationary position as the axial pressure is maintained at a constant at 50 MPa. There is a dip on the displacement graph as the densification of the powder approaches maximum densification at 22.5 minutes into sintering at 1900 °C. After 10 minutes of holding time the apparatus automatically switches off and the cooling starts. The cooling is achieved by flowing compressed air into the chamber until room temperature is attained and the chamber can be safely opened.

2.2 References

[1] Pierson, H.O., 1996. *Handbook of refractory carbides & nitrides: properties, characteristics, processing and applications*. William Andrew, pp.100-250.

[2] Munir, Z.A., Anselmi-Tamburini, U. and Ohyanagi, M., 2006. The effect of electric field and pressure on the synthesis and consolidation of materials: A review of the spark plasma sintering method. *Journal of materials science*, *41*(3), pp.763-777.

[3] Zavaliangos, A., Zhang, J., Krammer, M. and Groza, J.R., 2004. Temperature evolution during field activated sintering. *Materials Science and Engineering: A*, *379*(1-2), pp.218-228.

[4] Räthel, J., Herrmann, M. and Beckert, W., 2009. Temperature distribution for electrically conductive and non-conductive materials during Field Assisted Sintering (FAST). *Journal of the European Ceramic Society*, *29*(8), pp.1419-1425.

[5] Suárez, G., Sakka, Y., Suzuki, T.S., Uchikoshi, T., Zhu, X. and Aglietti, E.F., 2009. Effect of starting powders on the sintering of nanostructured ZrO_2 ceramics by colloidal processing. *Science and Technology of Advanced Materials*,*10*, pp. 025004

[6] Dobedoe, R.S., West, G.D. and Lewis, M.H., 2005. Spark plasma sintering of ceramics: understanding temperature distribution enables more realistic comparison with conventional processing. *Advances in Applied Ceramics*, *104*(3), pp.110-116.

[7] Olevsky, E.A., Kandukuri, S. and Froyen, L., 2007. Consolidation enhancement in spark-plasma sintering: Impact of high heating rates. *Journal of Applied Physics*, *102*(11), p.114913.

[8] Yanagisawa, K., Sasaki, M., Nishioka, M., Ioku, K. and Yamasaki, N., 1994. Preparation of sintered compacts of anatase by hydrothermal hot-pressing. *Journal of materials science letters*, *13*(10), pp.765-766.

[9] Angerer, P., Yu, L.G., Khor, K.A., Korb, G. and Zalite, I., 2005. Spark-plasma-sintering (SPS) of nanostructured titanium carbonitride powders. *Journal of the European Ceramic Society*, *25*(11), pp.1919-1927.

[10] Borrell, A., Salvador, M.D., Rocha, V.G., Fernández, A., Avilés, M.Á. and Gotor, F.J., 2012. Bulk TiCxN1− x–15% Co cermets obtained by direct spark plasma sintering of mechanochemical synthesized powders. *Materials Research Bulletin*, *47*(12), pp.4487-4490.

[11] Yushin, D. I., 2015, Spark plasma sintering diagram plant with hybrid heating (05 January 2021), Moscow, Russia, https://www.researchgate.net/figure/*Diagram-of-Spark-Plasma-Sintering-plant-with-hybrid-heating*_fig3_283790610.

Chapter three

3. Ion implantation and irradiation

When an energetic ion impinges a material, it interacts with the atoms of the host material resulting in progressive energy loss until coming to rest inside the material. Depending on the initial energy of the ion, the ion loses energy via interacting with electrons of the host material, i.e. inelastic or electronic energy loss or interacting with the nuclei of the host material, i.e. elastic energy loss or nuclear energy loss. In ion implantation, ions have initial energies ranging from 10 to 500 of keV while in ion irradiation, ions have energies in the range of MeV to GeV. In ion implantation the elastic energy loss is dominant while in the irradiation the inelastic energy loss is dominant. In this work both irradiation and implantation were performed. Hence, it is vital to understand the two-energy loss processes in order to predict the final distribution of the ions inside material. This chapter discusses the processes that take place during ion implantation and irradiation until ions come to rest in a material of interest, ion implantation and irradiation experiments are also discussed followed by the stopping and range of ions in matter (SRIM) program simulation.

3.1 Stopping power

As the ion is traversing a material, it losses energy per distance travelled. The energy loss per unit depth, i.e. $\mathrm{dE/dx}$, (where E is energy of ion and x is the penetration depth) is known as stopping power. Since an ion traversing through a material losses energy via nuclear energy and electronic energy loss, the total stopping power (S) can be written as:

$$S = \frac{dE}{dx} = \left(\frac{dE}{dx}\right)_n + \left(\frac{dE}{dx}\right)_e \qquad [3.1]$$

where n and e represent nuclear and electronic stopping powers, respectively.

From the stopping power S, the stopping cross section can be obtained by dividing by the target density N'[1]:

$$\varepsilon = -\frac{dE}{N'dx} \qquad [3.2]$$

The independence of the nuclear stopping and electronic stopping means that the stopping power is mainly dependent on the energy of the ion (*E)*, as demonstrated in the Figure 3-1.

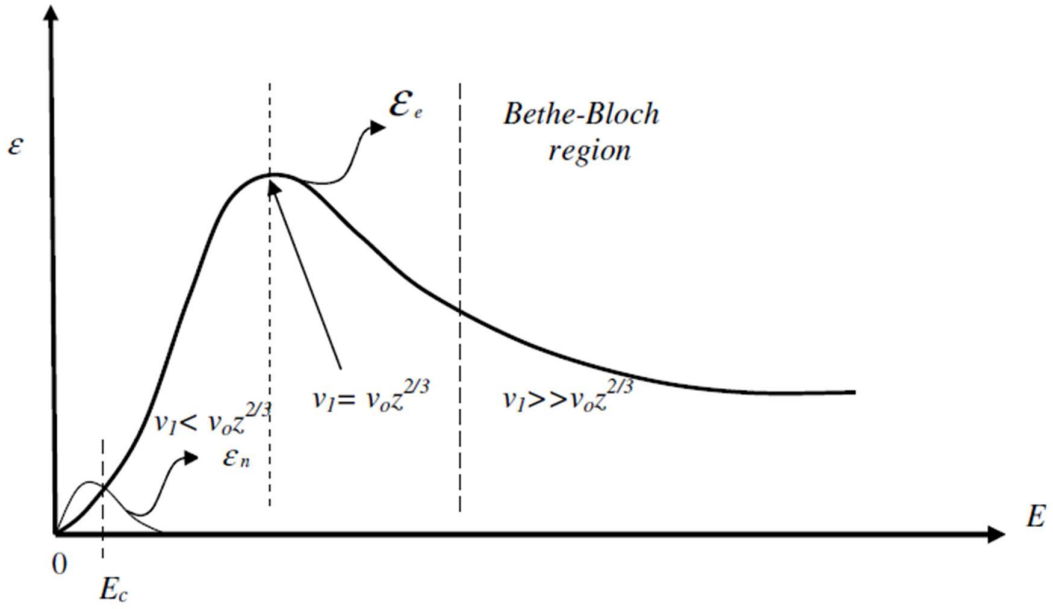

Figure 3-1: *The typical of electronic ε_e and nuclear ε_n contributions to the stopping power cross section ε as function of the energy E [1].*

From Figure 3-1, it can be noticed that at low energies the nuclear stopping power dominates while at high energies electronic stopping dominates. In fact, electronic stopping starts to dominate above the critical energy E_c, then reaches maximum and decreases at the very high energy region. This is caused by the minimum time the ion has to interact with the electrons of the atoms because of the high velocity of the impinging ions.

3.2 Nuclear stopping

Nuclear stopping power results in the transfer of energy from the implanted ion into the target atom as a whole. Therefore, the nuclear scattering can be described by the potential between implanted ion and a target atom. In a head on collision, where there is backscattering of the colliding ion from the target atom due to repulsion between colliding ion and target nuclei, the interatomic potential between the positive charges of ion and the target can be written as:

$$V = \frac{Z_1 Z_2 e^2}{4\pi\varepsilon_0 r} \qquad [3.3]$$

where Z_1 and Z_2 are the atomic numbers of the ion and the target respectively, e is the electronic charge, ε_0 is the permittivity of free space and r is the interatomic distance. This is Coulomb's potentials which assumes the screening effects are negligible. Backscattered ions are also not considered for energetic ions since nuclear stopping is only dominant at low energies.

There are other methods that consider the screening effects in the Coulomb potential, which use the basic quantum mechanics. There is also the Hartree-Fock charge distribution method used for a wide number of atomic pairs have been calculated and the results were found to agree with experimental data [2]. The analytical expression known as the universal interatomic potential was also derived [3]:

$$V = \frac{Z_1 Z_2 e^2}{4\pi\varepsilon_0 r} \emptyset\left(\frac{r}{a}\right) \qquad [3.4]$$

where $\emptyset\left(\frac{r}{a}\right)$ screening function depending on the electron density distribution in the two atoms [3].

The energy transfer mechanisms between the projectile ion and the atoms are very complicated and can be calculated using the interatomic potential between the ion and the atoms. In this scenario all the N atoms interactions are considered, and this results into N potentials. Such

calculations are known as molecular dynamics (MD) simulations and are tedious but today they are used to calculate the energy transfers between the ions and the atoms of the target material. A simpler classical approach has been adopted which limits the calculations to a binary collision approximation (BCA).

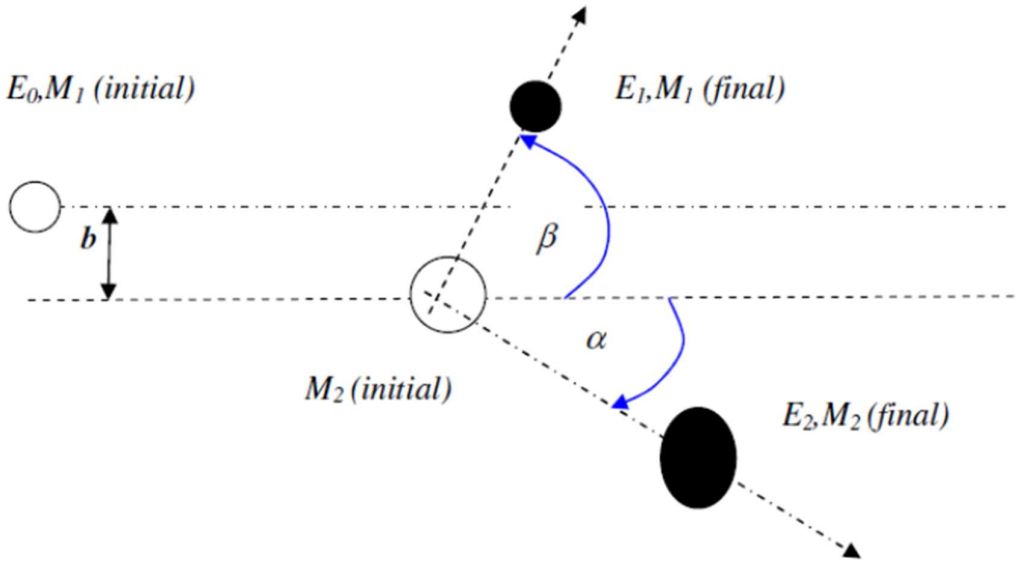

Figure 3-2: *The schematic diagram showing the ion M_1 of initial energy E_0 colliding with the target atom M_2 (initial) causing it to move with energy E_2 and its own energy reducing to E_1 [4].*

The schematic diagram in Figure 3-2 shows a collision between an energetic ion (of mass M_1 and initial energy E_0) and a target atom of mass M_2. The position of M_2 relative to the M_1 trajectory is called the impact parameter and is represented by ***b*** in Figure 3-2. The angles α and β are angles of deflection for M_1 and M_2 respectively relative to M_1 original trajectory. During this interaction, kinetic energy T is transferred from M_1 to M_2. Using the conservation of energy and momentum principle kinetic energy is found to be a function of α, E_0, M_1 and M_2 in the laboratory system [5]:

$$T = E_0 \frac{4M_1M_2}{(M_1 + M_2)^2} \cos^2(\alpha) \quad [3.5]$$

and in the centre of mass system:

$$T = E_0 \frac{4M_1M_2}{(M_1 + M_2)^2} \sin^2(\frac{\alpha_c}{2}) \quad [3.6]$$

where α_c is the recoiling angle in the centre of mass system. The projectile will transfer energy T which is a function of the collision parameter, therefore the integration is over all the impact parameters, the nuclear stopping power is as the in the equation 3.7 below.

$$\varepsilon_n = 2\pi \int_0^{b_{max}} T(E, \alpha) b db \quad [3.7]$$

Using equation 3.7, a universal nuclear cross section can be determined as shown in [2].

3.3 Electronic Stopping

Electronic stopping is the process whereby an energetic ion impinging a target loses its energy to the target electrons. There are several energy loss mechanisms involved in this process. These are: direct kinetic energy transfers to electrons due to electron-electron collisions, excitation or ionization of target atoms, excitation of the conduction electrons, and excitation, ionization or electron-capture of the ion [6]. Due to the complexity of the process, there are several models that are applied for different ion energies. As demonstrated in Figure 3-1, the ion energy regimes are compared with the Bohr velocity $v_o = e^2/\hbar$, where e and $\hbar$ are the electron charge and the reduced Planck's constant respectively. In this theory a hydrogen atom of 25 keV moves with the same velocity as its orbital electron, while helium atom moves with

the same velocity as its orbital electrons at 25 keV. Therefore, the ion's initial energy with velocity equal to orbital velocity can be written as a function of the ion's mass and atomic number as:

$$E = Z_1^{4/3} A_1 25\ keV \qquad [3.8]$$

where Z_1 and A_1 are the ion's atomic number and mass number respectively. In the low energy region the ion's velocity v_1 is less than $v_o Z^{2/3}$. In this region the ion loses energy through interaction with the electrons that are close to the Fermi level. The electron stopping for this region has been calculated by assuming a free electron gas with density ρ that changes slightly with location [7]. Therefore, the electronic cross section of an ion with Z_1 can be written as [2]:

$$\varepsilon_e = \int I(v, \rho) \left(Z_1(v)\right)^2 \rho dV \qquad [3.9]$$

where ε_e is the electronic stopping cross section, I is the stopping interaction function of the ion (particle) of unit charge with velocity v, Z_1 is the atomic mass of the particle, ρ is the electron density of the target and the integral is performed over each volume element dV of the target. If one considers the interaction with the charged particle to be a perturbation in the free electron gas and considering screening and polarization, then state of the ion can be changed through charge transfers. Then Z_1 in equation 3.9 can be replaced by the effective charge Z_1^*. The electron capture and electron loss depend entirely on the projectile velocity [2].

As it has been deduced that transferred energy (from the projectile to the target electron) is proportional to the projectile velocity, the electronic stopping power is proportional to the projectile velocity [7]:

$$\varepsilon_e = 19.2 \frac{Z_1^{7/6} Z_2 v_1}{\left(Z_1^{2/3} + Z_2^{2/3}\right) v_0} \left[\frac{eVcm^2}{10^{15} at}\right] \qquad [3.10]$$

where v_0 is the Bohr velocity: $v_0 = e^2/\hbar$

The second region is when the $v_1 \approx v_0 Z^{2/3}$. In this case the ion is partly ionized, and the electronic stopping reaches maximum.

The region where the ion velocity v_1 is far greater than $v_0 Z^{2/3}$ i.e $v_1 \gg v_0 Z^{2/3}$. In this region the ion is fully stripped of all its electrons. The energy loss is proportional to Z_1^2 as found by Bethe and Bloch. Hence this region is known as the Bethe-Bloch region, as indicated in the Figure 3-1. The electronic stopping in this region is given by the Bethe-Bloch equation [8–10]:

$$E_e = \frac{4\pi Z_1^2 Z_2 e^4}{m_e v_1^2}\left[\ln\left(\frac{2m_e v_1^2}{I}\right) + \ln\left(\frac{1}{1-\beta^2}\right) - \beta^2 - \frac{C}{Z_2}\right] \qquad [3.11]$$

where m_e is the electron mass, v_1 is the velocity of the projectile, $\beta = v/c$ where c is the speed of light, I is the average ionization potential and C/Z_2 is the shell correction. I is defined theoretically as $\ln I = \sum_n f_n \ln E_n$. Here E_n and f_n are possible energy transitions corresponding to oscillator strengths for target atoms. Hence the Thomas-fermi model has been used to estimate I. The approximation is Bloch's rule: $I = Z_2 10\text{eV}$ [10].

In this study Xe ions of 360 keV and 167 MeV were implanted into TiC and He ions of 167 MeV was used in RBS analysis. For Xe and He, $v_0 Z^{2/3} v_0 Z^{2/3}$ are 4.48×10^8 and 5.53×10^6 ms^{-1} respectively while v_1 for 360 keV Xe,167 MeV Xe and 1.6 MeV He ions are 7.27×10^5, 1.57×10^7 and 8.78×10^6 ms^{-1} respectively. From these calculated results, it is quite clear that 360 keV Xe, 167 MeV Xe, and He 1.6 MeV ions are in low energy, intermediate and Bethe-Bloch region, respectively.

3.4 Energy loss in Compounds

In this study two ceramics TiN and TiC were investigated. Therefore, understanding the energy loss in these compounds is vital. In compound materials the collisions are considered to be independent encounters taking place one at a time. The collisions are distributed among the

various elements and weighted proportionally to the elemental distribution of the compound. This is known as Bragg's rule [11]. For a compound with composition A_mB_n the stopping cross section $\varepsilon^{A_m B_n}$ is then given as:

$$\varepsilon^{A_m B_n} = m\varepsilon^A + n\varepsilon^B \qquad [3.12]$$

where the *A* and *B* are the elements in the compound and *m* and *n* are the relative molar fractions of the compound.

Deviations from the Bragg's rule have been established experimentally, this is due to the assumptions made by Bragg rule. Bragg's rule assumes that the ion interactions are independent of the environment [12]. Deviations of about 10 % - 20 % from Bragg's rule is owing to the chemical and physical of the material have been observed. Such cases involved light organic gases, as well as solid compounds with a large difference between atomic masses such as oxides and nitrides of heavy metals [3]. These deviations led to the development model with respect to correcting the chemical state of the compound. This model is called the core and bonds model (CAB) [6]. In this model for stopping of ions in compounds, it is assumed that two contributions are involved. These are effects of non-bonding closed shell "core" electrons and the bonding valence electrons. If the bond structure of the compound is known the CAB correction can be determined.

3.5 Energy Straggling

An energetic particle moving through a substrate interacts with target atoms resulting in the loss of its kinetic energy. Ions of the same energy have different interactions which results in statistical fluctuation in energy loss. Therefore, two identical ions with the same initial energy do not have the same energy after traversing a thickness Δx of the same medium. This phenomenon is known as straggling. For electronic energy loss where the energy loss process is subject to statistical fluctuations of the electronic interactions, the straggling has been derived

from the Bloch-Bethe equation [2,13]. This is equation is referred to as the Bohr straggling Ω_B^2 , is given by:

$$\Omega_B^2 = 4\pi Z_z^2 Z_2 e^4 Nx \qquad [3.13]$$

where Ω_B^2 is the variance of the average energy loss of a projectile travelling through target of thickness x. The distribution of energy for many dependent of collisions is approximately Gaussian when the energy loss is small compared to the incident energy [14]. The full width at half maximum (FWHM) of the energy loss distribution is given by $2\Omega_B\sqrt{2\ln 2}$. The Bohr theory of straggling is preferred over other theories. This theory extended to include corrections for energies where earlier assumptions may not be applicable. Some of these models include works by [7,15]. In compounds, the total energy struggling is through a similar linear additivity rule or Bragg's rule for energy loss [3,15].

3.6 Range of the implanted ions

Energetic ions that interact with matter lose energy via electronic energy loss and nuclear energy loss until they come rest inside the substrate. The path described by an impinging ion in a substrate is usually zigzag because of statistical fluctuations of the interactions during energy loss processes. Ions of the same energy may be implanted at different depths due to the statistical fluctuations. The deviation of the range due to energy fluctuations is called range straggling. The average penetration depth of ions from the target surface to where the ion comes to rest is the projected range, therefore the total range can be given by: $R_{tot} = \sum l_i$. Where l_i represents the different lengths of the paths traveled by ions inside the substrate. Figure 3-3 below shows two ions penetrating a substrate, one with high incident energy (top) and other with low incident energy (bottom). The ion with high incident energy travels in a straight line due to electronic energy loss and ultimately starts to show zigzag motion due to nuclear energy loss. The ion with low incident energy starts to show zigzag motion since the nuclear energy

loss and electronic energy loss have the same magnitude. The low energy ion travels for a short distance inside the substrate due to it low energy and many deflections as it interacts with the atoms of the substrate. The projected range R_p is defined as the average penetration depth from the substrate surface to where it comes to rest (measured parallel to the incident direction). On other hand the perpendicular range $R_{\perp}$ is measured perpendicular to the direction of the incident ion. The expression relating the range of an energetic particle with initial incident energy E_0 moving through a target material of atomic density *N,* is given as [16]:

$$R = \frac{1}{N}\int_0^{E_0} \frac{dE}{(dE/dx)} \qquad [3.14]$$

The standard practice when dealing with penetration depths of ions into target is to consider the projection of the distance traversed into the medium by an ion (the range *R* of the ion) onto the direction of incidence. This projection is called the projected range R_p of the projectile or ion.

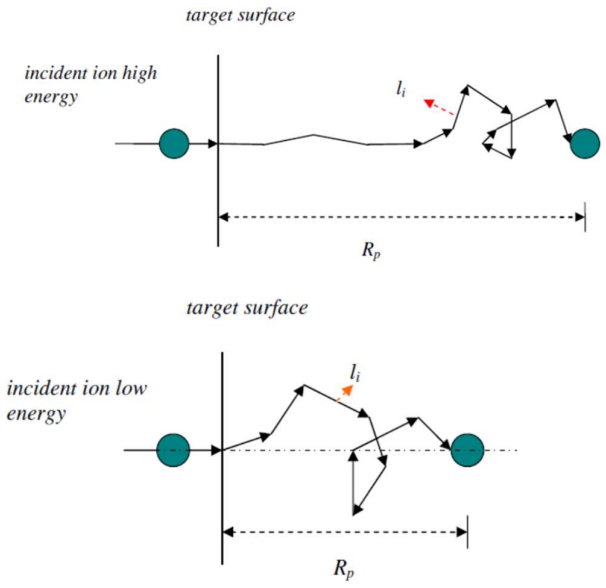

Figure 3-3: *The Range of an ion with high energy (top figure) and the range of an ion with low energy (bottom Figure) [4].*

In the situation of multiple ions impinging on a target, the mean value of the projections of the individual total ranges of ions on the initial direction of the beam path gives the R_p of the distribution of the ions in the material. The statistical fluctuations (standard deviation (ΔR_p)) on the projected range is referred to as the range straggling (see equation 3.17).

The implanted profile is usually almost similar to a Gaussian profile. The collisions between the energetic impinging ions and the atoms of the substrate are statistical in nature [17]. The concentration of incident ions as a function of depth *x* is given by [18]:

$$c(x) = C_p \exp\left[\frac{(x-R_p)^2}{2\pi\Delta R_p}\right] \qquad [3.15]$$

where ΔR_p is the standard deviation of the distribution (range straggling), R_p is the projected range and C_p is the maximum concentration of height in Gaussian ion distribution which is given by [19]:

$$C_p = \frac{\varphi}{\sqrt{2\pi N \Delta R_p}} \qquad [3.16]$$

where the ion fluence is φ(ion/cm^2), N is the atomic density of the substrate. The range straggling is defined by:

$$\Delta R_p = \sqrt{\frac{1}{\varphi}\int_{-\infty}^{\infty}(x-R_p)^2 C(x)dx} \qquad [3.17]$$

R_p and ΔR_p are the moments of Gaussian profile. The other moments are skewness and kurtosis. The skewness, γ, is the measure of the degree of asymmetry of distribution. The skewness of a profile is positive if the distribution has an asymmetric tail extending towards more positive values, and if the opposite occurs the skewness will have a negative value. The kurtosis, β, is described as the contribution ion distribution profile tail over the flatness of the

profile shape. For a perfect Gaussian profile, the skewness and the kurtosis are 0 and 3 respectively. According to Figure 3-4 (a) the Xe profile for TiN shows a skewness of 0.76 and kurtosis of 2.30. These results show that the profile was not a perfect Gaussian profile. From Figure 3-4 (b) the skewness of the Xe profile in TiC is 0.84 and kurtosis is 2.30 which also shows that the profile was not a perfect Gaussian profile. The kurtosis and skewness can be calculated from equation (3.18) and (3.19) respectively:

$$\beta = \frac{\int_{-\infty}^{\infty}(\mathrm{x\text{-}R_p})^4 \mathrm{C(x)dx}}{\varphi \Delta \mathrm{R_p^4}} \qquad [3.18]$$

$$\gamma = \frac{\int_{-\infty}^{\infty}(\mathrm{x\text{-}R_p})^3 \mathrm{C(x)dx}}{\varphi \Delta \mathrm{R_p^3}} \qquad [3.19]$$

Depth profiles of Xe implanted into TiN and TiC are shown in the Figure 3-4. The as-implanted depth profiles were fitted to an Edgeworth distribution using the Genplot program to obtain the projected range (R_p), range straggling ΔR_p, kurtosis (β) and skewness (γ). The Edgeworth distribution equation is given by:

$$N(x) = Af(x)exp\left[\frac{(x-R_p)^2}{2\Delta R_p^2}\right] \qquad [3.20]$$

$$f(x) = 1 + \frac{\gamma}{6}\left[\left(\frac{x-R_p}{R_p}\right)^3 - 3\left(\frac{x-R_p}{\Delta R_p}\right)\right] + \frac{(\beta-3)}{24}\left[\left(\frac{x-R_p}{\Delta R_p}\right)^4 - 6\left(\frac{x-R_p}{\Delta R_p}\right)^2 + 3\right] \qquad [3.21]$$

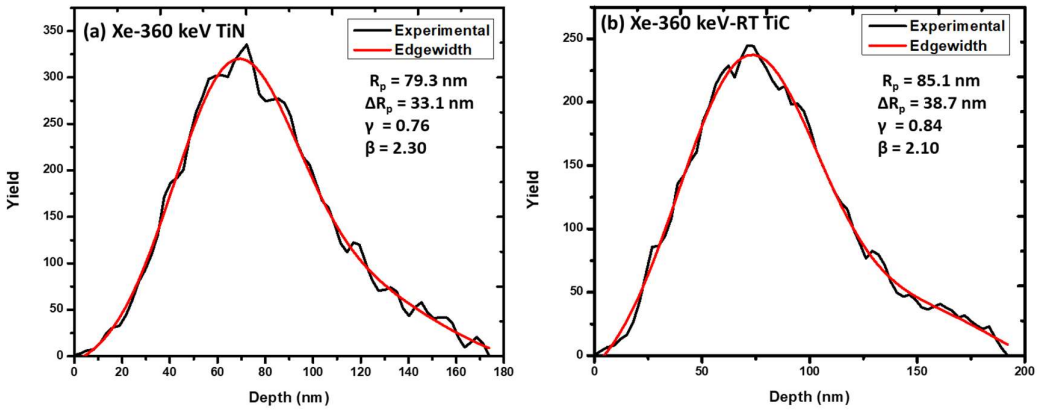

Figure 3-4: *The final distribution of Xe implanted into TiN and TiC obtained by RBS, the fitted Edgeworth distribution is included.*

From the fitted results, it is quite clear that both implanted profiles were almost Gaussian as expected for implanted species (Figure 3-4 (a) shows the skewness of 0.76 and kurtosis of 2.30. Figure 3-4 (b) shows the skewness of 0.84 and kurtosis of 2.10).

3.7 Simulation of ion implantation/ irradiation

Ion implantation/irradiation simulation was performed to gain insight in the expected results. In this work the stopping range of ions in matter (SRIM 2012) program was used for simulations [17]. This program can determine the ion range, damage range, ion and damage distributions as well as angular and energy distributions of backscattered and transmitted ions in amorphous targets. This program achieves high computing efficiency and a moderate accuracy of about 5 – 10 % error. Like any other computing program, SRIM has assumptions that must be taken into considerations. These approximations include the following:

(i) Binary collision, these are collisions which are taken to have no external influence and therefore the masses are considered as point masses, considering the size of the nucleus

(ii) Recombination of knocked off atoms with the vacancies is neglected

(iii) Electronic stopping power is taken as an average fit from a large number of experiments.

(iv) The target atom which reaches the surface can leave the surface provided it has sufficient energy and momentum to overcome the surface barrier.

(v) The interatomic potential is taken as a universal form which is an averaging fit to quantum mechanical calculations.

(vi) The system assumes that the material exists as layers, i.e. simulation of materials with composition differences in 2D or 3D is impossible.

During simulation, the impinging ions are assumed to change direction as a result of binary nuclear collisions, and they move in straight free paths between collisions. The other process involved such nuclear and electronic energy loses are independent and the ion track is terminated either when the energy drops below a pre-specified value or when the ion position is outside the target in this program. Since nuclear and electronic energy loss are independent, the ions lose energy in discrete amounts in nuclear collisions and continuously in electronic interactions. SRIM 2012 only works in the ion energy range of about 0.1 keV to several MeV, depending on the ions involved [20].

In this work, the sintered TiN and TiC samples were cut into 10×10 mm^2 using a diamond saw before polished to 0.25 μm using diamond suspension to remove scratch marks from the cutting process. The as-polished samples were then successively cleaned using acetone, deionised water and methanol.

Some of the polished samples were implanted with Xe ions of 360 keV at room temperature to a fluence of 1.1×10^{16} cm^{-2} and others were firstly irradiated with Xe ions of 167 MeV to a fluence of 3.4×10^{14} cm^{-2} followed by implantation of Xe ions of 360 keV to a fluence of 1.1×10^{16} cm^{-2}. Both implantations and irradiations were performed at room temperature Figure 3-5 shows the schematic diagrams of implantation and irradiation processes. High fluences for

both implantation and irradiations were chosen to maximize radiation damage retained. The low energy ions irradiations were performed at the FAMA (facility for modifications and analysis of materials with ion beams), located in the laboratory of Physics of the Vinća Institute at Belgrade, Serbia. FAMA is a low energy facility for basic and applied research in the field of modification and analysis of materials with ion beams and constitutes the largest scientific infrastructure in Serbia. High energy irradiations were performed using the IC-100 cyclotron at Flerov Laboratory for Nuclear Reactions (FLNR), Joint Institute for Nuclear Research (JINR) in Dubna, Russia. To control the temperature the ion current was kept at 0.5 μA and the samples were fixed with heat conductive glue to the sample holder. Ion beam homogeneity over the samples' surfaces was achieved by use of a 2-dimensional beam scanning system.

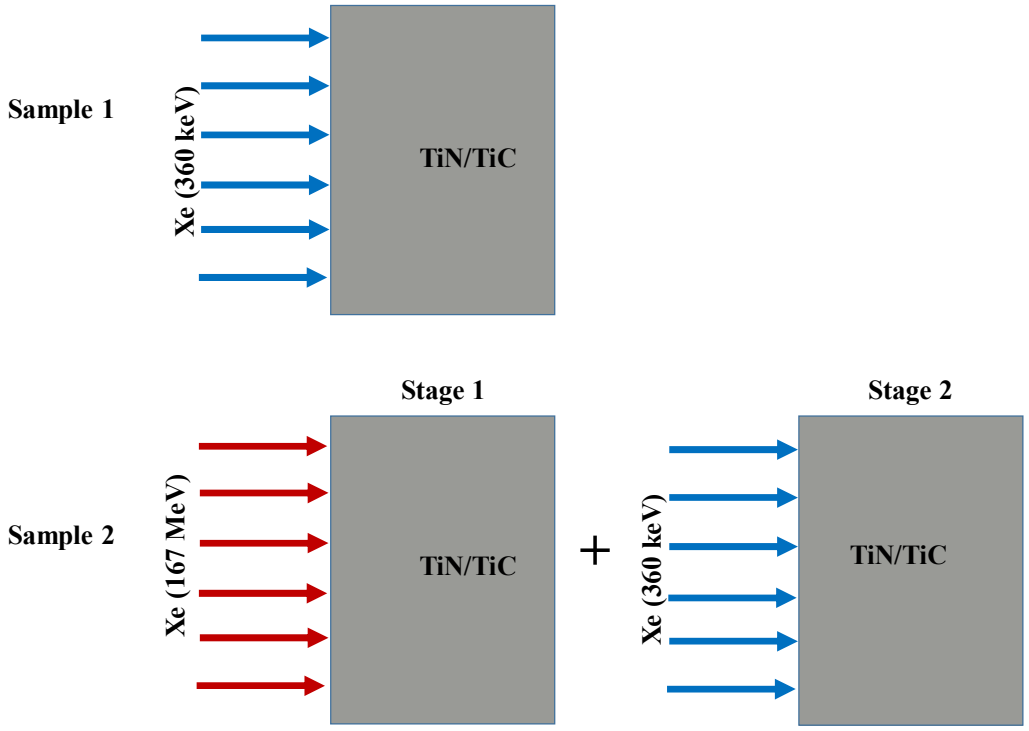

Figure. 3-5: *Schematic diagrams of implantations and irradiations of TiN and TiC samples.*

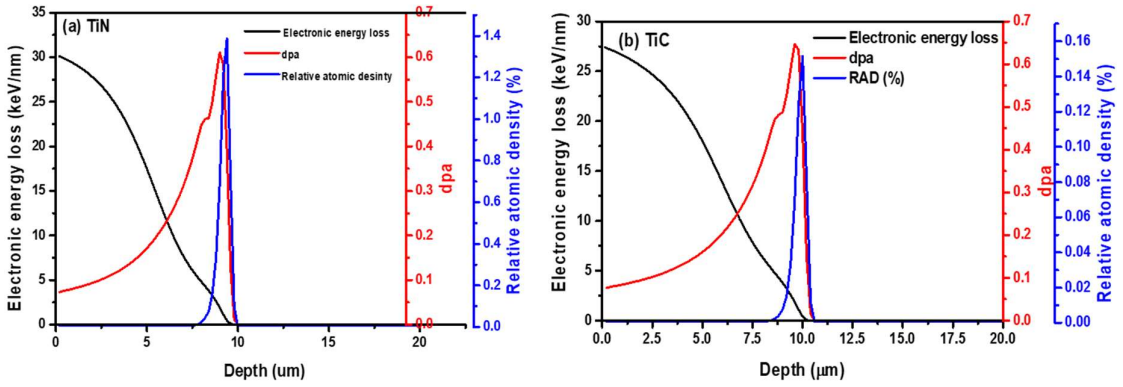

Figure 3-6: *SRIM simulated results of Xe (167 MeV) irradiated into TiN and TiC at RT.*

Figure 3-6 shows the plots of electronic stopping (S_e) and nuclear stopping (S_n) together with depth profile of Xe ions of 167 MeV irradiated into (a) TiN and TiC (b) at RT. The results show that Xe projected range is about 10 μm, which is way too deep to be detected by our RBS. Xe ions of 167 MeV lose energy mainly through electronic energy loss up to a depth of about 7 μm, while nuclear energy loss starts to dominate above 7 μm. Hence most of the energy is lost via electronic energy loss during irradiation of TiN and TiC.

Figure 3-7 shows the simulated results of 360 keV Xe ions implanted into TiN and TiC. From these results it is quite clear that energy loss is mainly via electronic energy loss in both materials. This was excepted as explained in the implantation section. Since the Xe ions of 167 MeV irradiation was performed before implantation the interaction of point defects retained by swift heavy ions irradiation and defects caused by implantation is expected. Therefore, the influence of these interactions in the migration of implanted Xe (slow moving ions) is expected in co-irradiated samples.

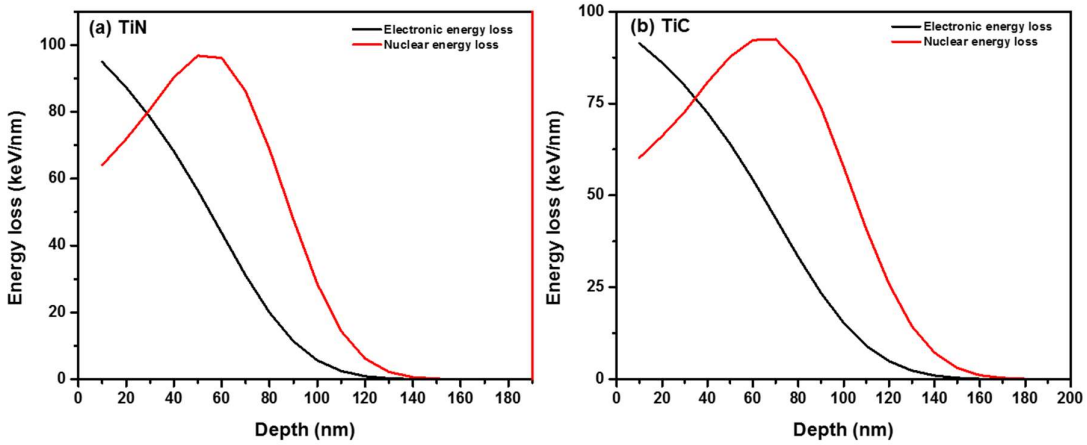

Figure 3-7: *SRIM calculations of Xe (360 keV) implanted into TiN and TiC at RT showing the electronic and nuclear energy loss.*

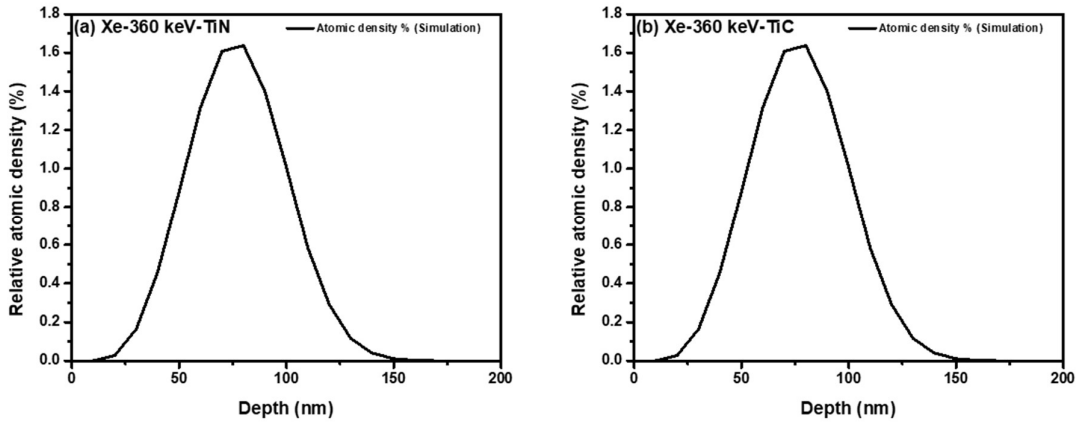

Figure 3-8: *SRIM depth profiles of Xe (360 keV) implanted into TiN and TiC.*

3.8 References

[1] Chu, W.K., Mayer J. W. and Nicolet M., 1978 Backscattring Spectroscopy, Academic press, San Franscisco, pp. 1-150.

[2] Ziegler, J.F. and Biersack, J.P., 1985. The stopping and range of ions in matter. In *Treatise on heavy-ion science* (pp. 93-129). Springer, Boston, MA.

3] Tesmer, J.R. and Nastasi, M., 1995. Handbook of modern ion beam materials analysis. *Materials Research Society, 9800 McKnight Rd, Suite 327, Pittsburgh, PA 15237, USA, 1995. 700*, pp.116-120.

[4] Hlatshwayo,T.T.,, 2010. Diffusion of silver in 6H-SiC PhD Thesis (University of Pretoria, South Africa)

[5] Thomson, J.J., 2005. *Conduction of electricity through gases*. Watchmaker Publishing, pp. 112-117.

[6] Ziegler, J.F. and Manoyan, J.M., 1988. The stopping of ions in compounds. *Nuclear Instruments and Methods in Physics Research Section B: Beam Interactions with Materials and Atoms*, *35*(3-4), pp.215-228.

[7] Lindhard J M S, and K D, 1953 Energy Loss in matter particles of Low Charge Videnskabernes Selskab Matematisk-Fysiske Meddelelser Konglige Danske. **33**

[8] Bethe, H., 1930. Theory of the transmission of corpuscular radiation through matter. *Annals of Physics Leipzig*, *5*, p.325.

[9] Bohr, N., 1913. BOHR 1913. *Philosophical Mag*, *26*, p.1.

[10] Bloch, F., 1933. Stopping power of mater for swiftly moving charged particles. *Annals of Physics*, *16*, p.287.

[11] Jenkin, J., 2004. William Henry Bragg in Adelaide: Beginning research at a colonial locality. *Isis*, *95*(1), pp.58-90.

[12] Bragg, W.H. and Kleeman, R., 1905. XXXIX. On the α particles of radium, and their loss of range in passing through various atoms and molecules. *The London, Edinburgh, and Dublin Philosophical Magazine and Journal of Science*, *10*(57), pp.318-340.

[13] Feldman, L.C., Mayer, J.W. and Grasserbauer, M., 1987. Fundamentals of surface and thin film analysis: North Holland, Amsterdam, 1986 (ISBN 0-444-00989-2). xviii+ 352 pp. Price Dfl. 125.00.

[14] Prigogine, I. and Rice, S.A., 2009. *Advances in Liquid Crystals: A Special Volume* (Vol. 244). John Wiley & Sons, pp.157.

[15] Chu, W.K., 1976. Calculation of energy straggling for protons and helium ions. *Physical Review A*, *13*(6), p.2057.

[16] Gibbons, J.F., Johnson, W.S. and Mylroie, S.W., 1975. Projected range statistics. Semiconductors and related materials.

[17] Malherbe, J.B., Selyshchev, P.A., Odutemowo, O.S., Theron, C.C., Njoroge, E.G., Langa, D.F. and Hlatshwayo, T.T., 2017. Diffusion of a mono-energetic implanted species with a Gaussian profile. *Nuclear Instruments and Methods in Physics Research Section B: Beam Interactions with Materials and Atoms*, *406*, pp.708-713.

[18] Hickey, D.P., 2007. *Ion Implantation Induced Defect Formation and Amorphization in the Group IV Semiconductors: Diamond, Silicon, and Germanium* (Doctoral dissertation, University of Florida).

[19] Agulló-López, F., Catlow, C.R.A. and Townsend, P.D., 1988. *Point defects in materials*. Academic press, pp 205.

[20] James, F. Ziegler 2012 James Ziegler - SRIM and amp; TRIM

Chapter four

4. Diffusion

Diffusion is the movement of matter from one part of a medium to another following the concentration gradient. The motion of particles of a diffusing of substance is characterized by random walk theory. In a one-dimensional system each particle has equal probability of moving in direction either side of its initial position that is, the particles have no preferred direction of motion for a given time interval. The net flow down the concentration gradient is not influenced by bias towards any direction of a particular direction. It is due to the fact there are more atoms that are randomly moved in the region of higher concentration than in the region of lower concentration. The structure of the medium influences the physical and mechanical properties of the materials often occur as a consequence of a diffusion process [1]. The transformations are brought about by material transport via atomic motion. In a crystal, the atoms are normally in constant oscillations about their fixed position at high frequencies (Debye frequency). Diffusion is a step by step migration of atoms from lattice site to another [2]. The migration is made possible by the availability of a vacancy in the lattice and the diffusing atom has sufficient energy to break bonds with its neighbouring atoms, hence overcoming the potential barrier. This migration or movement is often referred to as a 'jump'. The movement of the atoms is mainly influenced by the diffusing substance, host material and the temperature of the environment. As the substance diffuses through a medium it encounters the atoms of the medium resulting in collisions, the path is zigzag. Hence the motion is termed random walk theory.

4.1 Diffusion mechanisms

There are several ways in which diffusion takes place in solids. This chapter is dedicated to the mechanisms involved in the diffusion of Xe in ceramics (TiN and TiC). These mechanisms are vacancy, interstitial and grain boundary diffusion. In a real crystal the movement of atoms or

diffusing species is enhanced by the presence of defect structures and grain boundaries. Defects include vacancies and interstitial defects which are responsible for volume diffusion. In general grain boundary diffusion mechanism has lower activation energies than lattice diffusion. Hence it is dominant at low temperatures in solids. At high temperatures defects dominated diffusion in solids results in lattice or volume diffusion and suppresses grain boundary diffusion [1,3].

4.1.1 Vacancy mechanism

Vacancies are unoccupied sites in a lattice. They are an opportunity for diffusion of atomic species in solids. The unoccupied sites can exchange positions with neighboring atoms leaving another empty site behind. The atom moves by jumping into the vacancy. Vacancies are always present in crystalline materials they form during solidification due to vibrations and local arrangement of atoms. The probability that a site is vacant is proportional to the Boltzmann factor for thermal equilibrium [3,4]. For a crystal lattice composed of *N* atoms, the equilibrium number of vacancies η is given by the Boltzmann factor as:

$$\frac{\eta}{N-\eta} = \exp(-E_v/K_B T) \qquad [4.1]$$

where E_V is the energy that is required to move an atom from a lattice site within the crystal to one vacant site and K_B is the Boltzmann constant. When $\eta << N$ equation 3.1 becomes:

$$\eta = N\exp(-E_v/K_B T) \qquad [4.2]$$

Vacancies can also be created when a lattice atom is displaced from lattice site to an interstitial position. This type of defect is referred to as Frenkel defect [4]. If the number of Frenkel defects η, is by far smaller than *N*, the number of lattice sites and also far smaller than N', the number of interstitial sites is given by [5]:

$$\eta \cong (NN')^{\frac{1}{2}} \exp(-E_1/2K_B T) \quad [4.3]$$

where E_1 is the energy required to move an atom from a lattice site to an interstitial position.

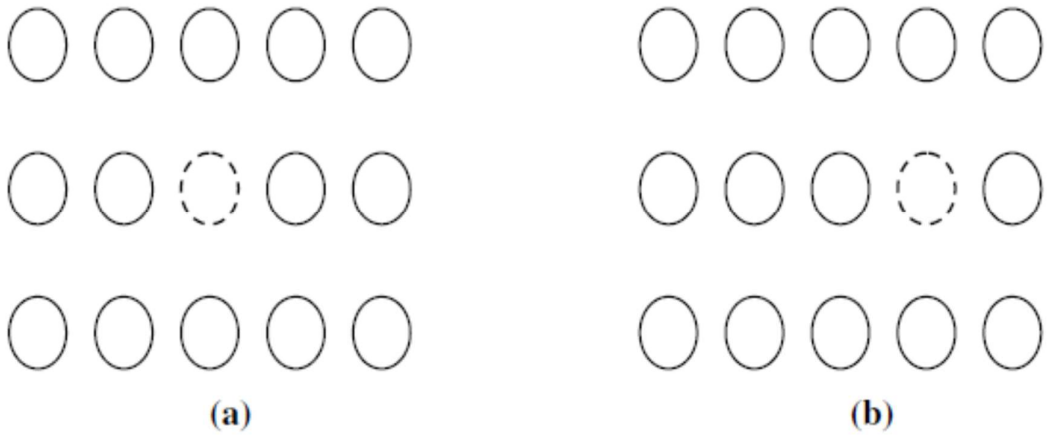

Figure 4-1: *Vacancy diffusion mechanism: the dotted circle represents a vacancy, the open circles represents atoms positions (a) before and (b) after diffusion respectively [7].*

4.1.2 Interstitial mechanism

In solids crystals, there are atoms that are located on an unoccupied sites in the crystal structure not in their regular sites, these are referred to as interstitial atoms. Interstitial atoms can be larger or smaller than the host material. There are usually more interstitial sites in solid than vacancies, the probability of interstitial diffusion taking place is higher than vacancy diffusion. Small interstitial atoms can diffuse by meandering through interstices [1,6] and it is faster than vacancy diffusion. In interstitial diffusion, the interstitial atoms jump from interstitial sites which are unoccupied as shown in Figure 4-2.

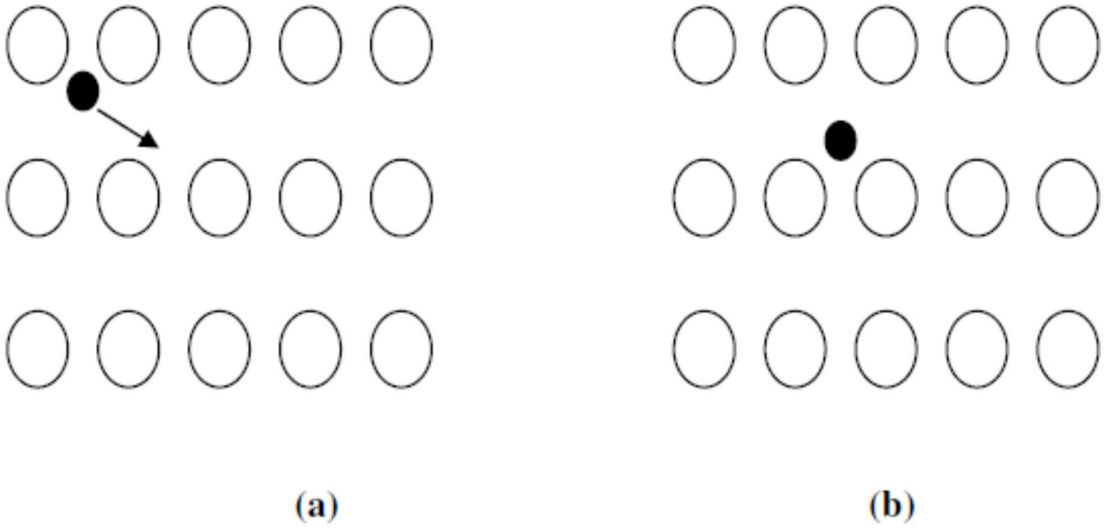

Figure 4-2: *Interstitialcy mechanism (a) before and (b) after interstitial diffusion [7].*

There are other types of interstitialcy diffusion which are commonly due to larger atoms in the host material. Larger atoms in interstitial positions may require large amounts of energy to overcome the potential barrier associated with large distortions to the lattice to an interstitial jump. In this case a jump that requires less energy to that will produce less distortions is favored. There are referred to as interstitialcy mechanism [1]. In this scenario the neighbouring atoms swap interstitial sites for lattice sites, this occurs usually when the atomic diameters of the diffusing substance is comparable with the host material [3]. There are two types of interstitial diffusion, which are collinear in which the atoms move along a straight line and non-collinear, when the displaced atoms move into an interstitial position at an angle to the direction of motion of the incident atom as shown Figure 4-3.

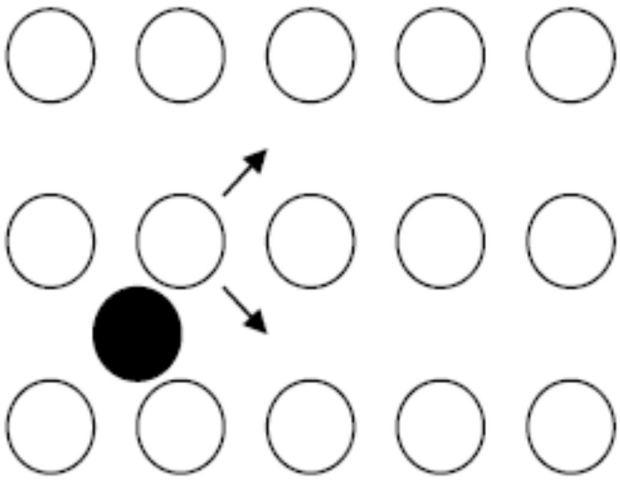

Figure 4-3: *The process of interstitial diffusion [7].*

4.1.3 Short circuit mechanism

Short circuit mechanism is form or type of diffusion that entails the diffusion of atoms/molecules along line and surface defects such grain boundaries and dislocations. Most solids are found or manufactured in polycrystalline form, and they have multiple grains generally separated from each other by boundaries along which atomic configurations are highly distorted [8]. Grain boundaries and dislocations are often referred to as high diffusivity paths, because of high diffusion within the regions. At low temperatures grain boundary diffusion and dislocation mechanism dominates lattice diffusion due to small activation energy and high level of disorder along the boundaries. Lattice diffusion however dominates at high temperatures when most of the disorder has been annealed out. Grain boundaries and dislocations make the diffusion in polycrystalline solids complex, because it is usually difficult to differentiate the two from volume diffusion. The reason being that atoms diffusing through grain boundaries and dislocations may eventually leave and continue to diffuse on the lattice around the grain boundary or dislocations [9].

4.2 Fick's first law

The diffusion flux along direction x is proportional to the concentration gradient.

$$J = -D\frac{\partial N}{\partial x} \qquad [4.4]$$

where D is the diffusion coefficient. Concentration gradient is the slope at a particular profile. The minus sign in the equation means that diffusion is down the gradient. Fick's first law describes steady state flux in a uniform concentration gradient and can be written in three dimensions as,

$$J = -D\nabla N \qquad [4.5]$$

4.2.1 Fick's second law

In most practical cases steady state conditions are not established. The concentration gradient is not uniform and varies with distance and time. Fick's second law is for the unsteady state diffusion along the x-direction and it is derived from the equation 4.5 above and the continuity equation.

Let us consider a cylinder of unit cross sectional area A- Figure 4-4. If we take two cross sections separated by distance dx, the flux through the cross-section J_1 will not be the same as the flux through the second cross-section ($J_1 \neq J_2$).

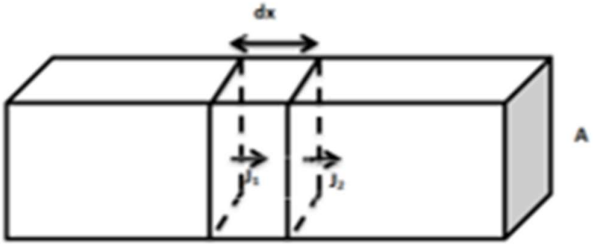

Figure 4-4: *A differential volume element in a bar of cross-sectional area A. The flux of the impurity entering and exiting the volume element is given by J_1 and J_2 respectively [10].*

Then

$$\frac{\partial J}{\partial x} = \frac{J_2 - J_1}{\partial x} \qquad [4.6]$$

As $J_1 \neq J_2$ the concentration of the diffusing particles in the small volume element of the bar should change. Since the number of impurity atoms in the volume element is the product of the of the concentration and the differential volume ($A.dx$), the continuity equation can be written as below:

$$A.dx\frac{\partial C}{\partial t} = -A(J_2 - J_1) = -A.\frac{\partial y}{\partial x} \qquad [4.7]$$

Equation 4.7 can be written as

$$\frac{\partial C}{\partial t} = -\frac{\partial J}{\partial x} \qquad [4.8]$$

Substituting equation 4.7 into equation 4.9 to yield:

$$\frac{\partial C}{\partial x}(x,t) = \frac{\partial}{\partial x}D\left(\frac{\partial C}{\partial x}\right) \qquad [4.9]$$

Assuming that the diffusion coefficient D is independent of position, the continuity equation can be written as

$$\frac{\partial C}{\partial x}(x,t) = D\left(\frac{\partial^2 C}{\partial x^2}\right) \qquad [4.10]$$

For an isotropic medium, in three dimensions Fick's second law (equation 4.6) can be written as

$$\frac{\partial C}{\partial x}(x,t) = D\nabla^2 C \qquad [4.11]$$

In a limited temperature range the temperature dependence of diffusion coefficient (D), is given by an Arrhenius equation [4.11]:

$$D = D_0 exp\frac{-E_a}{KT} \qquad [4.12]$$

where E_a is the activation energy, k is the Boltzmann constant, D_0 is the pre-exponential factor and T is the absolute temperature in Kelvins.

4.3 Evaluation of the diffusion coefficient

There are several methods of evaluating the diffusion of impurities in different materials [9,11]. In this study, the diffusion coefficients of Xe in TiN/TiC after annealing at temperatures ranging from 1100 to 1600 °C is estimated using the Arrhenius equation. In this work not all the profiles are near Gaussian, this is due to the statistical nature of the process, when energetic ions interact with substrate atoms [12]. However, there is some evidence of Fickian diffusion in some of the samples. To find the diffusion coefficient D for the Fickian diffusion in the samples we refer to the solution of Fickian diffusion solution by [12]

Considering an originally Gaussian profile with projected range R_p and range straggling ΔR_p we have equation 4.13 below:

$$C(0) = A_0 exp\left[-\frac{(\xi - R_p)^2}{2\Delta R_p^2}\right] \qquad [4.13]$$

where ξ is the depth below the surface. The solution for diffusion of the implanted profile with annealing time is given by the equations 4.10 and 4.11 below

$$N(x,t) = \frac{A_0 \Delta R_p}{\sqrt[2]{2Dt + \Delta R_p^2}} e^{\left[\frac{(x-R_p)^2}{4Dt+2\Delta R_p^2}\right]} \left[1 + erf\left(\frac{2DtR_p + \Delta R_p^2}{\sqrt[\Delta R]{2(2Dt)^2 + 4Dt\Delta R_p^2}}\right)\right.$$

$$\left. - ke^{\left[\frac{xR_p}{Dt+\frac{\Delta R_p^2}{2}}\right]} \left\{1 + erf\left(\frac{2Dt_{\ p} - x\Delta R_p^2}{\sqrt[\Delta R_p]{2(2Dt)^2 + 4DtR_p^2}}\right)\right\}\right] \qquad [4.12]$$

and

$$k = 1 - \left[\frac{2N_0}{A_0}\frac{\sqrt{2Dt + \Delta R_p^2}}{\Delta R_p} exp\left(\frac{R_p^2}{4Dt + 2\Delta R_p^2}\right) \Bigg/ \left\{1 + erf\left(\frac{R_p\sqrt{Dt}}{\sqrt[\Delta R_p]{2Dt + \Delta R_p^2}}\right)\right\}\right] \qquad [4.13]$$

There are two extreme cases for the value of *k* in the equation 4.11 above. *k* =*-1*represents the case of a perfect reflecting surface, while *k*= 1 represents in the case of a perfect sink at the surface of a substrate. In the case of this study *k*=1 is the most appropriate since Xe was implanted into the samples, and it sublimes at the surface.

To calculate the diffusion coefficients at different annealing temperatures, a software package (i.e. MATLAB program) was written in-house to fit our data and extract diffusion coefficients. As mentioned earlier the some of the profiles were not Gaussian and were asymmetric and truncated. Those profiles could not be fitted to produce any diffusion coefficients.

4.4 References

[1] Shewmon, P. ed., 2016. *Diffusion in solids*. Springer, pp.106.

[2] Callister, W.D., 2000. *Fundamentals of materials science and engineering* (Vol. 471660817). London: Wiley, pp.156-158.

[3] Murty, K.L. and Charit, I., 2013. *An introduction to nuclear materials: fundamentals and applications*. John Wiley & Sons, pp.254.

[4] Kittel, C., McEuen, P. and McEuen, P., 1976. Introduction to Solid State Physics, Wiley. *New York*.

[5] Kittel, C., McEuen, P. and McEuen, P., 1996. *Introduction to solid state physics* (Vol. 8, pp. 105-130). New York: Wiley.

[6] Gupta, D. ed., 2010. *Diffusion processes in advanced technological materials*. Springer Science and Business Media, pp.356-361

[7] Hlatshwayo,T.T.,, 2010. Diffusion of silver in 6H-SiC PhD Thesis (University of Pretoria, South Africa)

[8] Was, G.S., 2016. *Fundamentals of radiation materials science: metals and alloys*. springer.

[9] Springer, T. and Lechner, R.E., 2005. *Diffusion in condensed matter* (Vol. 1, pp. 93-164). New York: Springer.

[10] Campbell, S.A., 2001. *The science and engineering of microelectronic fabrication*. Oxford university press.

[11] Crank, J., 1979. *The mathematics of diffusion*. Oxford university press.

[12] Malherbe, J.B., Selyshchev, P.A., Odutemowo, O.S., Theron, C.C., Njoroge, E.G., Langa, D.F. and Hlatshwayo, T.T., 2017. Diffusion of a mono-energetic implanted

species with a Gaussian profile. *Nuclear Instruments and Methods in Physics Research Section B: Beam Interactions with Materials and Atoms*, *406*, pp.708-713.

Chapter five

5. Analytical techniques

This chapter discusses the main analysis techniques used to investigate the effect of swift heavy ion irradiation in the migration of Xe implanted into sintered TiN and TiC. The main techniques used in this thesis are Rutherford backscattering spectrometry (RBS), Raman spectroscopy (RS), X-ray diffraction (XRD), X-ray photoelectron spectroscopy (XPS) and scanning Electron Microscopy (SEM). The annealing system is also discussed in this chapter.

5.1 X-ray diffraction (XRD)

XRD is a non-destructive technique that is used in many fields like in geology, material science to mention a few, for structural analysis of materials. The stress, strain, crystallite size and phase of crystallites can be determined using XRD. The basic principle of XRD is the Bragg's law which states that the X-rays reflecting from the planes of a crystal interfere constructively, when the path difference is the integer multiple of the wavelength, which can be mathematical be represented as equation 5.1 below [1]

$$n\lambda = 2d_{hkl}\sin\theta \qquad [5.1]$$

where *n* is an integer, λ is the wavelength of the radiation, d_{hkl} is the spacing between the atomic planes and θ is the diffraction angle. The interplanar spacing is calculated by the following relation [1]:

$$d_{hkl} = \frac{1}{\sqrt{\frac{h^2}{a^2} + \frac{k^2}{b^2} + \frac{l^2}{c^2}}} \qquad [5.2]$$

where a, b, and c are lattice parameters and for cubic symmetry a = b = c [1]

$$d_{hkl} = \frac{a}{\sqrt{h^2 + k^2 + l^2}} \qquad [5.3]$$

The components of the diffractometer include a monochromatic X-ray source, sample stage (goniometer), detection system, closure, and safety features. One of the common configurations is the *θ - 2θ* upright. This configuration of the diffractometer has a movable detector and an X-ray source, rotating on the circumference of a circle centred on the surface of a flat specimen. The intensity of the diffracted beam is measured directly by the solid-state detection system. The diffracted beam of X-rays generates electron-hole pairs in the detector and the charge generated is collected and converted to voltage pulses by the electronic system. The number of pulses entering the detector per unit of time is proportional to the intensity of the signals [2].

Figure 5-1 shows the schematic side view of the θ - 2θ geometry of XRD. The source of the X-rays and the detector move at a constant angle θ relative to the sample. Hence the angle between the source and detector is essentially 2θ. This is the conventional θ - 2θ geometry known as the Bragg- Brentano reflection geometry. The pattern obtained is then compared with standard International Centre for Diffraction Data (ICDD) file.

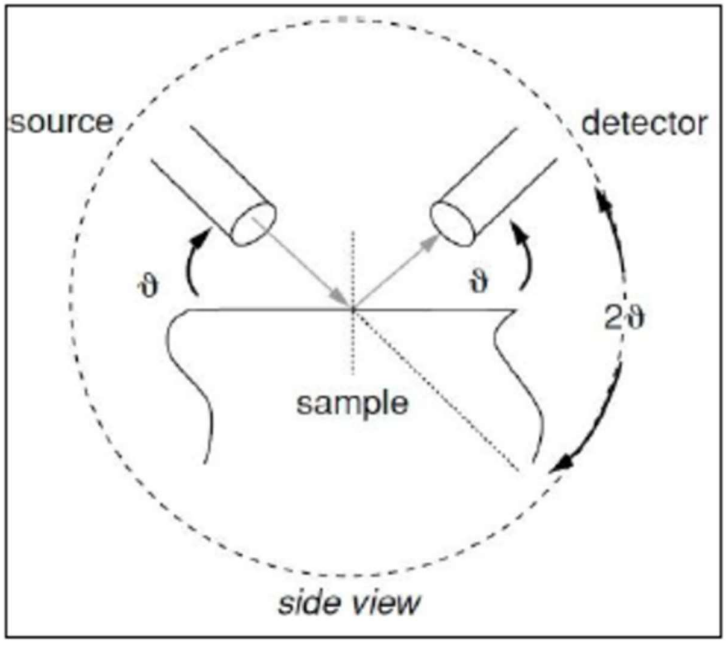

Figure 5-1: *The schematic side view of the θ - 2θ geometry of XRD analysis taken from [2].*

The crystal size can be obtained from the XRD patterns using the Sherrer equation given by [1]:

$$D = \frac{0.9\lambda}{\beta \cos \theta} \qquad [5.4]$$

where D is the crystallite size, θ is the Bragg angle and β is the full width at half maximum (in radians).

In this study the XRD analysis of the samples were performed in the University of Pretoria, South Africa using a PANalytical X'Pert Pro powder diffractometer in *θ–2θ* configuration with an X'Celerator detector and variable divergence- and fixed receiving slits with Fe filtered Co-Kα radiation (λ=1.789Å).

5.2 X-ray photoelectron spectroscopy (XPS)

When monochromatic X-ray is impinging a substrate, electron in the substrate are excited and when the energy is sufficient, they are ejected from the surface. The emitted electrons are called photoelectrons and when their energies are detected and analysed information about their original bonds may be acquired [3]. X-ray photoelectron spectroscopy (XPS) is a technique that is based on the analysis of the kinetic energies of the photoelectrons. Kinetic energies of photoelectrons carry information about the original bonding energies of the electrons thus giving chemical and elemental information about the substrate. These photoelectrons which are free of elastic collisions originate from as deep as 3-10 nm, hence XPS is a surface sensitive technique. It must be noted the X-rays penetrate deeper into the substrate and produce photoionization [3]. Photoionization is the ejection of one or more electrons from an atom by irradiation of the substrate with X-ray photon of known energy hν (where *h* is Planck's constant and *v* is the frequency of the radiation in Hertz (*Hz*) [4]. There are two common X-ray sources that are used in XPS. They are AlK_α radiation with *hv=1486.6* eV and MgK_α radiation with *hv= 1253.6 eV.* [4]. Since the X-ray energy is known and kinetic energy of photoelectrons is

measured electron binding energy (BE) of each of the emitted electrons can determined from [4]:

$$E_B = E_P - E_K - \emptyset \quad [5.5]$$

where E_B, E_P, and E_k are the binding energy of the electron, energy of the incident X-ray photon and kinetic energy of the electron respectively and $\emptyset$ is the work function of the spectrometer not the sample. This work function can be compensated for electronically, therefore, E_B can be calculated as [4]:

$$E_B = E_P - E_K \quad [5.6]$$

The binding energy is unique for a specific atom and specific orbitals. Therefore, it provides the elemental and chemical state of materials.

The basic requirements for a XPS set up are a X-ray source, an electron analyser and a high vacuum environment, that makes it possible to analyse emitted electrons with limited collisions with gas particles. The most used analyser is a concentric two hemispherical analyser (CHA). It uses an electric field generated between two hemispherical surfaces to disperse the electrons according to their kinetic energy [4]. An XPS spectrum is nothing else but the number of detected electrons as function of their binding energies. The specific binding energies give rise to characteristics peaks at specific energies indicating the presence of a specific element on the surface of the sample. The intensity of the peaks is an indication of the concentration of the element.

In this study X-ray photoelectron spectroscopy (XPS) surface analysis of the sintered TiN/TiC was done at Joint institute for nuclear research (JINR),Dubna-Russia using the Thermo SCIENTIFIC K- Alpha X-ray photoelectron spectrometer with monochromatic Al-Kα radiation. The energy scale was calibrated using the binding energy of 1Cs at 284 eV.

5.3 Raman Spectroscopy (RS)

Raman spectroscopy is basically a vibrational spectroscopy. When a monochromatic light of frequency *v* is incident on a molecule it induces electronic polarisation in the molecule. The polarizability of the molecule depends on the molecular structure and the nature of the bonds.

The electric field of the incident electromagnetic field wave may be written as 5.7 [5]:

$$E = E_0 \cos(2\pi_0 t) \quad [5.7]$$

where v_0 is the frequency of the incident electromagnetic wave is, E_0 is the amplitude of the wave ant *t* is the time. The induced dipole moment *P* is given by $P = \alpha E$, where α is the polarizability. Therefore, the time dependent induced dipole moment is then given by [5]:

$$P = \alpha E_0 \cos(2\pi v_0 t) \quad [5.8]$$

Perturbation of electron clouds of molecular structures depends on the relative location of the constituent atoms. In molecular bonds, the atoms are confined to specific vibrational modes where the vibrational energy is quantized. The displacement of the atoms about their equilibrium position is due to the vibration mode is given by [5]:

$$dQ = Q_0 \cos(2\pi v_0 t) \quad [5.9]$$

where Q_0 is the amplitude of the vibration and v_0 is the frequency of vibration. For small displacements, the polarizability may be approximated by a Taylor series expansion as [5].

$$\alpha = \alpha_0 + \frac{\partial \alpha}{\partial Q} Q_0 \quad [5.10]$$

where α_0 is the polarizability of a molecule mode at equilibrium position. Combining the equations 4.7 and 4.8 yields [5]:

$$P = \alpha_0 E_0 \cos(2\pi v_0 t) + \frac{\partial \alpha}{\partial Q} Q_0 E_0 \cos(2\pi v_0 t) \cos(2\pi v_i t) \quad [5.11]$$

Using a trigonometric identity in equation 4.11 results in [5]:

$$P = \alpha_0 E_0 \cos(2\pi v_0 t) + \left(\frac{\partial \alpha}{\partial Q} \frac{Q_0 E_0}{2}\right) \{\cos[2\pi(v_0 - v_i)t] + \cos[2\pi(v_0 + v_i)t]\} \quad [5.12]$$

Equation 4.12 shows that the induced dipole moments are created in three frequencies v_0, $(v_0 - v_i)$ and $(v_0 + v_i)$. Scattered radiation also results at the same frequencies. The first frequency corresponds to the incident frequency thus the scattering is elastic. The other two frequencies are shifted to lower and higher and are inelastic in nature. The scattered light in these two inelastic modes are the Raman modes named after C.V. Raman [5]. The shift to lower wavelengths is referred to as the Stokes scattering modes and the shift shorter wavelengths is referred to as anti-Stokes. Raman scattering is much weaker than Rayleigh scattering by a factor of 10^{-3} to 10^{-5} [5]. To obtain a good Raman spectra Rayleigh scattering must be suppressed by use of optics. Normally a Raman spectroscopy instrument consists of an excitation source (laser), sample illumination system and light collection optics, wavelength selector (filter or spectrophotometer) and detector (photodiode array of Charge Coupled Device (CCD)) [5]. The sample is usually illuminated with a laser beam in the ultraviolet (UV), visible (Vis) or near infrared (NIR) range. The scattered light is collected by a lens and is sent to spectrophotometer to obtain a Raman spectrum of the sample. Different materials or samples have different Raman spectra, since materials or samples have their unique molecular structures and bonding systems. Therefore, Raman can be used to identify materials and to study the crystal structure of materials. Raman is basically a non-destructive technique, except when high laser power is used, and the samples may get damaged.

In this study the TiN Raman spectra were recorded at the University of Pretoria, South Africa with a T64000 series II triple spectrometer system from HORIBA scientific, Jobin Yvon Technology, using the 514.3 nm laser line of a coherent Innova® 70C series Ar^+ laser (spot size ~ 2 mm) at power of 0.17 mW with a resolution of 2 cm^{-1}.While the TiC samples were characterized performed at the University of Pretoria using a WiTec alpha 300RAS + confocal Raman system (WiTecGmbh) using the 532 nm excitation laser at a power of 10 mW and a 100 ×/0.9 numerical aperture objective with a spot size of about 370 nm.

5.4 Scanning Electron Microscopy (SEM)

Morphological evolutions of the samples were monitored by scanning electron microscopy (SEM). SEM uses electrons to capture the specimen surface morphology by scanning the sample with a beam of electrons in the in the x-and y- directions. Since it was first developed in the 1930s, SEM has been used in different studies such as a material development, metallic materials, ceramics semiconductor, medical science and biology.

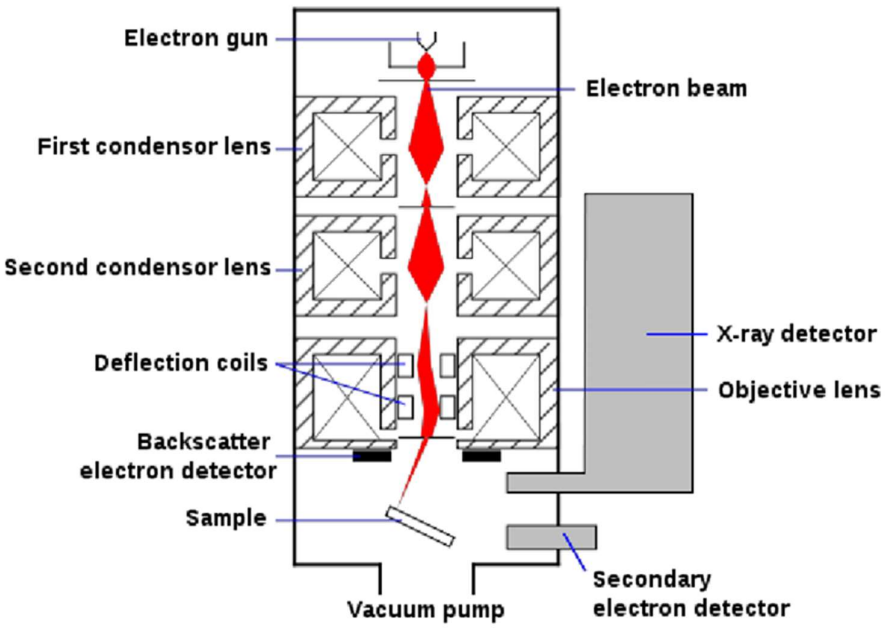

Figure 5-2: *The schematic diagram of SEM showing the main components [6].*

Figure 5-2 above shows the schematic diagram of SEM showing the main components. These components include the electron gun, condenser lenses, deflection coils, sample holder and the secondary electron detector. The inside of the SEM apparatus is kept under low pressure to avoid any contamination or any interference from the outside environment. The electrons are produced by the electron gun. The function of the electron gun is to provide a stable electron beam of adjustable energy. There are three types of electron guns. These are the tanthanum hexaboride (LaB_2), tungsten hair pin and field emission [7]. In this study the field emission gun (FEG) was used. The field emission cathode is usually a wire shaped into a sharp tip (100 nm or less in radius) supported by a tungsten hairpin. When the electric field at the tip reaches a magnitude of about 10 V/nm, electrons are emitted.

The electron gun generates free electrons with the help of the condenser lenses the electrons are accelerated to energies in the range of 1-40 keV. In this study of 2.0 keV was used in all the measurements. The electromagnetic lenses create a small focused electron probe on the sample. The probe is scanned across the sample, and the signal produced is detected and amplified before being displayed on the monitor. The detected signal is mainly made of secondary electrons.

There are mainly two interactions taking place during electron-matter interactions. Figure 5-3 shows the particles that are produced when the electron interacts with the sample. These processes can overlap for some of the X-rays. For instance, X-rays also originate from the surface regions. A backscattered electron (e^-) is the result of an elastic collision between an incoming electron and the nucleus of the target atom. The elements with higher atomic number produce more backscattered electrons. These electrons usually have higher energies compared to the energies of the secondary electrons. The detected signal of the former electrons is used for contrast between areas with different chemical compositions. The backscattered electrons

can also be used to form an electron backscatter diffraction (EBSD) image which can be used to determine the crystallographic structure of the sample [6].

Secondary electrons are the result of the inelastic collisions between the incident electrons and the target electrons of the atoms. These electrons have energy less than 50 eV [7]. Their signal is used to study the topography of the sample. These electrons are generated along the incident electrons' trajectory but only those generated a few nano-meters underneath the sample surface are detected, the others are absorbed in the sample because of their very low energy.

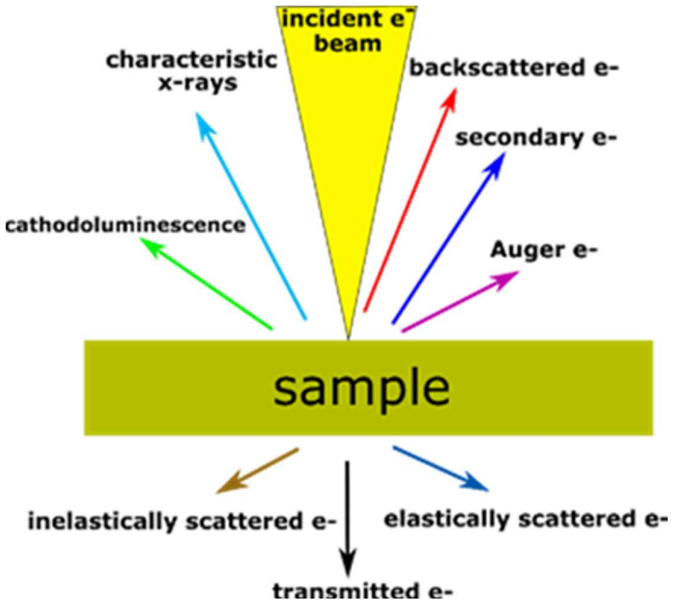

Figure 5-3: *A schematic diagram showing the types of rays that are emitted when an energetic electron (e-) is incident on the sample [8].*

Auger electrons are produced due outer shell electrons filling inner shell holes created by excited primary electrons. The excess energy available may be carried away through the release of low energy electrons (Auger electrons) or the production of X-rays. The signals that result from these Auger electrons can be used for chemical characterization of the samples, i.e. for identifying the type and concentration of the elements in the sample. The latter technique is called energy dispersive X-ray spectroscopy (EDS).

The Zeiss Ultra 55 field emission SEM at the University of Pretoria was used in this study. The microscope is equipped with secondary electrons, backscattered electrons, and in-lens Secondary Electrons detectors. In this study the in-lens SE detectors were used to study the morphology of the sample before and after annealing.

5.5 Rutherford Backscattering Spectrometry (RBS)

RBS is a technique that is based on the detection of the backscattered ions from a material of interest. For instance, in this work the material of interest is sintered TiN and TiC. which have been implanted with Xe ions and TiN and TiC irradiated with Xe SHIs then implanted with Xe ions. When a monoenergetic beam of ions impinge on a target material a small fraction of the ions are scattered back from the target material. When the backscattered particles are detected and analysed, information about the target material can be obtained. In this study, the energetic ions were helium (He^{+}) produced by a RF-source (Figure 5-4) and accelerated to high energies by application of potential difference. One of the main components of this set up is the Van der Graff accelerator [9]. The Van de Graaff accelerator uses a moving insulated belt that carries charge at high voltage produced-Figure 5-5. The charge is sprayed at the base plate and removed at the terminal as the belts rotates.

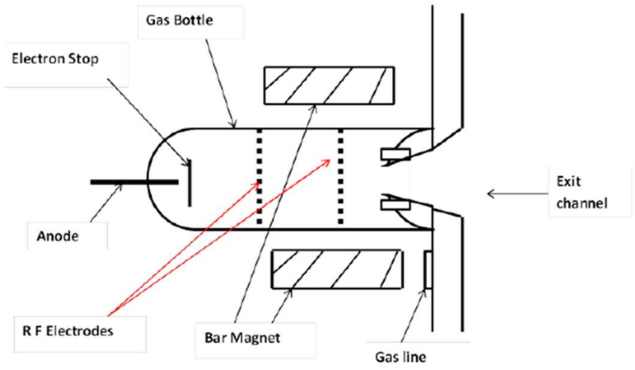

Figure 5-4: *Schematic of the rf ion source [10].*

The work reported in this thesis was carried out using the Van de Graaff accelerator at the University of Pretoria. The maximum energy that can be achieved with this machine is 2.0 MeV, but an energy of 1.6 MeV was used in this investigation.

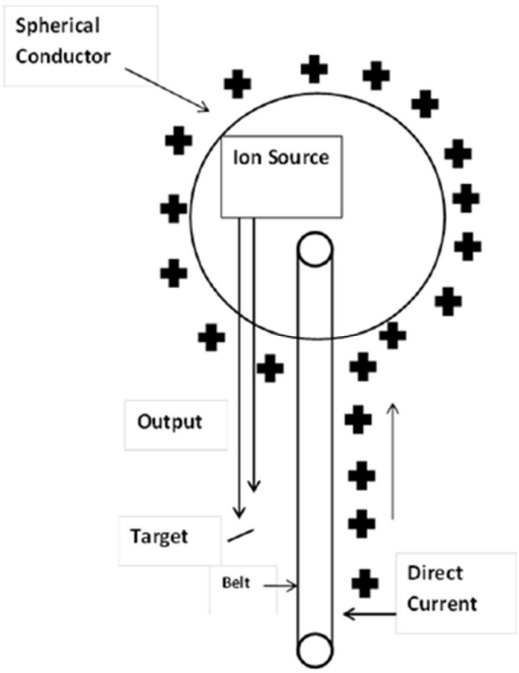

Figure 5-5: *Schematic diagram of the Van de Graaff [10].*

The dipole magnet in front of the Van de Graaff accelerator deflects the beam into either beam line 1 or beam line 2. Hence, its acts as an energy and mass separator. Beam line 1 has a chamber that is designed to operate below room temperature while beam line 2 functions at room temperature. In this study line 2 was used. A combination of vertical and horizontal slits focuses and guides the beam into the chamber. The slits also help in producing a monochromatic beam consisting of one species, that is helium ions in this case. The collimator inside the chamber (Figure 5-6), shapes the beam into a specific size before interacting with the sample. Thus, the size of the beam is determined by the collimator's size. The sample is secured on a (see Figure 5-6) holder connected on a three-axis goniometer system which has a precision of 0.02° in each of the angle settings. The secondary electrons that falsify the

measurements, suppressed by the negative voltage of 200 V connected to a ring-shaped electrode in the front of the target.

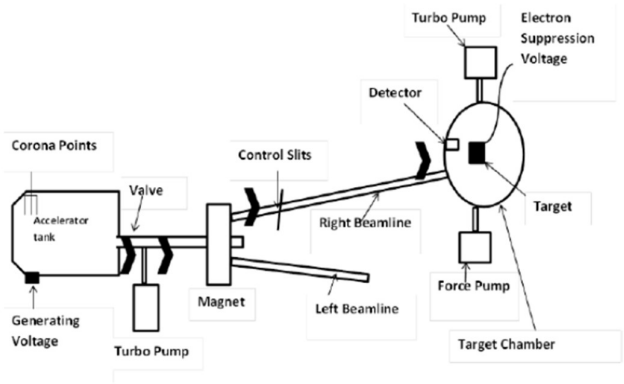

Figure 5-6: *The schematic diagram of the accelerator at the University of Pretoria [10].*

During the analysis, the beam is kept below 15 nA to avoid heating up of the sample. This is also done to avoid a pile up effect during the process of detecting backscattered particles. Pile –up occurs when the response of the detector system is not fast enough to separate individual events on the detector system is due high rate of encounter events. This results in a situation whereby two events may end up being recorded as one event, which results in wrong measurements. The hydrocarbon deposition on the sample during analysis by keeping low pressure in the chamber at 10^{-4} Pa or below during the running of the experimentation. This carbon deposition is due to the collision of the beam with residual gases and the subsequent decomposition of the gases. This occurs along the beam line but the carbon that is deposited on sample's surface is that produced near the surface is minimized by flooding the chamber with nitrogen gas during the opening of the chamber. This also helps in increasing the initial pumping rate.

The backscattered ions are detected a Si surface barrier detector operating with reverse bias of 40 V. The output charge signal of the detector is fed into a pre-amplifier where it is integrated

into voltage signal that is proportional to the backscattered energy. This voltage is then amplified and converted (by an analogue to digital converter (ADC) to digital signals inside the multi-channel analyser (MCA) and stored in the computer connected to MCA. The output of MCA consists of counts vs the channel spectrum. The yield is the number of backscattered particles at 165 ° while the channel number is proportional to the backscattered energy. Using the computer, the counts of the backscattered ions as a function of channel number are monitored electronically and saved in the computer.

5.5.1 Kinematic Factor

When an energetic particle interacts with a target as shown in Figure 5-8, some of the energetic particles are backscattered at an angle θ (which was 165° in this study) with respect to the incoming beam. During this interaction between incoming beam and the target, some target atoms also recoil at angle ∅ with respect to the incident beam. If only the elastic collisions are considered, the energy of the backscattered particles (E_1) can be calculated using the conservation of energy and momentum [10]:

$$E_1 = \left[\frac{M_1 \cos\theta \pm (M_2^2 - M_1^2 \sin^2\theta)^{1/2}}{M_1 + M_2}\right]^2 = KE_0 \qquad [5.13]$$

where E_0 and E_1 are the energies of the incident and backscattered particles respectively, M_1 and M_2 are the masses of the analysing particle and the target atom, K is the kinematic factor (the ratio of the backscattered particles energy to incident energy before scattering) and θ is the backscattering angle. Therefore, one can calculate E_1 if the kinematic factor K is known. K can be calculated using M_1 and M_2 and the scattering angle θ. At the fixed scattering angle kinematic factor K depends only on the mass ratio i.e. M_1/M_2. The plus sign in the equation above is only valid for when $M_1 < M_2$, while for $M_1 > M_2$ there two solutions resulting in two values of K for backscattered particles at an angle θ corresponding to different recoil angles $\emptyset$ [10].

The RBS technique can be used to identify the sample compositions because the particles with the same incident energy and incident angle backscattered at the different masses yield different energies according to equation 5.13. The difference in the scattering energy for different masses influence the depth resolution, which is limited by several factors. These are: the energy resolution of the detector, the spread in energy of the particle, the solid angle of the detector, the beam size and the divergence of the accelerator beam. Good mass resolution is usually obtained by using a projectile of higher mass but not larger than the target mass atom and measuring at an angle approximately at 180 °.

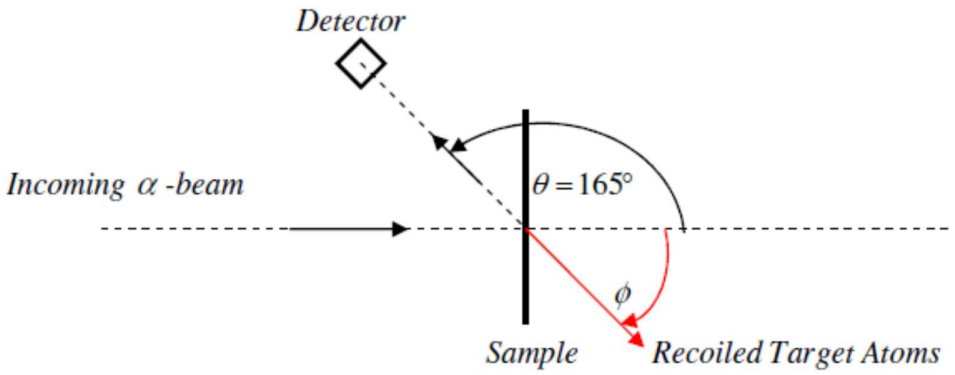

Figure 5-7: *A schematic diagram showing the RBS experimental setup at the University of Pretoria [12].*

5.5.2 Depth Profiling

The backscattered α-particles from different depth have different energies. Figure 5-8 shows a schematic diagram depicting the backscattering events at the surface and depth *x*. The alpha particle that backscatters at the surface possesses energy of KE_o while the one that backscatters at depth *x* has an initial energy E lower than E_0 because it loses energy before backscattering at depth *x*. From Figure 5-8 the length of the inward path where the ion loses energy is $x/cos\theta_1$. The ion has energy KE just after being backscattered at depth *x*. The ion that is backscattered

at depth *x* continues to lose energy on its way out; referring to the Figure 5-8 again, it is evident that the outward path is $x/\cos\theta_2$.

To calculate the energy of the alpha particle that backscatters at depth *x* one needs to consider account the fact that it loses energy both on its way in and out. Assuming that the energy loss (*dE/dx)* is constant along the inward and outwards paths, the energy of the backscattered alpha particle from depth *x* can be writes as [10]:

$$\mathrm{KE_0 - E_1} = \left[\frac{\mathrm{K}}{\cos\theta_1}\frac{\mathrm{dE}}{\mathrm{dx}}(\mathrm{in}) + \frac{1}{\cos\theta_2}\frac{\mathrm{dE}}{\mathrm{dx}}(\mathrm{out})\right]\mathrm{x} \qquad [5.14]$$

8

where the "in" and "out" in refer to the constant values of dE/dx along the inward and outward paths. KE_0 is the energy of the backscattered alpha particles at the surface atoms of the target, while E_1 is the energy of the alpha particle backscattered from the atom at depth *x*.

Taking the difference between E_1 and KE_0 to be ΔE, i.e.

$$\Delta\mathrm{E} = \mathrm{KE_0 - E_1} \qquad [5.15]$$

Then equation 5.14 can be written as:

$$\Delta\mathrm{E} = [\mathrm{S}]\mathrm{x} \qquad [5.16]$$

where :

$$[S] = \left[\frac{\mathrm{K}}{\cos\theta_1}\frac{\mathrm{dE}}{\mathrm{dx}}(\mathrm{in}) + \frac{1}{\cos\theta_2}\frac{\mathrm{dE}}{\mathrm{dx}}(\mathrm{out})\right] \qquad [5.17]$$

[S] is called the energy loss factor that contains the relationship between energy and depth information. It also relates to the energy width δE to the depth resolution δx: $\delta x = \delta E/[S]$.

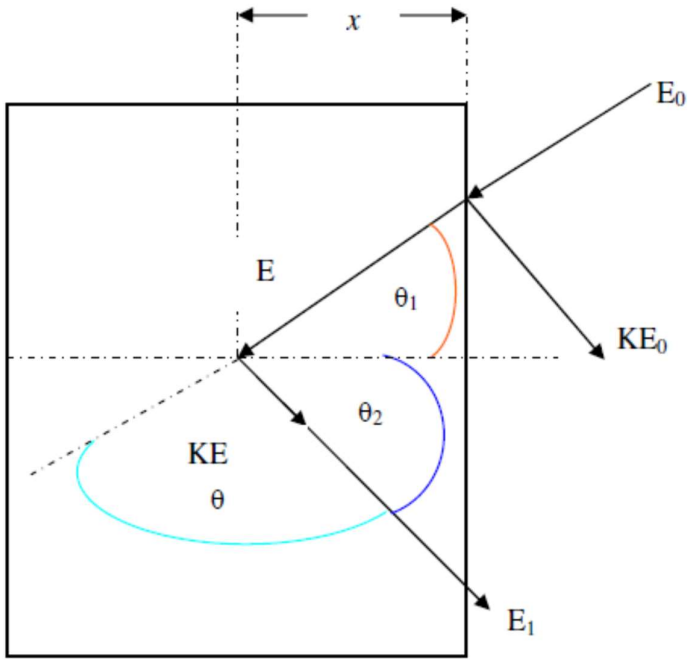

Figure 5-8: *A schematic diagram showing the backscattering events in a target consisting of one of one element. The angles θ_1 and θ_2 are positive regardless of the side on which they lie with respect to the normal of the target [12].*

5.5.3 Differential Cross Section

The probability for a backscattering event to take place is called differential cross section for scattering. i.e $d\sigma/d\Omega$ in a given direction into a solid angle dΩ, and it is defined as the number of particles scattered into the solid angle dΩ per number of incident particles per unit area. The differential cross section for the scattering of a projectile into a solid angle dΩ centered around and angle θ in the laboratory frame of reference [10] is given by:

$$\frac{d\sigma}{d\Omega} = \left(\frac{Z_1 Z_2\ e^2}{4E_0}\right)^2 \frac{4(\sqrt{M_2^2 - M_1^2 \sin^2\theta} + M_2 \cos\theta)^2}{M_2 \sin^4\theta \sqrt{M_2^2 - M_1^2 \sin^2\theta}} \qquad [5.18]$$

and the total number of detected particles can be written as [11]:

$$A = \sigma \Omega Q N \qquad [5.19]$$

where E_0 is the energy of the projectile before scattering, Z_1 is the atomic number of the projectile with mass M_1, Z_2 is the atomic number of the target with mass M_2, e is the electronic charge, A is the number of backscattered particles, Q is the total number of incident projectiles, N is the total number of target atoms per unit area, σ is the differential cross section and Ω is the solid angle of the detector. From equation 5.19 it is clear that N can be calculated when A, Ω, σ and Q and thus the results can be quantified.

By inspection of equation 5.18, the differential cross section is directly proportional to Z_2^2 and inversely proportional to E_0^2 , one deduces that RBS is more sensitive to detection of elements with higher Z and one could therefore expect more backscattered yield if one is working with lower energy compared to high energies.

5.6 Annealing

After the implantations, the samples were annealed in a computer controlled high temperature vacuum graphite furnace (Webb® 77). To prevent contamination the samples were each put in separate graphite crucibles.

5.6.1 Webb furnace

The oven is fitted with a Eurotherm 2704 temperature controller connected to a thermocouple and a pyrometer. The thermocouple is sensitive to temperatures below 1475 °C, while the pyrometer is sensitive to temperatures above 1525 °C. An average value of the thermocouple and the pyrometer is used in the temperature range between the 1475 and 1525 °C set points. The uncertainty in the temperature measurements in the Webb furnace is about $\pm$ 15 °C. Pre-annealing preparations involves the evacuation of the oven to pressures of about 10^{-7} mbar, followed by degassing phase where the oven is heated to 100 °C for one hour to aid the

desorption of water vapour and other gases adsorbed in the fibrous carbon internal high temperature insulation. The degassing also helps in attaining maximum pressure during annealing.

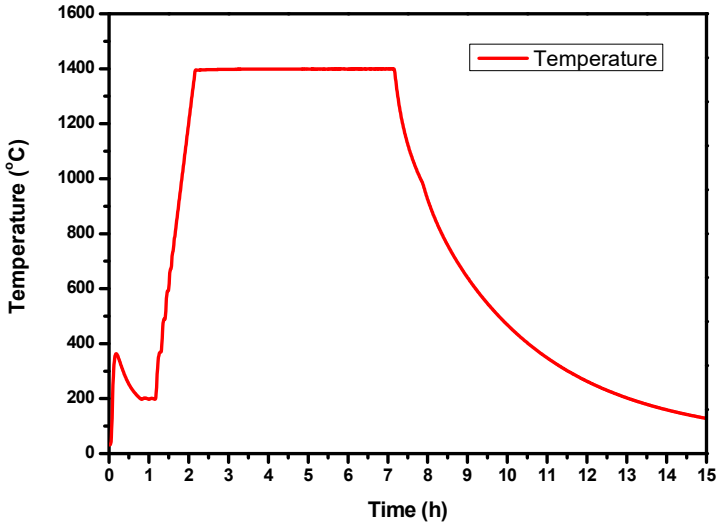

Figure 5-9: *Heating and cooling curve for a sample annealed at 1400 °C for 5 hours.*

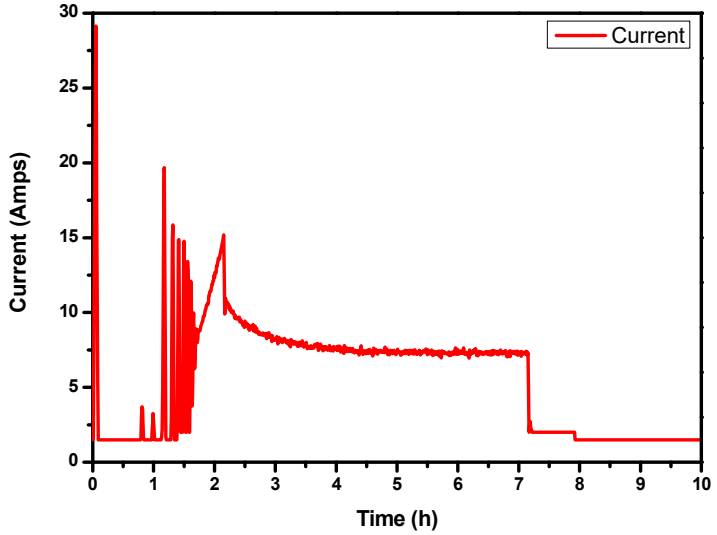

Figure 5-10: *The graph representing the current drawn by the heating element.*

The advantage of degassing is to ensure that maximum pressure is maintained at 10^{-5} mbar region, because most of the gas would have been removed from the chamber. The oven was programmed to a heating rate of 20 °C/min in all the annealing cycles. At the start of the annealing, the heating element draws a large current of about 20 A (see Figure 5-10). Ultimately the current drops to 10 A as the heating starts to be regulated automatically. There is feature that comes in between switching on the heater and the start of the regulation for the current that is observed on the graph, this is due to the increase in the chamber pressure to about 10^{-5} mbar. It is the effects of the high initial current that was drawn by the heater as the heater was switched on. As the current reaches a steady state at around 2.5 hours into the annealing cycle, the base pressure is then reduced to the order of 10^{-6} mbar as the pumping rate increases again surpassing the degassing rate. In this annealing cycle the, the furnace was set to dwell at a temperature of 1400 °C for 5 hours and automatically the furnace stops annealing and starts cooling off naturally. From the radiation law of cooling, the furnace cooling is given by:

$$T(t) = Fexp(-zt) \qquad [5.20]$$

Differentiating the equation 5.21 above gives the cooling rate of the furnace as:

$$\frac{\mathrm{dT}}{\mathrm{dt}} = -\mathrm{FZexp}(-\mathrm{Zt}) \qquad [4.21]$$

Where *F* and *Z* are the constants, *T* is the temperature and *t* is the time. For the Webb furnace the constants *F* and *Z* are 3.09×10^{6} °C and $2.79 \times 10^{-1}\mathrm{h}^{-1}$ respectively as determined by [12].

5.7 References

[1] Klug, H.P. and Alexander, L.E., 1974. *X-ray diffraction procedures: for polycrystalline and amorphous materials* (p. 992).

[2] Barbero, N., Delfino, M., Palmisano, C. and Zosi, G., 2014. Fundamentals of X-Ray Diffraction and X-Ray Interferometry. In *Pathways Through Applied and Computational Physics* (pp. 7-107). Springer, Milano.

[3] Riggs, W.M. and Parker, M.J., 1975. Surface analysis by X-ray photoelectron spectroscopy. *Methods of Surface Analysis*, *1*, pp.150.

[4] Biesinger, M.C., Payne, B.P., Grosvenor, A.P., Lau, L.W., Gerson, A.R. and Smart, R.S.C., 2011. Resolving surface chemical states in XPS analysis of first row transition metals, oxides and hydroxides: Cr, Mn, Fe, Co and Ni. *Applied Surface Science*, *257*(7), pp.2717-2730.

[5] Ferraro, J.R., Nakamoto, K. and Brown, C.W., 2003. Chapter 1-basic theory. *Introductory Raman spectroscopy*, *2*, pp.1-94.

[6] Thermo Fisher Scientific Phenom-World BV 2020 How Does EDX Analysis with a Scanning Electron Microscope (SEM) Work?. AZoM. Retrieved on September 17, 2020 from https://www.azom.com/article.aspx?ArticleID=16256

[7] Hafner, B., 2007. Scanning electron microscopy primer. *Characterization Facility, University of Minnesota-Twin Cities*, pp.1-29.

[8] Choudhary, O.P. and Choudhary, P., 2017. Scanning electron microscope: advantages and disadvantages in imaging components. *Int. J. Curr. Microbiol. Appl. Sci*, *6*, pp.1877-1882.

[9] Van de Graaff, R.J., Compton, K.T. and van Atta, L.C., 1933. VAN DE GRAAFF 1933. *Physics Review*, *43*, p.149.

[10] Kuhudzai, R.J., 2015. *Diffusion and surface effects of SiC implanted with fission product elements* (Doctoral dissertation, University of Pretoria).

[11] Chu, W.K., 2012. *Backscattering spectrometry*. Elsevier.

[12] Hlatshwayo,T.T., 2010. *Diffusion of silver in 6H-SiC PhD Thesis* (University of Pretoria, South Africa)

Chapter six

6. TiN results and discussion

6.1 Characterization of as-sintered TiN

TiN powder was sintered using spark plasma sintering (SPS). Some sets of the sintered TiN samples were implanted with Xe ions of 360 keV to a fluence of 1.1×10^{16} cm $^{-2}$ at room temperature (RT). Others were firstly irradiated with Xe of 167 MeV ions to a fluence of 3.4×10^{14} cm^{-2} at RT and then implanted with Xe ions of 360 keV to a fluence of 1.1×10^{16} cm^{-2} also at RT. The implanted samples were then sequentially annealed in temperatures ranging from 1100 to 1600 ^{o}C in steps of 100 ^{o}C for 5 hours. The as-sintered samples were characterized by SEM, XRD, RS and XPS while the irradiated and implanted then annealed samples were additionally characterized by RBS. This chapter presents and discusses the results from analysis.

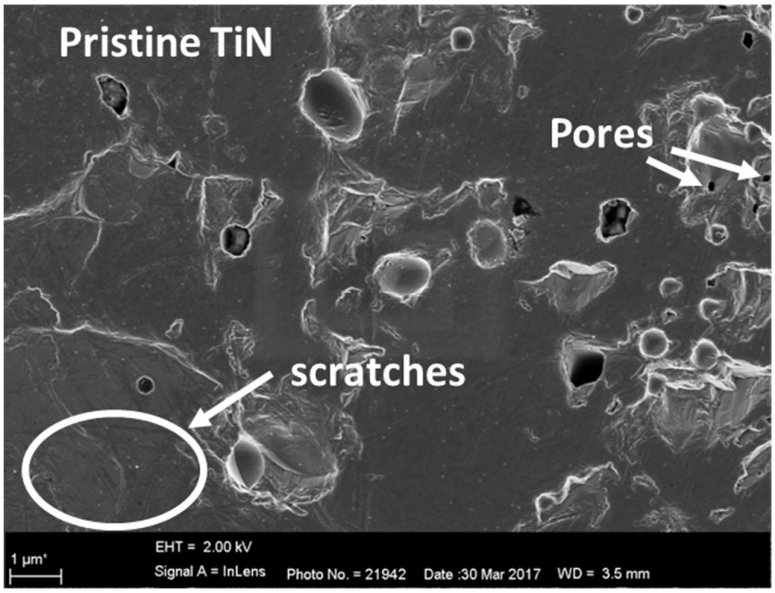

Figure: 6-1: *SEM surface micrograph of the as-sintered TiN.*

Figure 6-1 shows the SEM micrograph of spark plasma sintered TiN. There are few pores on the surface of the as-sintered TiN indicating maximum densification as verified by

Archimedes' principle. A relative density of 98.5 % (TiN theoretical density) equivalent to 5.31 g/cm^{-3} was obtained from Archimedes principle. The scratch marks on the surface are due to polishing that was carried out after cutting the samples into manageable sizes.

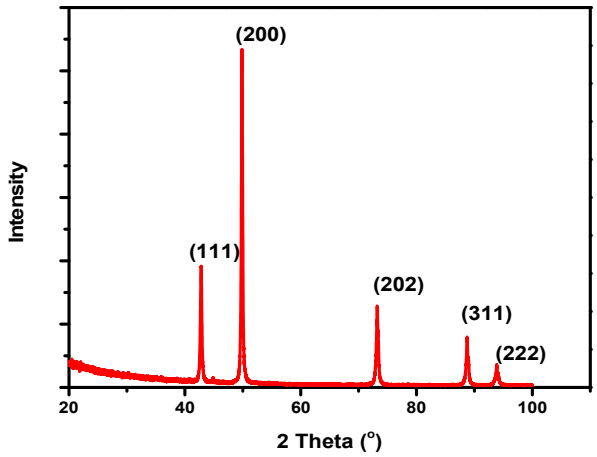

Figure 6-2: *XRD pattern of the as-sintered TiN.*

The XRD pattern of the as-sintered TiN is shown in Figure 6-2. The XRD pattern revealed several sharp peaks at 2θ positions of 42.9, 49.9, 73.2, 88.8 and 93.8 ° corresponding to (111), (200), (202), (311) and (222) TiN planes according to International center for diffraction data (ICDD) File number: 03 065 8417, indicating the polycrystalline nature of the as-sintered TiN. The average crystalline size was found to be 28 nm using the Scherrer equation:

$$D = \frac{0.9\lambda}{\beta\cos\theta} \qquad [6.1]$$

where D is the mean crystallite size, β is FWHM, λ the wavelength of the X-rays (1.798 nm) and θ is the Bragg angle [1].

The Raman spectrum of as-sintered TiN is shown in Figure 6-3 together with the fitted spectrum. The measured spectrum consists of four peaks at 236, 321, 442 and 557 cm^{-1}. The peaks at 236, and 321 cm^{-1} are the first order Raman scattering corresponding to longitudinal acoustic (LA) and transverse acoustic (TA) modes. The broad peak at 557 cm^{-1} is transverse

optical (TO) mode. The acoustic modes are attributed to the vibrations of the Ti atoms while the optical modes are attributed to N vibrations [2]. The band at 442 cm^{-1} due to presence of titanium oxide [3]. TiN is known to have NaCl type (fcc) structure and to undergoes octahedral symmetry (O_h). In a perfect NaCl structure only the zone centre phonons can be Raman active, and usually not even all of them. The selection rules for Raman do not allow O_h symmetry, therefore first order scattering is forbidden in TiN [2]. Although the first order Raman scattering is forbidden in TiN, the presence of defects in TiN results in the detection of the first order scattering. Hence the sintered TiN had defects. The presence of TiO_2 is attributed to oxidation of the TiN surface. The oxidation might have taken place during polishing as it was done in air. The Raman spectrum was fitted using the Gaussian-Lorentzian profile (Figure 6-3). The Raman spectrum fitted well with peaks at 236, 321, 442, 557 and 614 cm^{-1}. The peak at 614 cm^{-1} is attributed to the optical mode of the TiO_2 phase [3]. The Raman spectra had peaks which indicates the presence of defects in the as-sintered TiN.

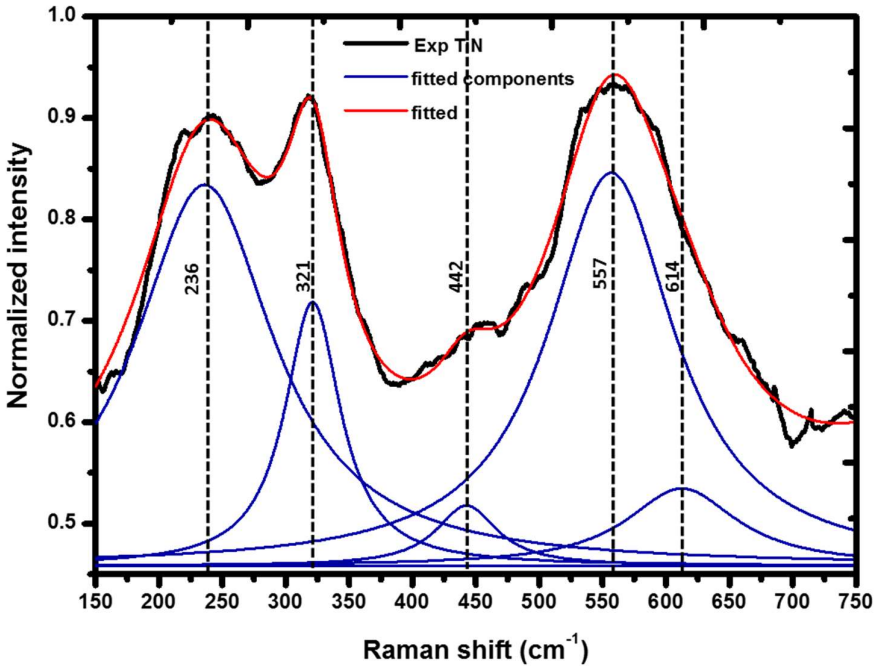

Figure 6-3: *Raman spectrum of as-sintered TiN, fitted and fitted components (Lorentzian-Gaussian).*

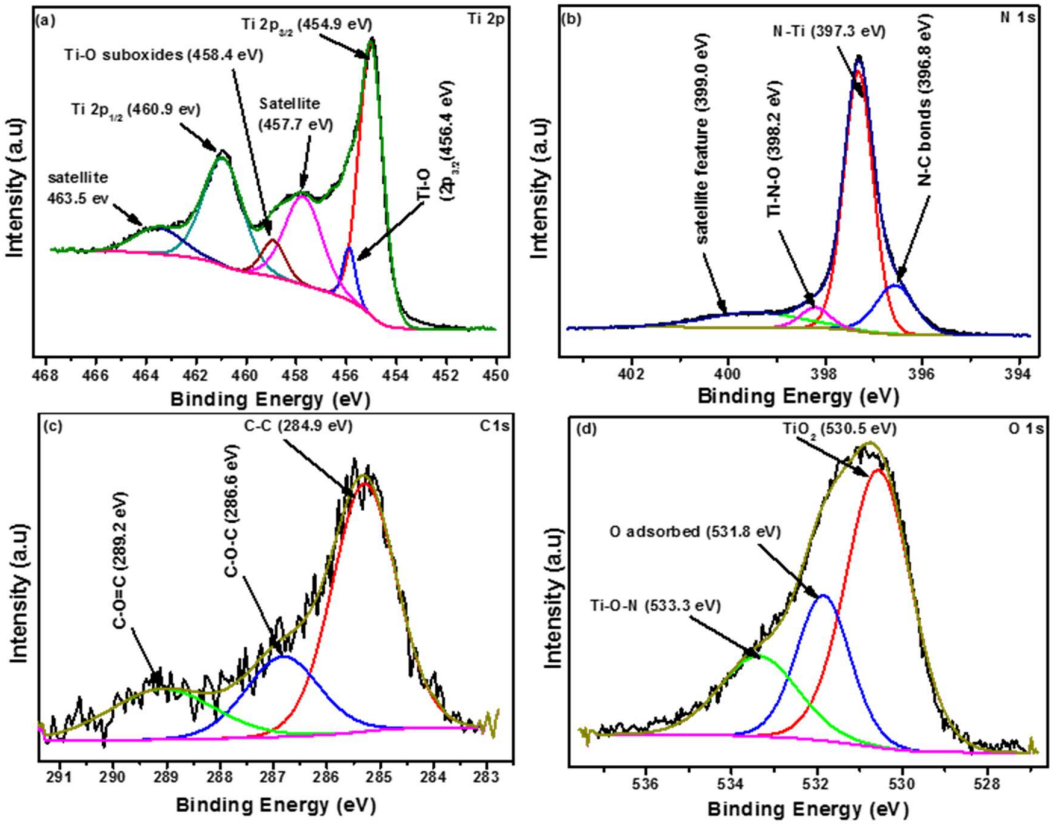

Figure 6-4: *High resolution XPS spectra of (a) Ti 2p, (b)N 1s, (c) C 1s and (d) O1s with their fitted components.*

The composition and chemical states of the as-sintered TiN was further characterized by XPS. The high resolution XPS spectrum of Ti2p shown in Figure 6-4 (a) displays Ti $2p_{3/2}$ and $Ti2p_{1/2}$ peaks positioned at binding energy of 454.9 and 460.9 eV, respectively consistent with the Ti – N bonds in TiN [4]. The spin-orbit difference between the Ti 2p doublets is 6.0 eV indicating that the bonding state of Ti was in the form of TiN [4]. The fitted TiN spectrum showed a peak located at binding energy of 456.4 eV corresponding to the Ti-O bonds and a peak at 458.4 eV attributed to the sub-oxides of TiO_2 [4,5]. The latter indicates that the surface of the samples was oxidized. The observed satellite peaks at binding energy ~2.7 eV higher than the $Ti2p_{3/2}$ and $Ti2p_{1/2}$ peaks differentiates TiN from TiO_2. Figure 6-4 (b) shows the N 1s high resolution spectrum. This spectrum fitted well with three components located at 396.8, 397.3 and 398.2

eV using Gaussian function. The first component from the low binding energy side (396.8 eV) could be attributed to surface carbon-nitrides (N-C) bonds [5]. The main peak at 397.3 eV was assigned to N bonded to Ti forming TiN [4,6]. The peak at 398.2 eV originates from titanium oxynitrides and the relatively low intense component centered at 399.0 eV is due to the presence of the free nitrogen at the interstitial sites [4,7]. Figure 6-4 (c) shows the spectrum of C1s with a prominent peak at 284.9 eV which could be attributed to C-C. The remaining two peaks at 286.6 and 289.2 eV were attributed to adventitious peaks of C-O-C bond and C-O=C, respectively [8]. There is a possibility of adventitious carbon and oxygen that contaminated the samples during polishing and storage as they were polished and stored in an open environment. O1s core level photoelectron fitted with three different fragments as shown in Figure 6-4 (d). The first component at 530.5 eV is ascribed to TiO_2, the second component at 531.8 eV is assigned as the elemental O (or physically adsorbed molecular H_2O) and the third component at 533.3 eV is identified to be originated from Ti-O-N phase [8]. These results agree with Raman results which also indicated the oxidation of the samples surfaces.

6.2 Irradiation of TiN

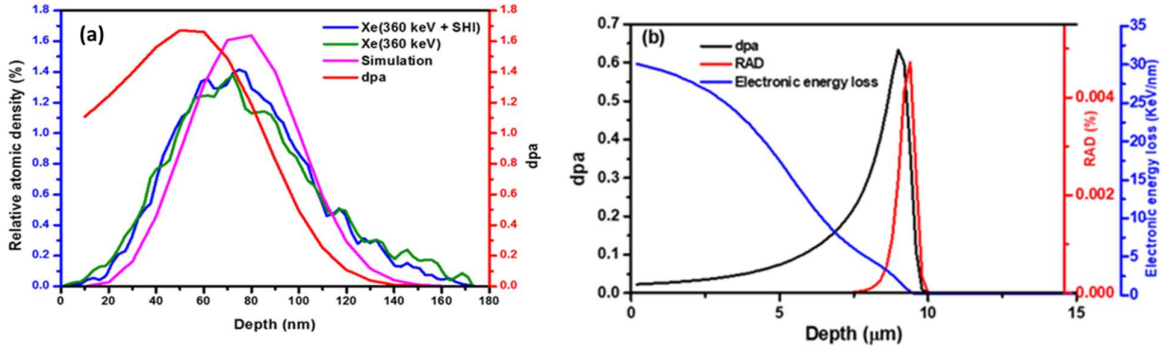

Figure 6-5: *(a) Depth profiles of Xe ions of 360 keV implanted into TiN at room temperature to a fluence of 1.1×10^{16} cm^{-2}, Xe ions of 360 keV implanted into TiN (pre irradiated with Xe ions of 167 MeV to a fluence of 3.4×10^{14} cm^{-2} at room temperature) to fluence of 1.1×10^{16} cm^{-2} at RT and SRIM simulated Xe of 360 keV implanted into TiN. The simulated damage in displacement per atom (dpa) is included. (b) TiN SRIM simulated results of Xe ions of 167 MeV implanted into TiN to a fluence of 3.4×10 ^{14} cm $^{-2}$ at RT.*

Figure 6-5 (a) and (b) shows the SRIM simulated results of 360 keV Xe ions implanted into TiN to a fluence of 1.1×10^{16} cm^{-2} at RT and 167 MeV ions irradiated into TiN to a fluence of 3.4×10^{14} cm^{-2} also at RT respectively. The measured RBS profiles of Xe ions of 360 KeV implanted into TiN (Xe-360 keV) and Xe ions of 360 keV implanted into TiN pre-irradiated with Xe ions of 167 MeV (Xe-360 keV+SHI) are also included. The fluence was converted into displacement per atom (dpa) using [9]:

$$\text{dpa} = \frac{\frac{\text{Vac}}{\text{ion Å}} \times 10^{8}}{\rho_{\text{TiN}}(\text{atoms}^{-3})} \times \varphi(\text{ions cm}^{-2}) \qquad [6.2]$$

where φ is the ion fluence, ρ_{TiN} is the theoretical density of TiN in *atcm^{-3}* (10.48 ×10 ^{23} at□cm $^{-3}$) and $\frac{\mathbf{Vac}}{\mathbf{ion Å}}$ is the vacancy per ion from SRIM 2012 [10]. A detailed calculation with full

damage cascades was used in both simulations. The threshold displacement energies of 28 eV and 25 eV for the N and Ti sublattices were used.

The measured Xe depth profiles from Xe-360 keV and Xe-360 keV+SHI samples are identical and slightly broader but in reasonably agreement with SRIM simulated Xe profile. The experimental projected ranges (Rp) of implanted Xe are about 72.6 nm and 79.3 nm in Xe-360 keV and Xe-360 keV+167 MeV samples which are in reasonable agreement with Rp of about 70.3 nm from SRIM. The retained damage is closer to the surface compare to projected range. The maximum dpa of about 1.60 at 50.0 nm and of about 0.62 at of 9.10 um are retained in Xe-360 keV and Xe-360keV + SHI respectively. From these results, it is quite clear that SHI irradiation prior to Xe implantation had insignificant effect on the distribution of implanted Xe. SHI irradiation exposed the TiN mostly to electronic energy loss while Xe implantation exposed the samples to nuclear energy loss. Hence, interaction of the defects retained by SHI and slow-moving ions in the Xe-360 keV + SHI samples is expected.

Raman spectra of Xe-360 keV and Xe-360 keV + SHI samples compared with the Raman spectrum of pristine TiN (Virgin) are shown in Figure 6-6. The Raman spectra of both Xe-360 keV and Xe-360 keV + SHI retained all the characteristic Raman peaks indicating lack of amorphization after both treatments. Implantation of Xe 360-keV resulted to a slight combination of the peaks in the 200 and 350 cm^{-1} region accompanied by the broadening of the optical band. These observations indicate accumulation of defects after implantation. Similar combination of the acoustic bands accompanied by broadening of the optical band indicating accumulation of defects were observed in the Raman spectrum of Xe-360 keV + SHI. To get more insight on the radiation damage retained in both the samples, the Raman spectra of both the samples were fitted by Lorentzian- Gaussian profile.

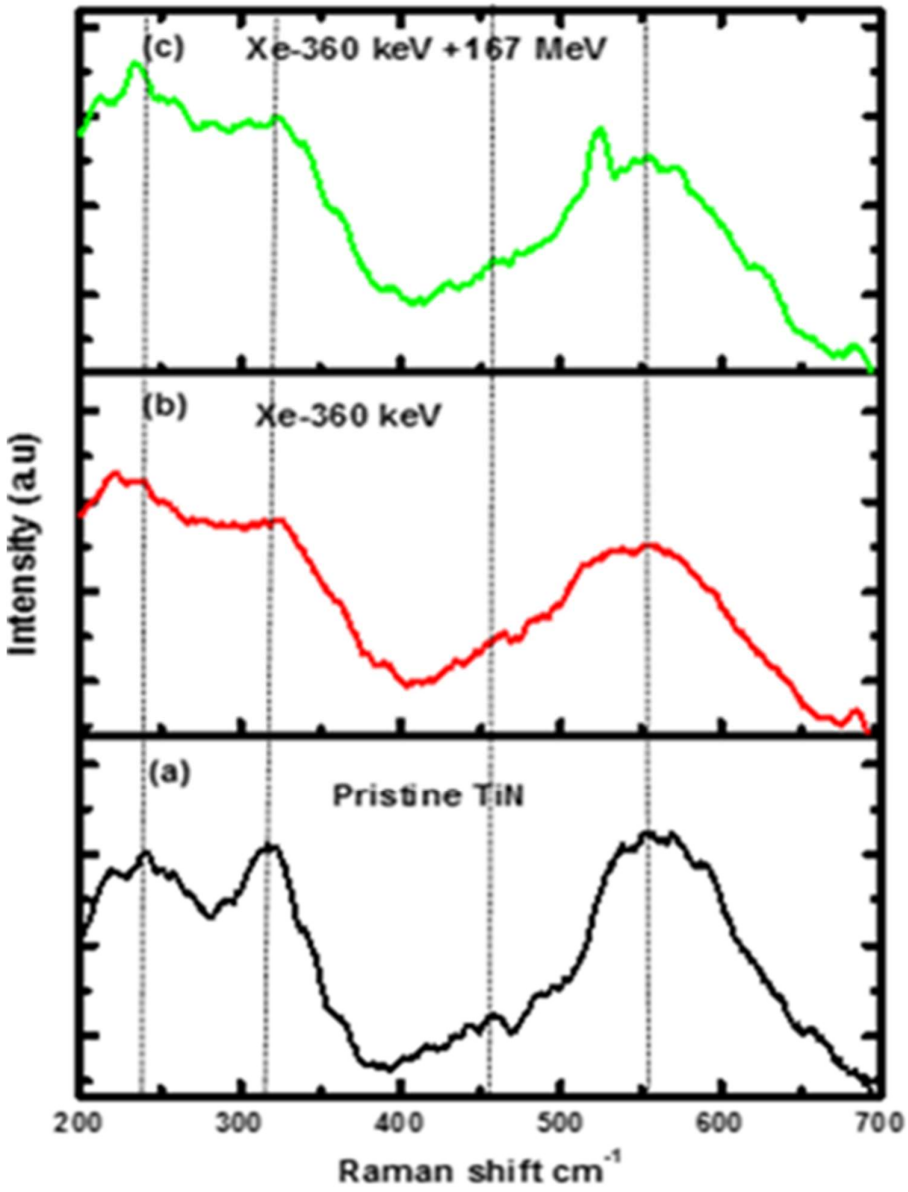

Figure 6-6: *Raman spectra of TiN implanted with Xe of 360 keV to a fluence of 1.1×10^{16} cm^{-2} at RT (Xe-360 keV) and co-irradiated with Xe of 167 MeV to a fluence of 3.4×10^{14} cm^{-2} and with Xe ions of 360 keV to a fluence of 1.1×10^{16} cm^{-2} respectively (Xe-360 keV+167), the spectra of pristine TiN is included for comparison.*

Figure 6-7 shows the Raman spectra of Xe-360keV and Xe-360keV+SHI samples together with their corresponding fitted spectra. The fitted spectrum of Xe-360 keV reveals that the TA mode has shifted from 236 to 224 cm^{-1}, the LA mode shows an insignificant shift from 321 to 319 cm^{-1}, while the TiO_2 peak shifted from 442 to 449 cm^{-1}. The TO peak also shifted from

557 to 545 cm^{-1}. The oxide peak shoulder which is observed at 614 cm^{-1} in the pristine samples has shifted to 587 cm^{-1}. The fitted Raman spectrum of Xe-360 keV+SHI showed no significant shift of TA mode while the LA mode shifted from 321 to 326 cm^{-1}. The TiO_2 peak shifted from 442 to 452 cm^{-1}, while a TiO_2 peak at 614 shifted to 604 cm^{-1}. These differences in peak shifts either to lower or higher wavenumbers indicate the different stress in Xe-360 keV and Xe-360 keV+SHI samples. The full width at half maximum (FWHM) of the TO mode peaks were calculated from the fitted spectra. They were found to be 91, 125 and 105 for pristine, Xe-360 keV and Xe-360 + SHI, respectively. The broadening of the TO peaks indicates relative amount of defects retained. Therefore, relatively more defects/damages were retained in the Xe-360 keV compared to Xe-360 keV+ SHI samples. The different concentration of defects retained in the Xe-360 keV and the Xe-360 keV + SHI might be due to interaction of defects in the latter. Since SHIs lose energy due to electronic energy loss and they traverse in straight lines deep into the target material. Generally, these results indicate that irradiating with slow moving ions and co-irradiation with both slow and swift heavy ions did not cause any severe damage in the TiN. Similar radiation tolerance has been reported in TiN irradiated with slow moving ions [11, 12, 13,14]. Popovic *et al.* irradiated TiN films with Ar ions of 200 keV to a highest fluence of 2×10^{16} ions/cm^2 [12], Xue *et al.* irradiated TiN films with 100 keV Ar ions to a fluence of 3×10^{17} ions/cm^2 at 600 °C [13] and Wang *et al* irradiated TiN films with He ions of energies ranging from 12 keV to 35 keV to a fluence of 4×10^{16} cm^{-2} and 1×10^{17} cm^{-2} at RT [14]. In all these studies, no amorphization was reported which demonstrated the resilience of TiN to radiation damage.

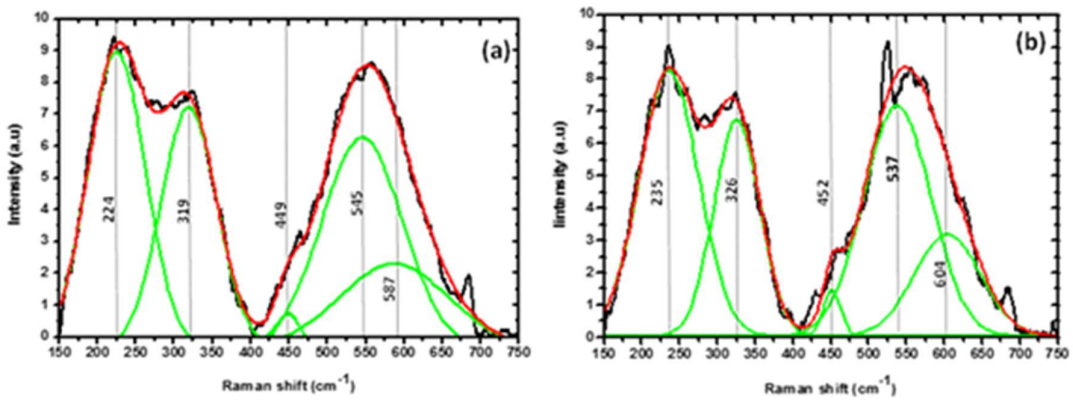

Figure 6-7: *(a) Raman spectrum of sintered TiN implanted with Xe-360 keV to a fluence of 1.1×10^{16} cm^{-2} at RT, fitted and fitted components (Lorentzian- Gaussian) and (b) The Raman spectrum of sintered TiN co-irradiated with Xe-360keV + SHI to fluences of 1.1×10^{16} and 3.4×10^{14} cm^{-2}respectively at RT, fitted and fitted components (Lorentzian- Gaussian).*

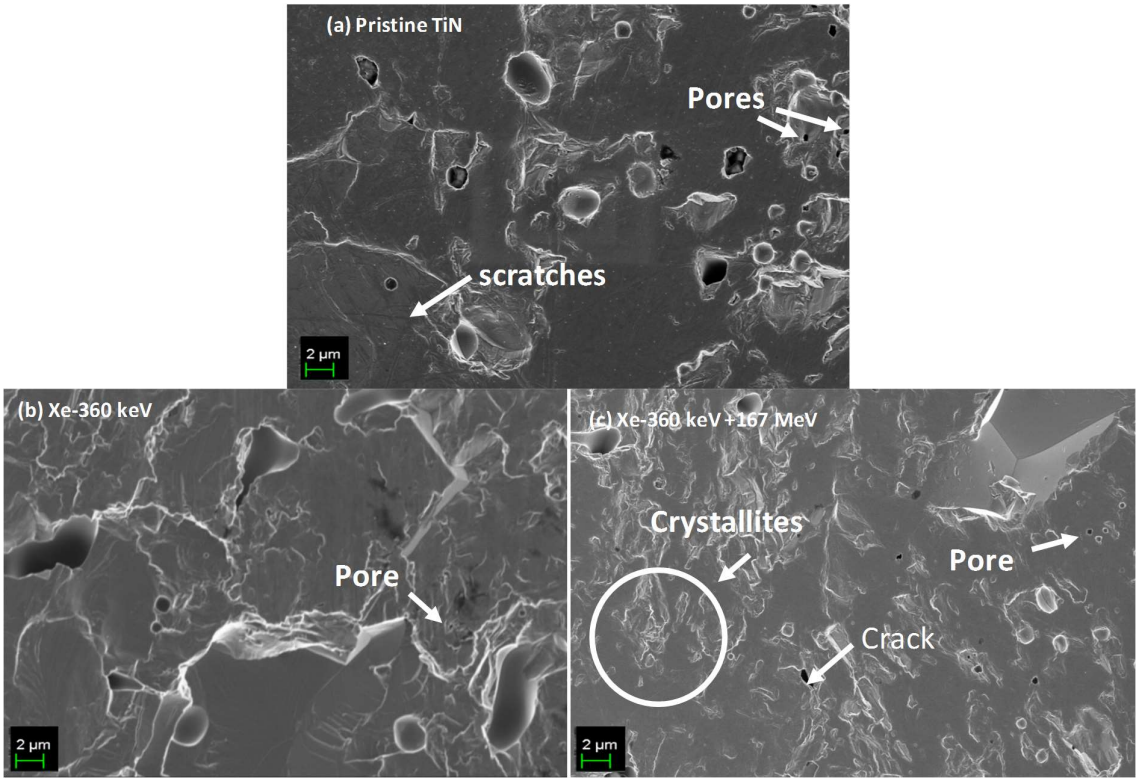

Figure 6-8: *SEM micrographs of the (a) Pristine TiN, (b)TiN implanted with Xe ions of 360 keV to a fluence of 1.1×10^{16} cm^{-2} at room temperature (Xe-360 keV) and (c) co-irradiated with Xe ions of 167 MeV to a fluence of 3.4×10^{14} cm^{-2} and implanted with Xe ions of 360 keV to a fluence of 1.1×10^{16} cm^{-2} respectively (Xe-360 keV +SHI).*

SEM micrographs of Xe-360 keV and Xe-360 keV+SHI samples are shown in Figure 6-8, the SEM micrograph of pristine TiN is included for comparison. Except the appearance of larger crystals on the surface of Xe-360 keV samples, the surface of Xe-360 keV samples is similar to that of pristine samples. The Xe-360 keV+ SHI samples have bigger crystals (like the ones observed in Xe-360 keV samples), some finer crystals of different sizes also appeared on the surfaces. The difference might be caused by localized heat during SHI irradiation before implantation or interaction of defect retained by SHI irradiation and slow ions implantation.

6.3 Annealing of implanted TiN

Xe-360 keV and Xe-360 keV+SHI samples were sequentially annealed at temperatures ranging from 1100 to 1500 ℃ in steps of 100 ℃ for 5 hours. The Raman spectra of the annealed samples are presented in Figure 6-9, with pristine TiN, as-implanted Raman spectra of Xe-360 keV and Xe-360 keV+SHI Raman spectra included for comparison. Annealing the Xe-360 keV samples at 1100 ℃ resulted in a slight combination of TA and LA modes accompanied by a blue-shift from 236 and 321 to 189 and 292 cm^{-1}, respectively. A blue-shift of the TO mode from 557 to 533 cm^{-1} accompanied by the narrowing of FWHM compared to the implanted and pristine was also observed. The shift is attributed to stress in the implanted samples while slight combination of TA and LA mode together with narrowing indicated the reduction in defect concentration after annealing at this temperature. Annealing at 1200 ºC resulted in significant combination of TA and LA modes with TO mode remaining at 533 cm^{-1} indicating more reduction of defect concentration after annealing at this temperature. This reduction in defects concentration progressed with annealing temperature and at 1300 ℃ a new peak attributed to LO mode of TiN in the region between 600 and 700 cm^{-1} emerged. This peak became more prominent as the annealing temperature was increased up to 1500 ℃. The LO mode was clearly visible at 630 cm^{-1} after annealing at 1500 ℃.

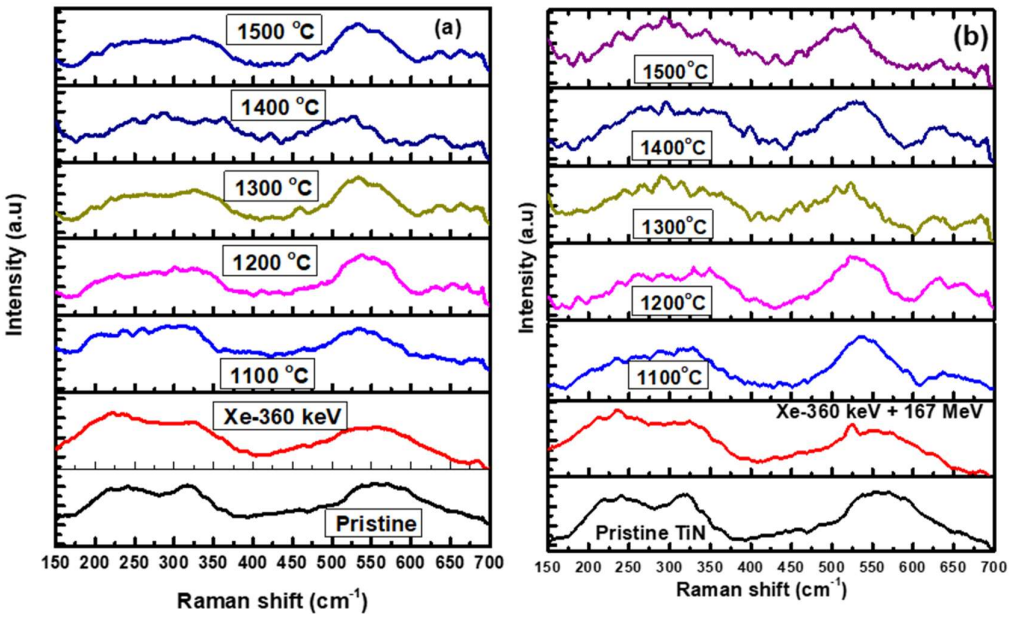

Figure 6-9: *Raman spectra of Xe-360 KeV and Xe-360 KeV +SHI TiN after being isochronally being annealed at different temperatures from 1000 °C to 1500 °C at 5hour cycles. The Raman spectrum of the pristine TiN is included for comparison.*

Annealing the Xe-360 keV +SHI samples at 1100 °C resulted to the combination of TA and LA peaks and narrowing of the TO mode (which shifted from 557 to 536 cm^{-1}) similar to the Xe-360 keV annealed at 1100 °C. The appearance of the LO mode at 635 cm^{-1} after annealing at this annealing temperature (1100 °C) was also observed. As the annealing temperature was increased, a combination of TA and LA modes became prominent while the TO mode remained at 536 cm^{-1}. Comparing these results with what Xe-360 keV (which showed no LO mode) after annealing at 1100 °C), suggests that faster annealing of defects in the Xe-360 keV + SHI samples. This was expected as less defect concetration was retained in the latter samples as expalined earlier section 6.2.

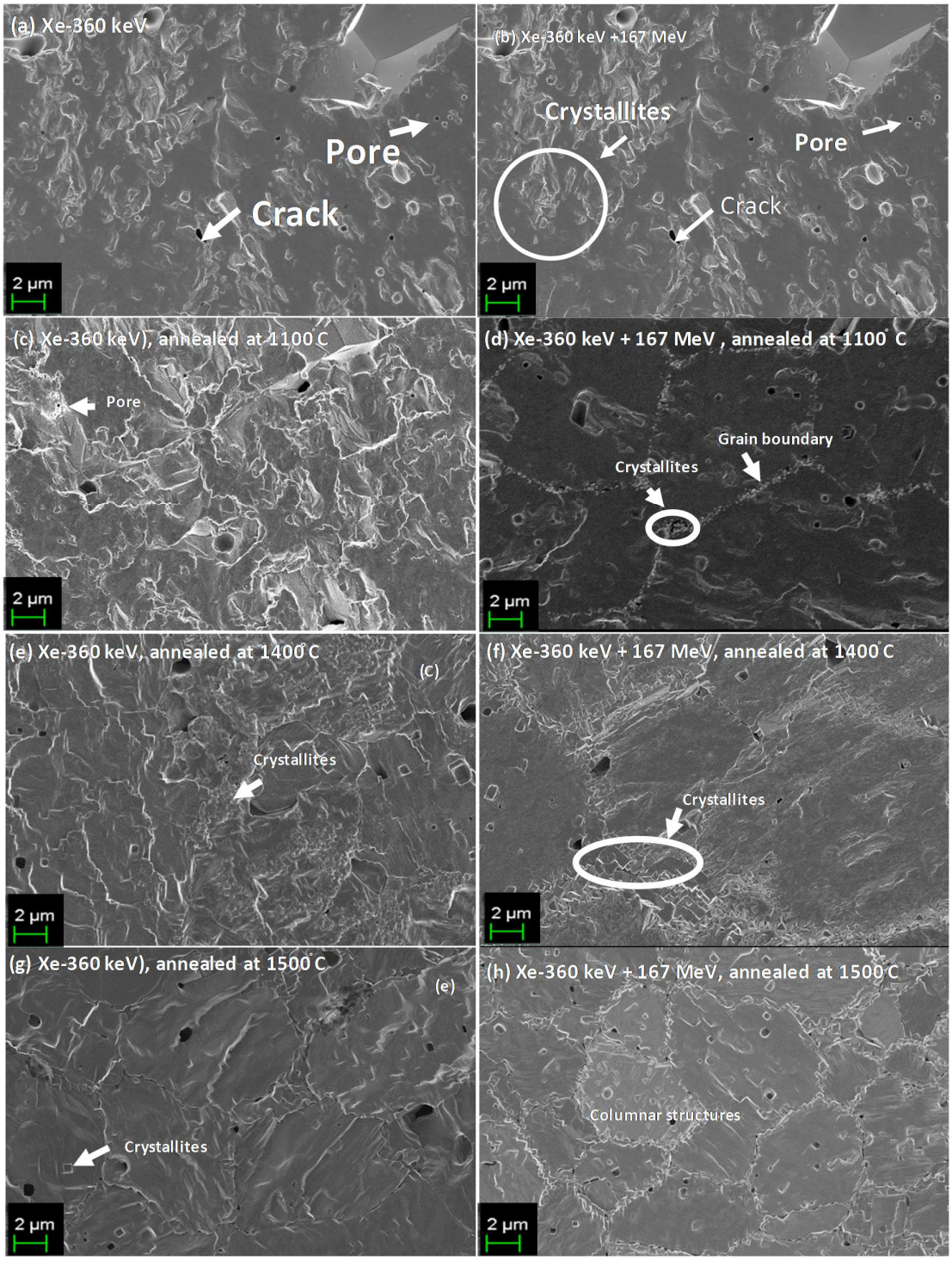

Figure 6-10: *SEM micrographs of Xe-360 keV and Xe-360 keV+SHI after being subsequently annealed at 1100, (1200, 1300, not shown here), 1400 °C, 1500 °C, with (a) the as-implanted (b) as-implanted + SHI micrographs for comparison.*

Morphological evolution of the sample surfaces was investigated after each annealing cycle using SEM. Figure 6-10 shows the SEM micrographs of Xe-360 keV and Xe-360 keV+SHI samples before and after annealing. Annealing the Xe-360 keV samples at 1100 °C did not show any significant change on the surface as compared to the Xe-360 keV as-implanted surfaces. At higher annealing temperatures, the surface became smoother and with less distinct grain boundaries appeared. The grains were relatively becoming smaller.

Annealing the Xe-360 keV + SHI samples at 1100 °C caused some smoothening of the surfaces and appearance of distinct grain boundaries with crystallites forming along their interface. Increasing the annealing temperature resulted in the increase in grain boundaries. Similar increase in number of grain boundaries after annealing has been observed by Bes' *et al.* [15]. Bes *et al.* implanted sintered TiN with Xe ions of 800 keV to a fluence of 5×10^{15} cm^{-2} followed by annealing the at 1500 °C for 1 and 5 h under a vacuum of about 5×10^{-6} mbar. The results showed that there was heterogenous crystallite formation after heat treatment and they concluded that the crystallite formation and the Xe mobility could be attributed to the orientation of each considered grain. Contrary to these results, Bes' *et .al* [15] also observed flaking which was directly linked to Xe bubbles after annealing. No indication of bubbles were observed in annealed Xe-360 keV and Xe-360 keV + SHI samples. The difference in the surface features of the annealed samples might be due to different annealing of defects at different temperatures as observed in Raman results. In the Xe-360 keV + SHI samples, the slow ions were implanted in an already defective TiN. The pre-existing defects interacted with defects caused by implantation which resulted in the formation of complex defects. In the Xe-360 keV, the implantation was performed in a pristine TiN, therefore, the defects were only retained by implantation. Annealing these samples at 1100 °C caused faster annealing of defects in the Xe-360 keV + SHI samples compared to Xe-360 keV as was observed in the

Raman results (Figure 6-9). The smaller crystals in the Xe-360 keV + SHI samples might be due to relatively faster annealing of the defects in these samples.

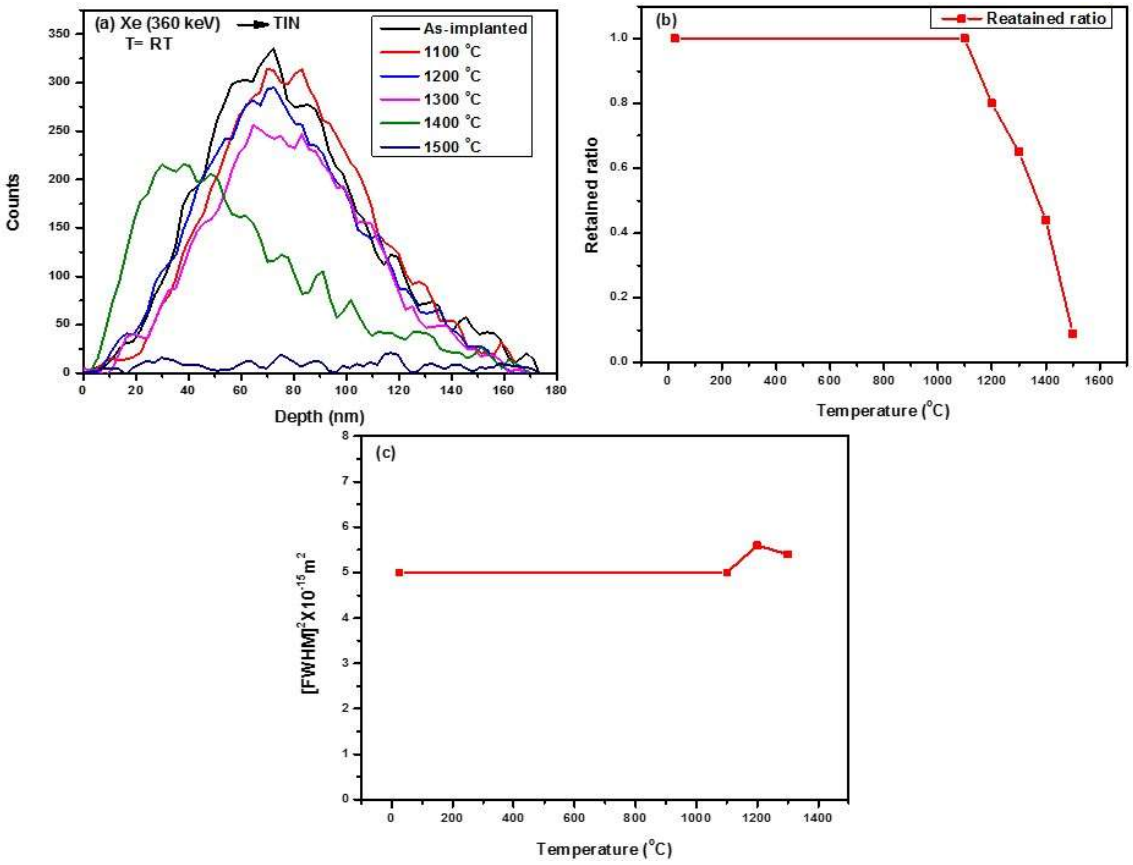

Figure 6-11: *(a) Depth profiles of Xe(360 keV) implanted into TiN to a fluence of 1.1×10^{16} cm^{-2} at room temperature (RT) after isochronal annealing at temperatures from 1100 to 1500 °C for 5hours, the as-implanted Xe depth profile is included for comparison (b) retained ratio of implanted Xe and (c) square of full width at half maximum (FWHMs) of implanted Xe profile as a function of temperature.*

The Xe depth profiles of Xe-360 keV and Xe-360 keV +SHI samples (before and after annealing), their Xe retain ratios and squares of FWHMs as function of temperature are depicted in Figure 6-11 and 6-12. Annealing the Xe-360 keV samples at 1100 °C caused a shift

of Xe peak towards the bulk. This shift was not accompanied by either broadening or loss of the implanted Xe indicating the lack of Fickian type of diffusion after annealing at this temperature. Sequentially annealing at 1200 °C caused a peak shift towards the surface resulting in the Xe peak returning to its original projected range position. This was accompanied by slight broadening of the Xe peak indicating Fickian diffusion and 20 % loss of implanted Xe. Neither further broadening of Xe peak nor shift was observed after annealing at 1300 °C but about slightly ≤ 40 % of the implanted Xe was lost. Further peak shift towards the surface was observed after annealing at 1400 °C. This was accompanied by 60 % loss of Xe from the surface. Furthermore, the surface side of the Xe profile became truncated indicating a direct release of implanted Xe from the surface after annealing at this temperature. This shift towards the surface resulted in the subsequent loss of almost all the implanted Xe after annealing at 1500 °C.

Annealing the Xe-360 keV+ SHI samples at 1100 °C caused no measurable change in the implanted Xe profile Figure 6-12(a). About 15% was lost after annealing at 1200 °C. This was accompanied by no peak broadening and shift. This loss without peak broadening and shift became significant with annealing temperature resulting in the total loss of implanted Xe at 1500 °C. These results indicate the lack of Fickian diffusion in the Xe-360 keV +SHI samples.

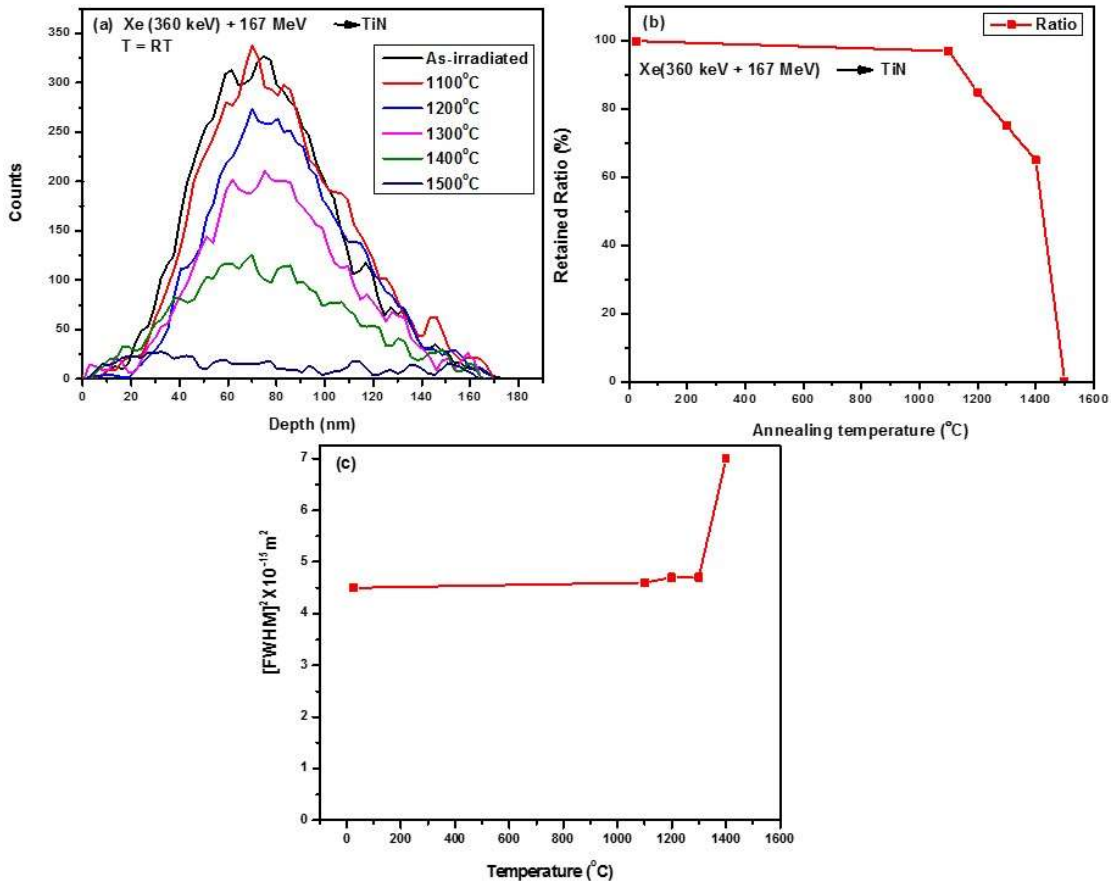

Figure 6-12: *(a) Depth profiles of Xe(360 keV) implanted into TiN (pre irradiated with Xe (167 MeV)) to a fluence of 1.1×10^{16} cm^{-2} at room temperature (RT) after isochronal annealing at temperatures at from 1100 to 1500 °C for 5hours, the as-implanted Xe depth profile is included for comparison, (b) the retained ratio of Xe (c) Square of Full width at half maximums (FWHMs) as function of temperature.*

Comparing these results, it is quite clear that the migration behavior of Xe in the Xe-360 keV and Xe-360 keV +SHI samples is totally different. The different behavior might be due to difference in the radiation damage retained in both samples and their annealing resulting different structures. After annealing at 1100 °C, Raman results indicated more annealing of defects in the Xe-360 keV +SHI samples compared to Xe-360 keV samples. The defects in the

Xe-360 keV samples (which are more towards the surface as predicted by SRIM) might be enough to hinder the implanted Xe from moving towards the surface. This resulted in the peak shifting towards the bulk where there are relatively less defects. Annealing of more defects at 1200 °C caused implanted Xe to shift towards the surface and diffused out. The significant Xe loss (about 30 %) observed after annealing at 1300 °C caused no further Fickian diffusion and shift indicating a radiation enhanced diffusion.

In the Xe-360 keV-SHI samples, significant healing of defects occurred after annealing at 1100 °C. This resulted in no detectable Fickian diffusion and peak shift. The loss of implanted Xe without diffusion might be due to visible grain boundaries with crystallites as seen on the SEM images. These grain boundaries increased in numbers as the annealing temperature was increased resulting in more loss of implanted Xe. Therefore, radiation damage/defects concentration in TiN and structure play a major role in the migration behaviour of implanted Xe. The influence of structure in the migration of Xe implanted into TiN has been reported by Bes' *et al* [15]. They reported that the formation of crystallite and xenon mobility are both related to crystalline orientation. Moreover, they also reported similar observations to this study where Xe depletion was through grain boundaries, which was more prominent in the co-irradiated samples.

Since the as-implanted Xe profiles were almost Gaussian. (see Figure 6-13), the diffusion coefficient (D) of Xe in Xe-360 keV samples was evaluated by fitting the depth profiles to a solution of the Fickian diffusion equation for an initially Gaussian profile [17]. An example of a Gauss fit is shown in Figure 6-13 for both as-implanted samples. The diffusion coefficients of 1.90×10^{-21}, 6.21×10^{-21}, 51×10^{-21} and 1.25×10^{-20} m^2s^{-1} at 1100, 1200, 1300, and 1400 °C were determined for Xe-360 keV samples. Since no broadening was observed in the annealed Xe-360 keV+SHI samples, the diffusion coefficients were not obtained for these samples. From

an Arrhenius plot, shown in Figure 6-14, an activation energy of 1.4 eV and pre-exponential factor (D_o) of $D_o = (1.4 \pm 0.5)\times10^{-16}$ m^2/s were obtained. There is no or very little knowledge on diffusion parameters of Xe implanted into TiN has been reported in literature, hence the results in this study were not compared with literature.

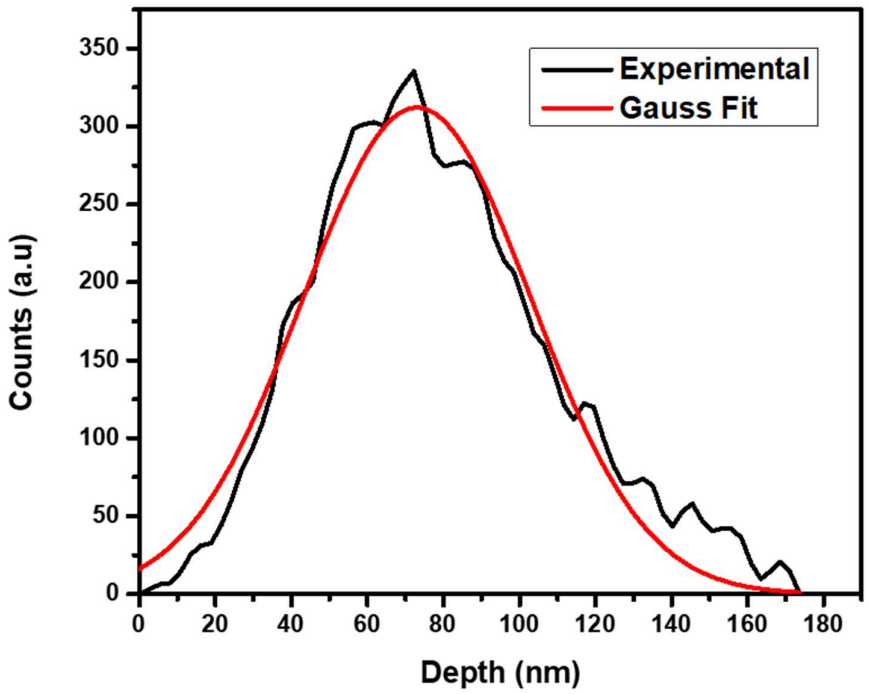

Figure 6-13: *A typical MATLAB program fitted RBS Xe depth profile of as- implanted Xe-360 keV-RT- TiN.*

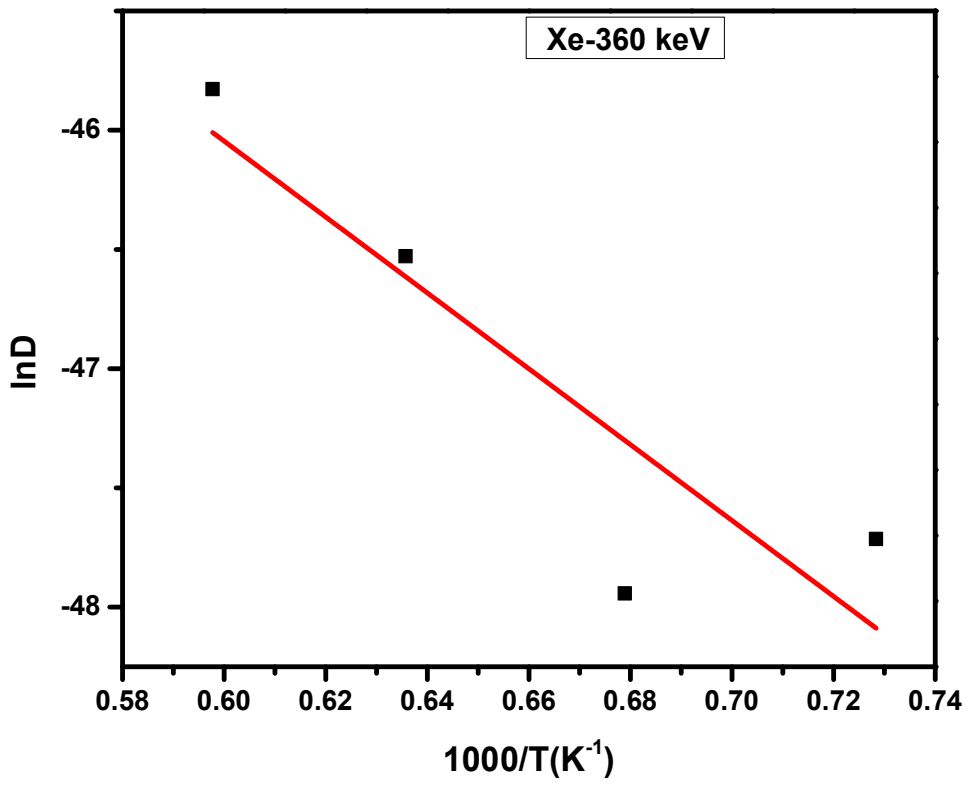

.

Figure 6-14: *Arrhenius plot of the diffusion coefficients of Xe-360 keV sequentially vacuum annealed for 5 h at 1100 °C, 1200 °C and 1300 °C and 1400 °C.*

6.4 References

[1] Cullity, B.D., and Stock, S.R., 1978. Principles of X-ray diffraction. Rading, MA: Addison-Wesley, pp. 90-95

[2] Chen, C.C., Liang, N.T., Tse, W.S., Chen, I.Y. and Duh, J.G., 1994. Raman spectra of titanium nitride thin films. *Chinese journal of physics*, *32*(2), pp.205-210.

[3] Barshilia, H.C. and Rajam, K.S., 2004. Raman spectroscopy studies on the thermal stability of TiN, CrN, TiAlN coatings and nanolayered TiN/CrN, TiAlN/CrN multilayer coatings. *Journal of Materials Research*, *19*(11), pp.3196-3205.

[4] Rahman, M.M., Jiang, Z.T., Munroe, P., Chuah, L.S., Zhou, Z.F., Xie, Z., Yin, C.Y., Ibrahim, K., Amri, A., Kabir, H. and Haque, M.M., 2016. Chemical bonding states and solar selective characteristics of unbalanced magnetron sputtered Ti x M 1− x− y N y films. *Royal Society of Chemistry advances*, *6*(43), pp.36373-36383.

[5] Cheng, Y.F.Z.Y. and Zheng, Y.F., 2007. Characterization of TiN, TiC and TiCN coatings on Ti–50.6 at.% Ni alloy deposited by PIII and deposition technique. *Surface and Coatings Technology*, *201*(9-11), pp.4909-4912.

[6] Han, Y., Yue, X., Jin, Y., Huang, X. and Shen, P.K., 2016. Hydrogen evolution reaction in acidic media on single-crystalline titanium nitride nanowires as an efficient non-noble metal electrocatalyst. *Journal of Materials Chemistry A*, *4*(10), pp.3673-3677.

[7] Bertoti, I., Mohai, M., Sullivan, J.L. and Saied, S.O., 1995. Surface characterisation of plasma-nitrided titanium: an XPS study. *Applied surface science*, *84*(4), pp.357-371.

[8] Greczynski, G. and Hultman, L., 2017. C 1s peak of adventitious carbon aligns to the vacuum level: dire consequences for material's bonding assignment by photoelectron

spectroscopy. *Eouropian Journal of Chemical Physics and Physical Chemistry*, *18*(12), p.1507.

[9] Fisher, D. J., 2004. Defects and diffusion in Ceramics Trans Tech Publications Ltd, pages 93-95

[10] Ziegler, J.F., Ziegler, M.D. and Biersack, J.P., 2010. SRIM–The stopping and range of ions in matter (2010). *Nuclear Instruments and Methods in Physics Research Section B: Beam Interactions with Materials and Atoms*, *268*(11-12), pp.1818-1823.

[11] Jiao, L., 2015. *Enhanced Radiation Tolerance of Ceramic Thin Films by Nano-structural Design* (Doctoral dissertation).

[12] Popović, M., Novaković, M., Šiljegović, M. and Bibić, N., 2012. Effects of 200 keV argon ions irradiation on microstructural properties of titanium nitride films. *Nuclear Instruments and Methods in Physics Research Section B: Beam Interactions with Materials and Atoms*, *279*, pp.144-146

[13] Xue, J.X., Zhang, G.J., Xu, F.F., Zhang, H.B., Wang, X.G., Peng, S.M. and Long, X.G., 2013. Lattice expansion and microstructure evaluation of Ar ion-irradiated titanium nitride. *Nuclear Instruments and Methods in Physics Research Section B: Beam Interactions with Materials and Atoms*, *308*, pp.62-67.

[14] Wang, H., Araujo, R., Swadener, J.G., Wang, Y.Q., Zhang, X., Fu, E.G. and Cagin, T., 2007. Ion irradiation effects in nanocrystalline TiN coatings. *Nuclear Instruments and Methods in Physics Research Section B: Beam Interactions with Materials and Atoms*, *261*(1-2), pp.1162-1166.

.

[15] Bes, R., Millard-Pinard, N., Gavarini, S., Cardinal, S., Garnier, V., Khodja, H., Malchere, A., Martin, P. and Peaucelle, C., 2010. Study of xenon thermal migration in sintered titanium nitride using nuclear micro-probe. *Nuclear Instruments and Methods in Physics Research Section B: Beam Interactions with Materials and Atoms*, *268*(11-12), pp.1880-1883.

[16] Bès, R., Gaillard, C., Millard-Pinard, N., Gavarini, S., Martin, P., Cardinal, S., Esnouf, C., Malchere, A. and Perrat-Mabilon, A., 2013. Xenon behavior in TiN: A coupled XAS/TEM study. *Journal of nuclear materials*, *434*(1-3), pp.56-64.

[17] Malherbe, J.B., Selyshchev, P.A., Odutemowo, O.S., Theron, C.C., Njoroge, E.G., Langa, D.F. and Hlatshwayo, T.T., 2017. Diffusion of a mono-energetic implanted species with a Gaussian profile. *Nuclear Instruments and Methods in Physics Research Section B: Beam Interactions with Materials and Atoms*, *406*, pp.708-713.

Chapter seven

7. TiC results

7.1 Characterization of as-sintered TiC

TiC powder was sintered using spark plasma sintering (SPS). Some sets of the sintered TiC samples were implanted with Xe ions of 360 keV to a fluence of 1.1×10^{16} cm $^{-2}$ at room temperature (RT). Others were firstly irradiated with Xe of 167 MeV ions to a fluence of 3.4×10^{14} cm^{-2} at RT and then implanted with Xe ions of 360 keV to a fluence of 1.1×10^{16} cm^{-2} also at RT. The implanted samples were then sequentially annealed in temperatures ranging from 1100 to 1600 ^{o}C in steps of 100 ^{o}C for 5 hours. The as-sintered samples were characterized by SEM, XRD, micro-RS and XPS while irradiated and implanted then annealed samples were additionally characterized by RBS. This chapter presents and discusses the results from analysis

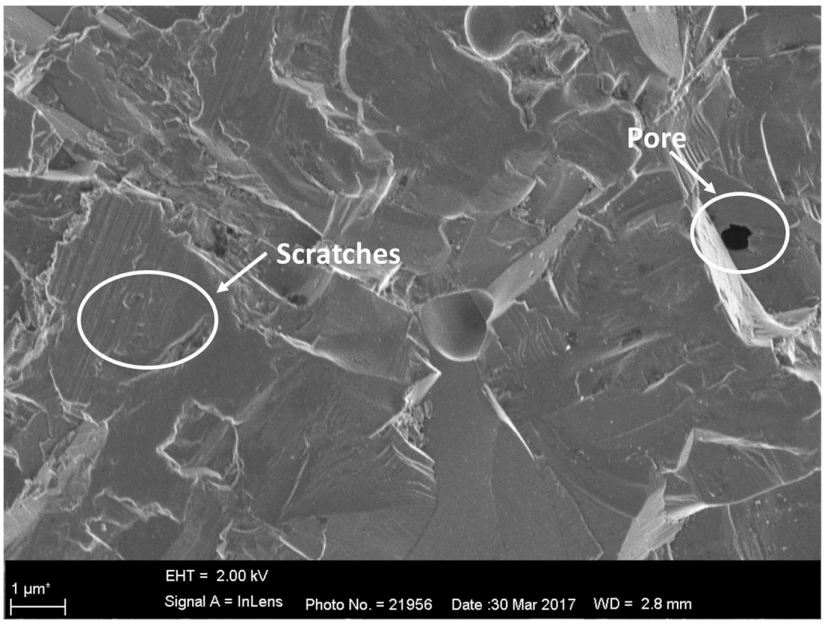

Figure 7-1: *SEM surface micrograph of the as-sintered TiC.*

Figure 7-1 shows the SEM micrograph of as-sintered TiC. There are few pores on the surface of the sintered TiC indicating maximum densification as was verified by Archimedes'

principle. A relative density of 94.5 % equivalent to 4.15 g/cm^{-3} was obtained for as-sintered TiC. Scratch marks are also visible on the samples surface owing to polishing that was performed after cutting the samples into manageable sizes.

Figure 7-2 shows the XRD pattern of the as sintered of TiC. The XRD pattern has sharp peaks at 2θ positions of 42.9, 49.9, 73.2, 88.8 and 93.8^{o} corresponding to (111), (200), (202), (311) and (222) TiC planes according to ICDD file number: 98 061 8922, indicating the polycrystalline nature of the sintered TiC. The average crystallite size of the as-sintered samples was found to be 39.0 nm using Scherrer's equation [1].

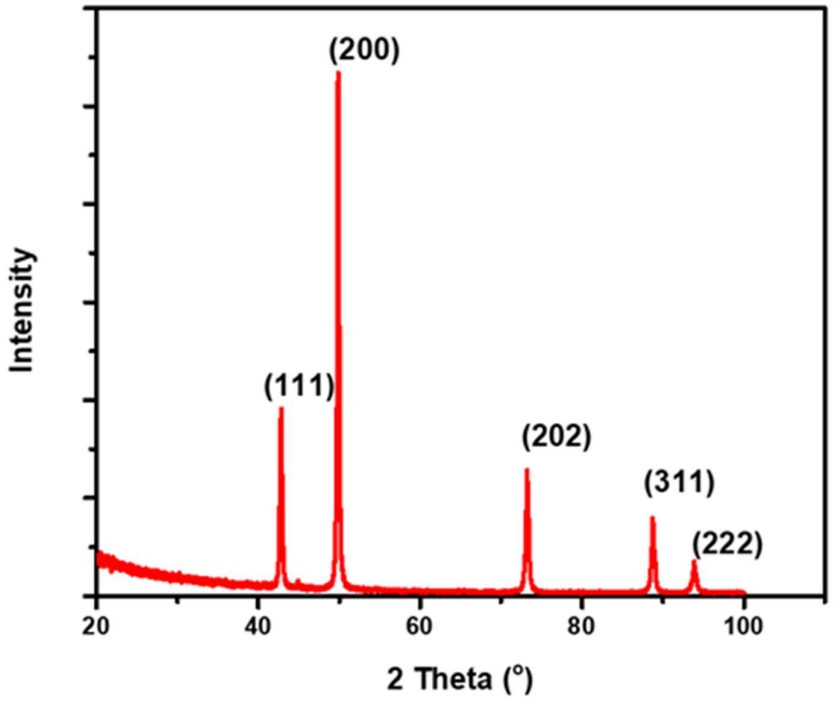

Figure 7-2: *XRD pattern of as-sintered TiC.*

The Raman spectrum of as-sintered TiC is shown in Figure 7-3 together with the fitted spectrum. The measured spectrum reveals four distinct bands at 287, 376, 573 and 669 cm^{-1}. The peaks at 287 and 376 cm^{-1} are the first order Raman scattering corresponding to longitudinal acoustic (LA) and transverse acoustic (TA) modes while the peaks at 573 cm $^{-1}$ and 669 cm^{-1} correspond to transverse optical (TO) and longitudinal optic (LO) modes

respectively. The Raman spectrum fitted well with peaks at 262, 287, 376 421, 573 and 669 cm^{-1}. The peaks at 262 and 421 cm^{-1} are atributed to tatinium oxide [2]. The acoustic modes are attributed to the vibrations of the Ti atoms while optical modes are attributted to the vibration of the C atoms. Similar to TiN, TiC has face centred cubic(fcc) NaCl structure, face-centred cubic (fcc) and undergoes octahedral symmetry (O_h). In a perfect crystall only the zone centres phonons can be Raman active, usually not even all of them. The selection rules for Raman do not allow O_h symmetry, therefore first order scattering is forbidden in TiC [3,4]. Although the first order is forbiden in TiC, the presence of defects results in the detection of the first order scattering. Hence the as-sintered TiC has defects and has oxidised. It is evident that TiC had defects due to the fact that Raman spectra had peaks. Some of the likely defects are Frenkel defects, which results due to non-stiochiometry of the ceramic (TiC). Since the samples were polished and stored in an open environment there is a possibility of adsorbed moisture that can lead to oxidation.

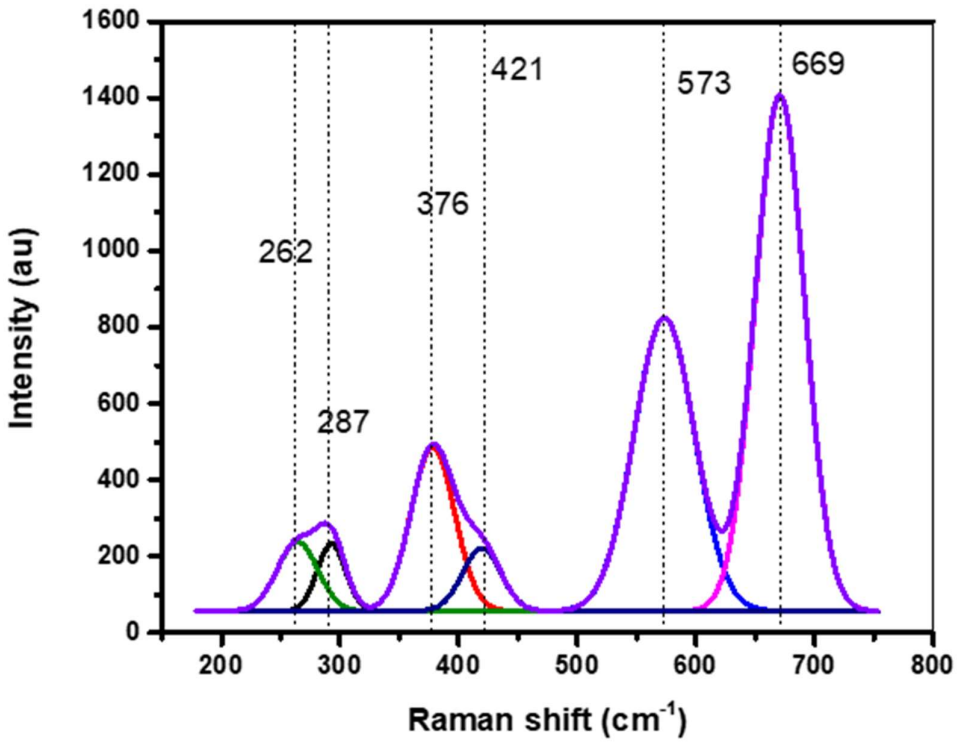

Figure 7-3: *Raman spectrum of as-sintered TiC fiited and fitted components (Lorentzian-Gaussian).*

High resolution XPS spectrum for Ti 2p shown in Figure 7-4 (a) displayed $Ti2p_{3/2}$ and $Ti2p_{1/2}$ peaks positioned at binding energies of 454.8 eV and 460.9 eV, respectively consistent with the Ti – C and Ti-O bonds [5,6]. The fitted Ti spectrum also shows only two peaks. The presence of the Ti-O bonds reveals that the surface of the samples has been oxidized. Oxidation of TiC at elevated temperatures has been reported by Shimada *et al* [7]. Figure 7-4 (b) shows the high-resolution spectrum of C 1s with a prominent peak at 281.6 eV which could be attributed to carbon bonded to Ti [6]. The remaining two peaks at 282.1 eV and 285.4 eV are attributed to carbidic carbon peaks and graphitic carbon (C-C), respectively. Other studies showed similar oxidation of TiC at elevated temperatures [6,7,8].

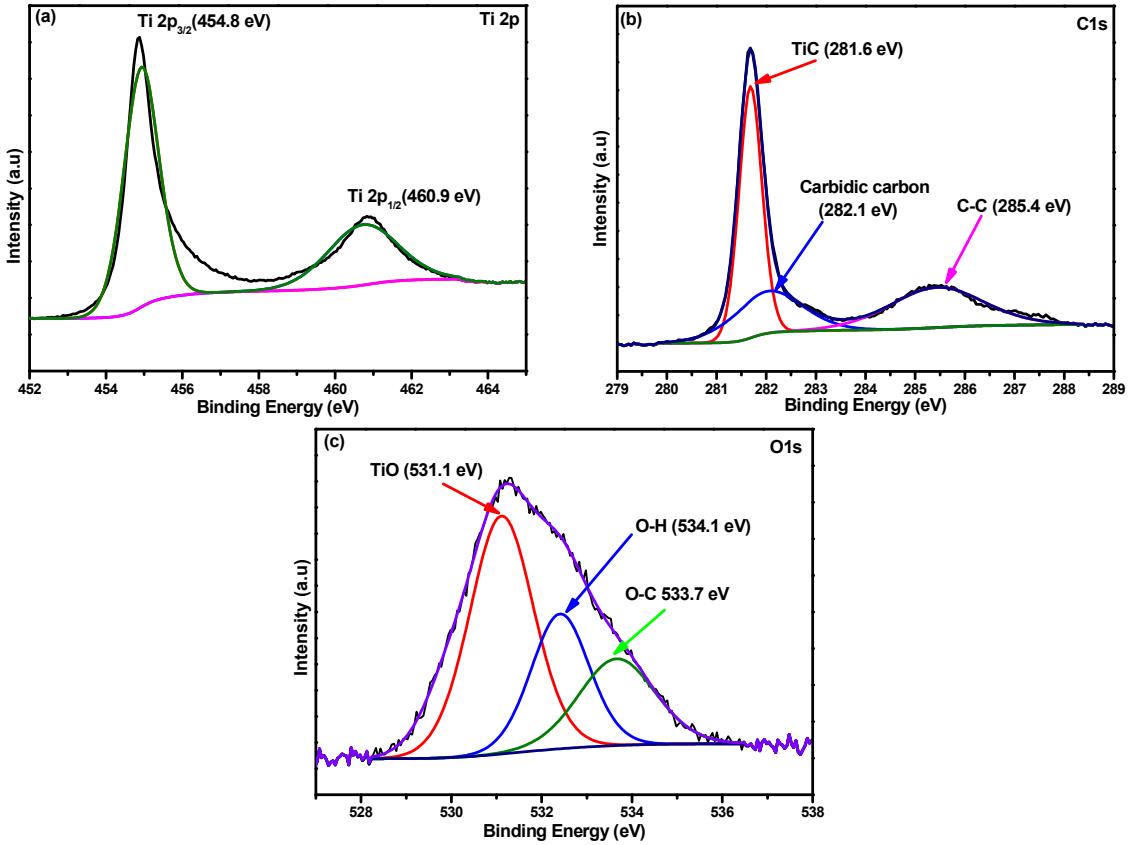

Figure 7-4: *High resolution XPS spectra of (a) Ti 2p, (b) C 1s and (c) O 1s, fitted and fitted components.*

O1s core level photoelectron was fitted into three different fragments Figure 5-16 (c): the first component at 531.1 eV is ascribed to TiO, the second component at 534.1 eV is assigned as the elemental O (or physically adsorbed molecular H_2O) and the third component at 533.7 eV is identified to be originated from O-C phase [4,8] These XPS results are consistent with Raman results that showed oxidised TiC surface.

7.2 Implantation and Irradiation of TiC

Figure 7-5 (a) shows the SRIM simulated results of Xe ions of 360 keV implanted into TiC to a fluence of 1.1×10^{16} cm^{-2} at RT and Figure 7-5 (b) Xe ions of 167 MeV irradiated into TiC to a fluence of 3.4×10^{14} cm^{-2} also at RT. The measured RBS profiles of Xe ions of 360 keV

implanted into TiC(Xe -360 keV-RT) and Xe ions of 360 keV implanted into TiC (pre-irradiated with Xe ions of 167 MeV)-Xe-360 keV-RT+SHI are also included. The fluence were converted into damage in displacement per atom (dpa) using equation 6.2 as discussed in chapter 6. The theoretical density of TiC (9.91 $\times 10^{22}$ atcm^{-3}) and the vacancy per ion from SRIM 2012 [9] were used. A "Detailed Calculations with full Damage Cascades" which follows every recoil until its energy drops below the lowest displacement energy of a target atom, was used in simulations. The threshold displacement energies of 20 and 25 eV for the C and Ti sublattices were used.

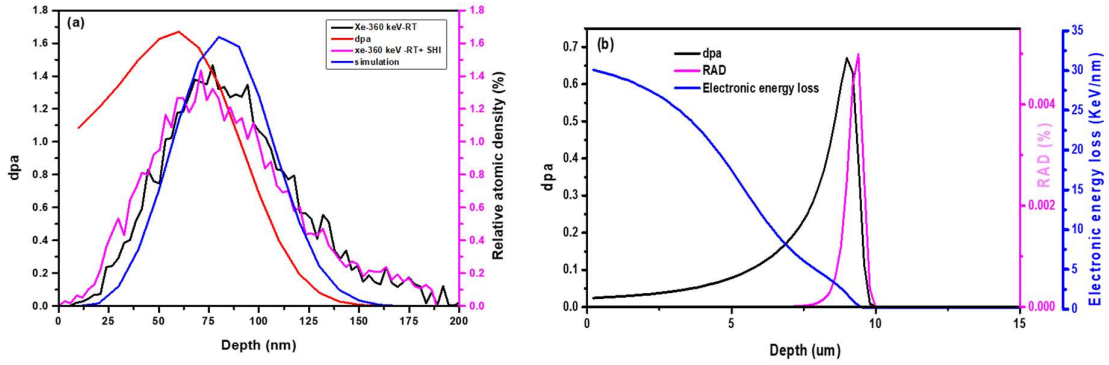

Figure 7-5: *(a) Depth profiles of Xe ions of 360 keV implanted into TiC at RT to fluence of 1.1×10^{14}cm^{-2}, Xe ions of 360 keV implanted into TiC (pre irradiated with Xe ions of 167 MeV to a fluence of 3.4×10^{14} cm^{-2}at RT) to a fluence of 1.1×10^{16} cm^{-2}at RT and SRIM simulated damage in dpa, (b) electronic energy loss and Xe profiles are included*

The measured Xe depth profiles from Xe-360 keV-RT and Xe-360keV-RT+SHI are identical and slightly broader but in reasonably agreement with SRIM simulated Xe profile. The experimental Rp of about 76.84 nm for the Xe-360 keV-RT and 85.1 nm for Xe-360keV-RT+SHI are reasonable in agreement with the simulated Rp of about 80.00 nm. From these results, it is quite clear that SHI irradiation prior to Xe implantation had insignificant effect on the distribution of implanted Xe. The maximum retained damage in dpa is closer to the surface

as compared to projected range. Low energy Xe ions exposed the surface to nuclear energy loss resulting in a maximum dpa of about 1.70 at 50.0 nm while SHIs exposed the surface to electronic energy loss of 30 keV/nm at the surface resulting to about 0.62 dpa at 9.10 um- Figure 7-5 (b). Therefore, the interaction of the defects retained by low energy ions (during implantation- Xe 360 keV) and defects retained by both low energy ions and SHIs is expected in the Xe-360 keV-RT+SHI.

Figure 7-6 shows the Raman spectra of Xe-360 keV-RT+SHI and Xe-360 keV-RT. Raman spectrum of pristine or virgin TiC is included in Figure 7-6 for comparison. Both treatments resulted to a slight combination of the peaks in the 280 to 380 cm^{-1} region accompanied by the broadening of the optical bands with all Raman characteristic TiC peaks still present indicating accumulation of concentration of defects in the samples without amorphization. To get more insight on the defects retained in both the samples, the Raman spectra of both the samples were fitted using Lorentzian-Gaussian profile.

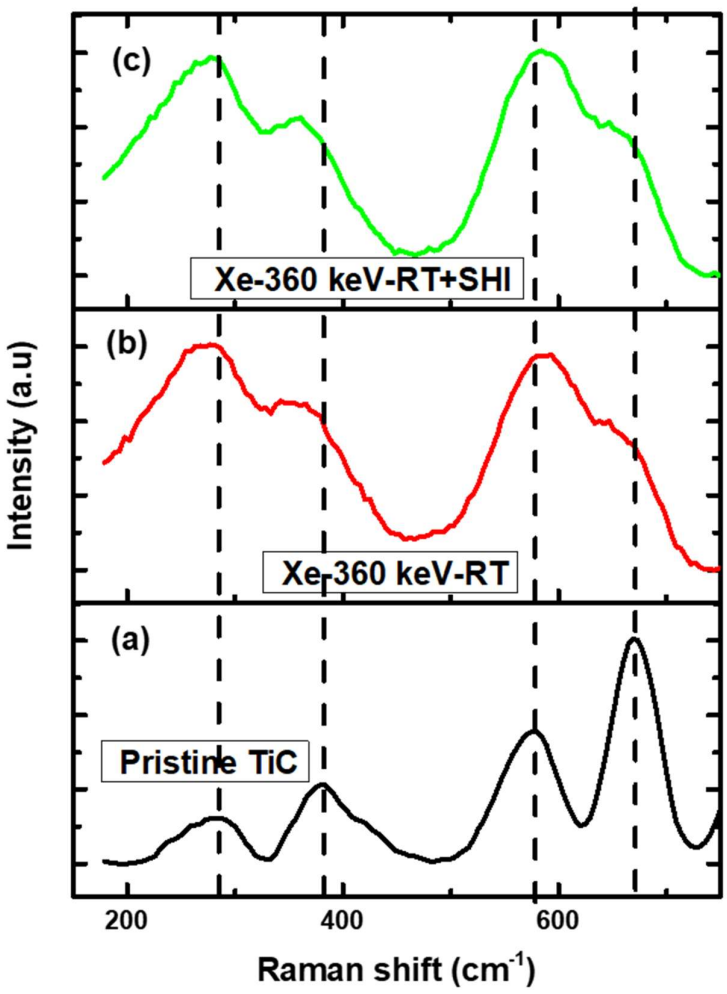

Figure 7-6: *Raman spectra of (a) as-sintered TiC (b) TiC implanted with Xe of 360 keV to a fluence of 1.1×10^{16} cm^{-2} at RT (Xe-360 keV-RT) and (c) co-irradiated with Xe of 167 MeV to a fluence of 3.4×10^{14} cm^{-2} and then implanted with Xe ions of 360 keV to a fluence of 1.1×10^{16} cm^{-2} respectively (Xe-360 keV-RT+ SHI).*

Figure 7-7 (a) shows the fitted and measured Raman spectra of Xe-360 keV-RT and (b) the fitted and measured Raman spectra of Xe-360 keV-RT+SHI. Both treatments caused an increase in peak intensities of the acoustic and the optical accompanied by a slight combination of the TA and LA, TO and LO. The shifting of TA, LA and LO mode to lower wavenumbers and TO shifting to higher wavenumbers were also observed. These results indicate the accumulation of defects without amorphization in both samples. Similar accumulation of

vacancies/defects concentration without amorphization has been reported in TiC irradiated with Au ions of 1.2 MeV at several fluences, even at the highest fluence of 7×10^{15} cm^{-2} that was lack of amorphization [4].

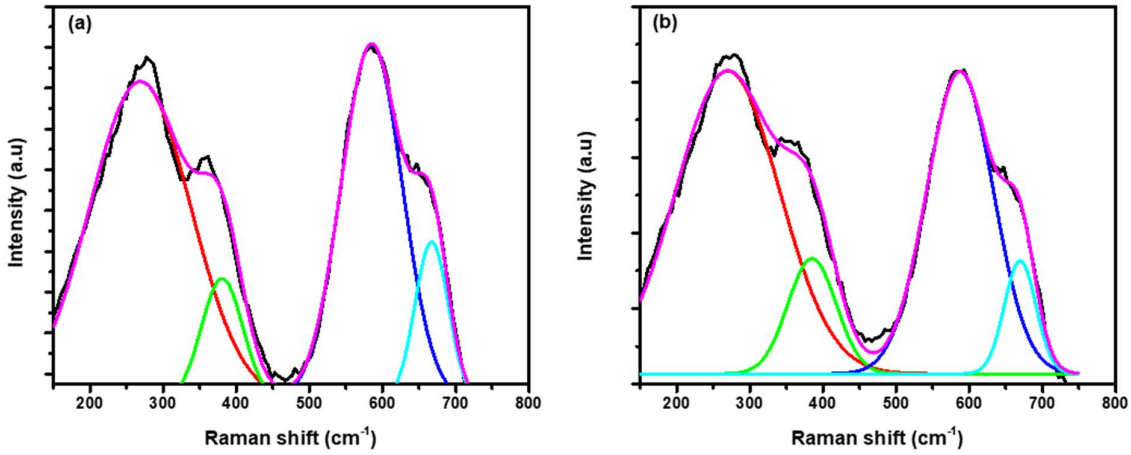

Figure 7-7: *(a) Raman Spectrum of sintered TiC implanted with Xe-360 keV to a fluence of $1.1\times10^{16}cm^{-2}$at RT (Xe-360 keV-RT), fitted and fitted components (Lorentzian- Gaussian) and (b) The Raman spectrum of sintered TiC firstly irradiated with 167 MeV Xe ions to a fluence of $3.4\times10^{14}cm^{-2}$ then implanted by Xe ions of 360 keV to fluence of $1.1\times10^{16}cm^{-2}$ at RT(Xe-360 keV-RT+SHI), fitted and fitted components (Lorentzian-Gaussian).*

The fitted peaks also showed a similar trend of shifting to lower wavenumbers while the TO shifted to the higher wavenumbers. These differences in peak shifts either to lower or higher wavenumbers indicate the different stress in the samples. Furthermore, the LA/LO ratio was used to quantify the defects retained in the samples as suggested in [10]. The ratio is proportional to the concentration of vacancies/defects [3]. The full width at half maximum (FWHM) of the TO mode peaks were calculated from the deconvoluted spectra. Both LA/LO ratio and FWHM (TO) are shown in Table 7-1. Both ratio and FWMH suggested relatively the same amount of defects concentration in both Xe-360 keV-RT and Xe-360 keV-RT+SHI. As explained earlier in Chapter 6.2, SHIs interactions with matter are more complex and owing to their penetration depth into the sample their effect may not be easily observed. Moreover, S_e

dominates with very insignificant alteration of the target material. However, SHIs may contribute to defect creation and defect annealing due to thermal heating during irradiation. All these make the whole process more complex, more investigations are needed to understand the processes at play.

Table 7-1: *LA/LO ratio of Pristine, as-implanted and implanted then annealed up to 1600 °C.*

Sample	LA/LO	FWMH(TO)
Pristine	0.40	65
Xe-360 keV-RT	1.16	105
Xe-360 keV-RT +SHI	1.15	105
Xe-360 keV-RT-1600 °C	0.57	103
Xe-360 keV-RT+SHI-1600 °C	0.58	103

Figure 7-8 (a) shows the SEM surface micrograph of as-sintered TiC, there are scratches due to polishing of the samples. The scratch marks that were visible in the pristine samples are not visible in the Xe-360 keV-RT samples as seen in Figure 7-8(b). This could be due to sputtering of the samples' surface during implantation. Figure 7-8 (c) shows the micrograph of the Xe-360 keV- RT+SHI sample. Crystallites and cracks are visible on the surface. The visible cracks and formation of crystallites on the surface can be attributed to the heating effect during SHI irradiation prior to implantation and also mechanical polishing during cleaning of the samples. The similarities in morphology of as-implanted, irradiated then implanted and as- sintered TiC further indicate the lack of amorphization after treatments. Similar lack of amorphization in implanted TiC has been reported in TiC implanted with 500 keV argon and 800 keV xenon ions to fluences more than 6.0×10^{16} cm^{-2} [11].

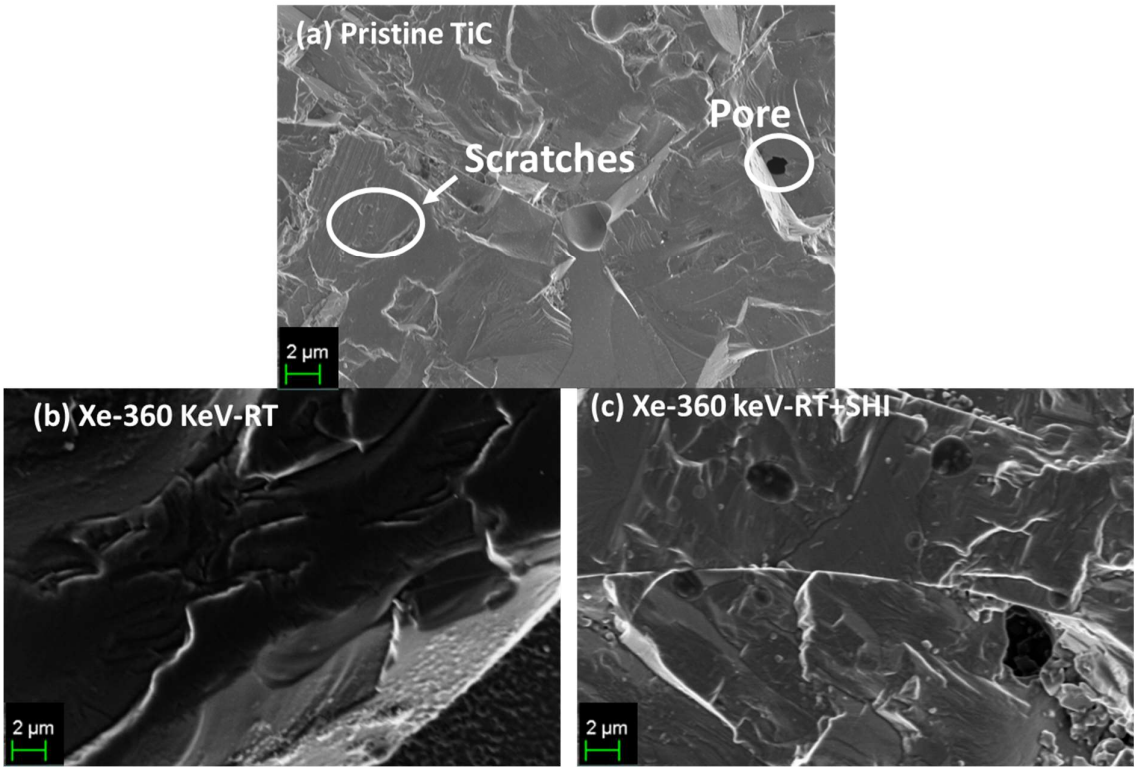

Figure 7-8: *SEM micrographs of (a) as-sintered TiC, (b) Xe-360 keV-RT and (c) Xe-360 keV-RT+SHI.*

7.3 Annealing of as-implanted and irradiated then implanted TiC

Figure 7-9 shows the Raman spectra together with the fitted spectra of *(a)* Xe-360 keV- RT after sequentially annealed up to 1600 °C and (b) Xe-360 keV-RT+SHI after sequentially annealed up to1600 °C. Table 7-2 shows the experimental peak positions while Table 7-3 shows their corresponding fitted peak positions obtained using the Gaussian-Lorentzian function.

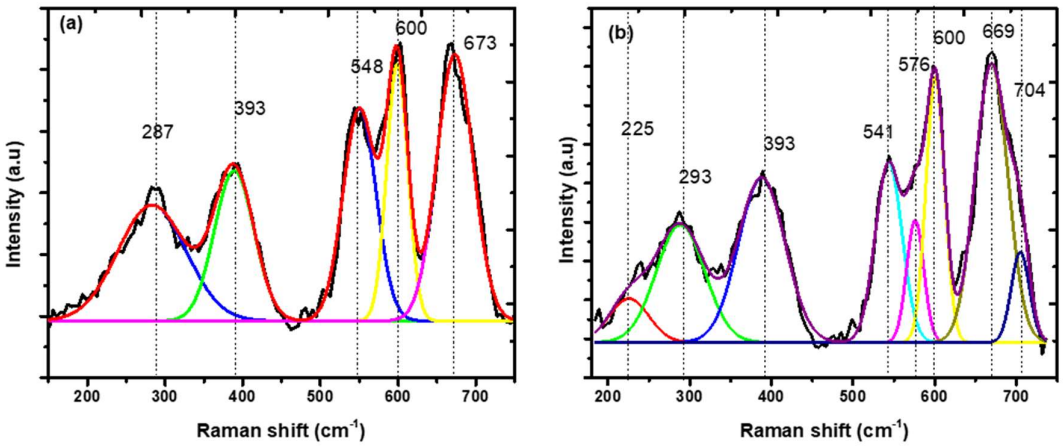

Figure 7-9: *Raman spectra of (a) Xe-360 keV-RT with fitted components after sequentially annealing up to 1600 °C (b) Xe-360 keV-RT+SHI with fitted components after sequentially annealing up to 1600 °C.*

Table 7-2: *Experimental Raman peaks for all the samples (TiC).*

Sample ID	**TA (cm^{-1})**	**LA (cm^{-1})**	**TO (cm^{-1})**	**LO (cm^{-1})**
Pristine-TiC	284	380	577	671
Xe-360 keV-RT	277	351	584	646
Xe-360 keV-RT+SHI	277	351	592	647
Xe-360 keV RT - 1600 °C	287	393	548, 600	673
Xe-360 keV-RT+SHI-1600 °C	293	393	541, 600	669

Table 7-3: *Summary of the fitted Raman peaks for all samples (TiC).*

Sample ID	**TA (cm^{-1})**	**LA (cm^{-1})**	**TO (cm^{-1})**	**LO (cm^{-1})**
Pristine (TiC)	262,287	376,421	573	669
Xe-360 keV-RT	287	393	548,600	669,704
Xe-360 keV-RT+SHI	293	393	595	673
Xe-360 keV-RT - 1600 °C	287	393	548,600	673
Xe-360 keV RT+SHI-1600 °C	225,293	393	541,576,600	669,704

Sequential annealing up to 1600 °C resulted in the decrease in the peak intensities of the TA and LA modes accompanied by a shift to higher frequency of the TA, LA, and LO mode while the TO mode shifted to lower frequency and composed of more than one peak for both samples. Similar patterns were observed in the fitted spectra. The TO mode of Xe-360 keV-RT+SHI sequentially annealed up to 1600 °C samples composed of three peaks while the TO mode of Xe-360 keV-RT sequentially annealed up to 1600 °C composed of two peaks. These results indicate the reduction in defects concentration after sequentially annealing resulting in TiC with different stoichiometry compared to the as-sintered TiC. Klein *et al* showed that TiC of different stoichiometry have different Raman spectra [3]. The annealing of defects in both

samples after sequentially annealing up 1600 ºC was also observed from the reduction in the LA/LO ratios of the annealed samples in Table 7-1.

Figure 7-10 shows the SEM surface micrographs of Xe-360 keV-RT and Xe-360 keV-RT+SHI after being isochronally annealed from 1400 to 1600 °C in steps of 100 °C for 5 hours. The Xe-360 keV-RT and Xe-360 keV-RT+SHI micrographs are included for comparison.

Both the as- implanted and annealed TiC samples in Figure 7-10 are composed of homogenous, brighter, and darker regions. The homogenous regions are crystals while the brighter and darker regions are grain boundaries and pores, respectively. Both implanted (Figure 7-10 (a) and (b)) and the annealed (Figure 7-10 (c) to (h)) have SEM micrographs with relatively similar features as in the as-sintered samples (Figure 7-8 (a)-(b)). However, the as-sintered has sharp edges and rough surfaces, while the annealed samples are smoother. Similar features on the as-sintered, as-implanted and annealed indicate that the TiC is resilient to irradiation and recovery from irradiation.

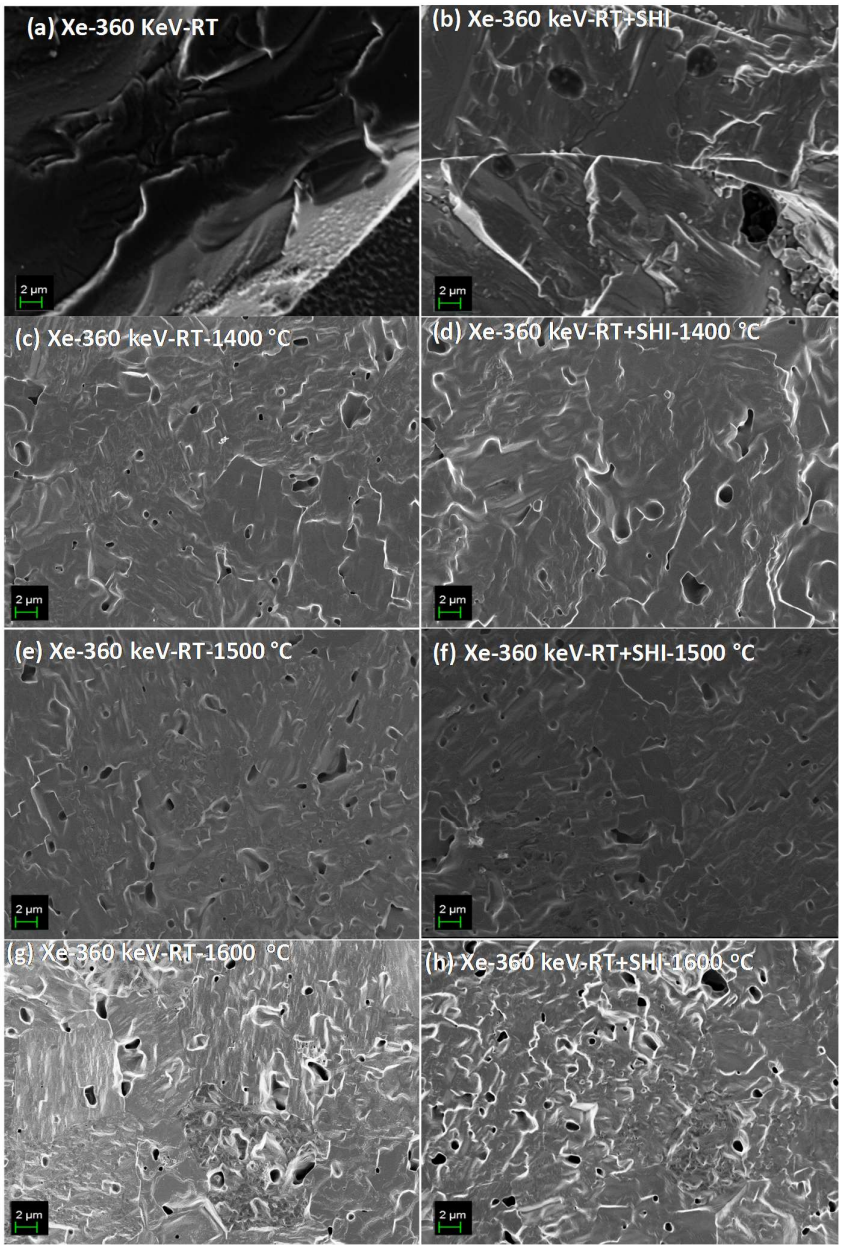

Figure 7-10: *SEM micrographs of (a) Xe-360 keV-RT, (b) Xe-360 keV-RT+SHI after isochronally being annealed at 1400 to 1600 °C (Figures 7-10 (c)-(h)) in steps of 100 °C for 5 hours cycles.*

The migration behavior of implanted Xe was monitored using RBS after each annealing cycle. Figure 7-11 (a) shows the depth profiles of the Xe implanted into sintered TiC at RT to a fluence of 1.1×10^{16} cm^{-2}after sequentially annealed at temperatures from 1100 up to 1600 °C in steps of 100 °C for 5 hours. The as-implanted depth profile is included for comparison. The retained ratios calculated as the ratio of area of Xe counts after annealing to that of as-implanted and squares of the full width at half maximum as a function of annealing temperature are shown in Figure 7-11 (b) and (c) respectively. Annealing at 1100 °C caused slight broadening of the FWHM (Figure 7-11(c) accompanied by no loss of implanted Xe. Annealing at 1200 °C caused the Xe profile to slightly shift towards the bulk accompanied by broadening and no loss of Implanted Xe indicating diffusion of implanted Xe towards the bulk during annealing at this temperature. Annealing at 1300 °C caused migration of Xe towards the surface accompanied by further broadening and loss of about 25% of implanted Xe. These results indicate the diffusion towards the surface resulting in the loss of Xe from the surface after annealing at 1300 °C. Additional loss of implanted Xe accompanied by broadening of the Xe profile was observed after annealing at 1400 °C. Further annealing resulted in further loss of Xe without broadening. About 70% was lost after annealing at 1600 °C.

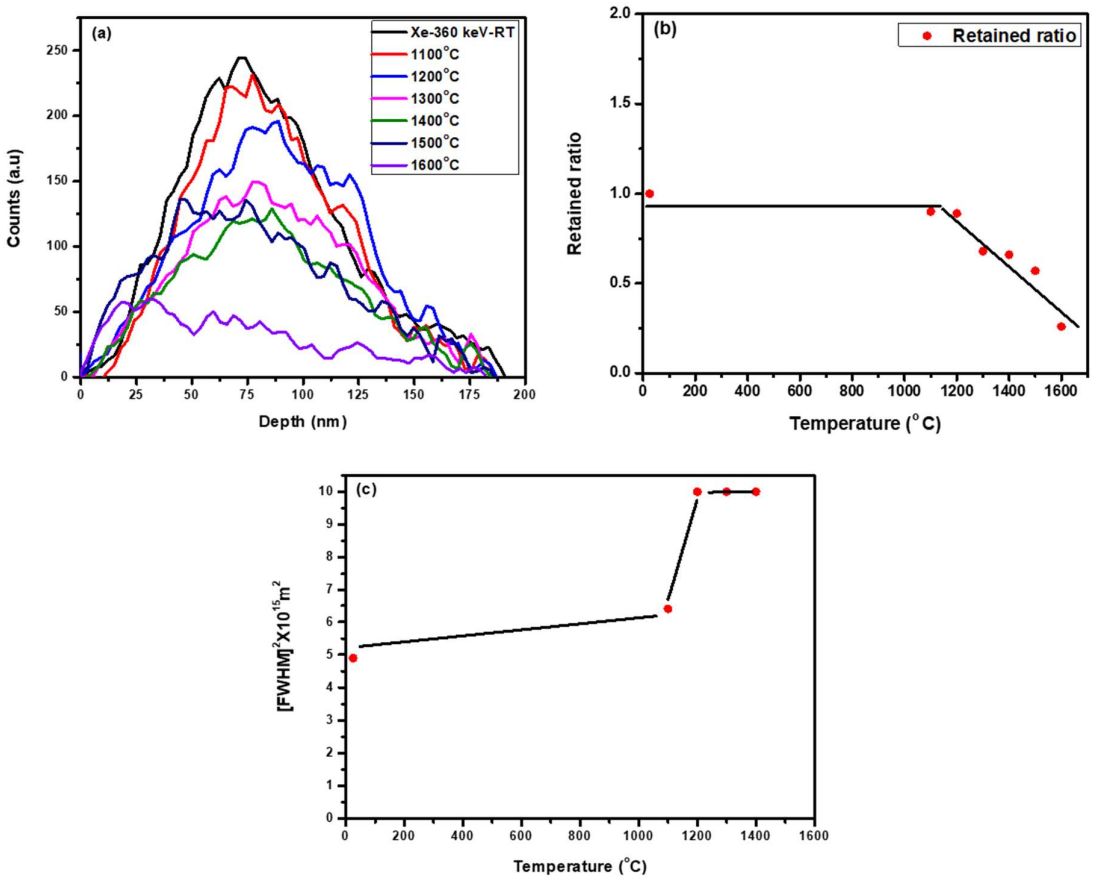

Figure 7-11: (*a) Depth profiles of the Xe of 360 keV implanted into TiC at RT to a fluence of* 1×10^{16} *cm*$^{-2}$ *then sequentially annealed from 1100 up to 1600 °C in steps of 100 for 5 hours, (b) retained ratio of Xe implanted into TiC and (c) the square of the FWHM as a function of annealing temperature.*

Figure 7-12 shows the results of Xe-360 keV-RT+SHI sequentially annealed up to 1600 ºC. Annealing the Xe-360 keV-RT+SHI samples at 1100 ºC resulted in no broadening of implanted Xe. However, the implanted Xe slightly moved towards the surface resulting in the loss of about 25 % of implanted Xe. The broadening accompanied by loss began after annealing at 1200 ºC and progressed with annealing temperature. About 60 % was lost after annealing at 1600 ºC and the Xe peak became truncated indicating direct release of implanted Xe.

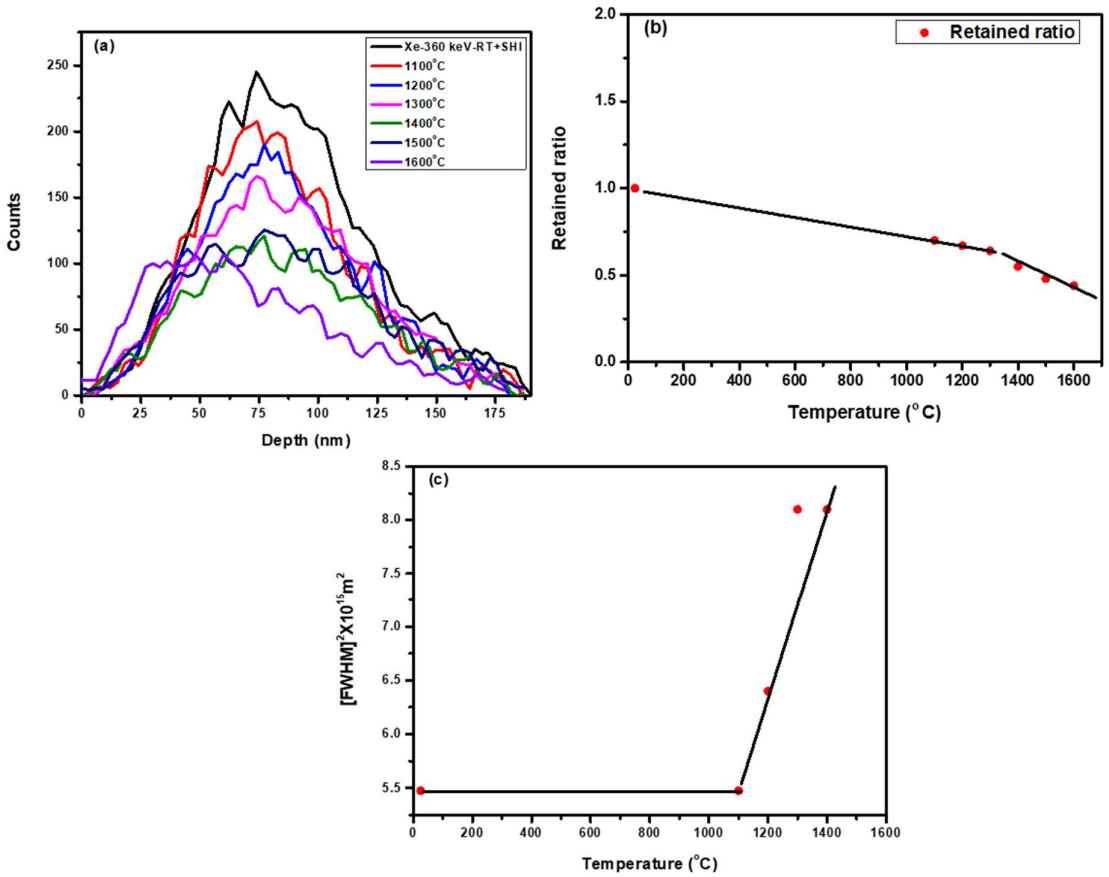

Figure 7-12: *(a) Depth profiles of Xe (360 keV) implanted into TiC (pre-irradiated with Xe ions of 167 MeV to a fluence of 3.4×10^{14} cm^{-2} at RT) to a fluence of 1.1×10^{16} cm^{-2} at RT then sequentially annealing from 1100 up to 1600 °C in steps of 100 for 5 hours. and (b) the retained ratios of implanted Xe and (c)squares of the FWHM as a function of annealing temperature.*

A slight change at 1100 ºC, shifting of implanted Xe towards the bulk accompanied by broadening after annealing the Xe-360 keV-RT samples at 1200 ºC suggests that the Xe was initially trapped by the radiation damage as more defects were retained near the surface and minimum defects were retained in the undamaged-damaged interface. Annealing of defects should be more enhanced in the interface where there are less defects. On the other hand, Xe migration requires a particular level of defects. In the Xe-360 keV-RT samples the level of defects is higher than the level required for migration of Xe. Annealing at 1100 °C led to some

annealing of defects preferable more on the interface but to a level that is more than the one that allow diffusion. Further annealing at 1200 ºC resulted in annealing of defects to a level enough to allow diffusion only in the interface thus resulting in the migration towards the bulk. Annealing most of the surface defects to a minimum defects concentration that allows migration of Xe occurred after annealing at 1300 ºC which led to the migration of implanted Xe towards the surface.This migration of implanted Xe progressed with increasing annealing temperature up to 1600 °C in Xe-360 keV-RT.

The migration of implanted Xe in Xe-360 keV-RT+SHI samples is different in Xe-360 keV-RT samples. Annealing the Xe-360 keV-RT+SHI at 1100 ºC resulted in the loss of implanted Xe accompanied by no broadening. If the migration of Xe is assisted by the level of defects concentration, then defects concentration in these samples are enough for migration to takes place. This migration accompanied by loss progressed with temperature and was accompanied by broadening after annealing at temperatures greater than 1100 ºC. From these results it is quite clear that the defects retained in the Xe-360 keV-RT samples initially are enough to trap implanted Xe while in Xe-360 keV-RT+SHI the retained defects are at the level that allows the migration of Xe. This might be due to the interaction of the defects retained by SHIs and slow ions in the latter samples. Annealing at 1300 °C resulted in the migration of implanted Xe towards the surface as more defects were annealed out. This was accompanied by the loss which might be due to direct release from the surface and pores that were observed on SEM micrographs. The pores might have resulted in lack of broadening owing to fast loss of implanted Xe.

Similar to the TiN studies, the diffusion coefficients (D) of Xe in Xe-360 keV-RT and Xe-360 keV-RT+SHI samples were determined by fitting the depth profiles to a solution of the Fickian diffusion equation for an initially Gaussian profile [13]. The program fits experimental depth profiles to the solution of the Fickian diffusion equation with an originally Gaussian profile

and a perfect sink at the surface [13]. An example of the fitted Xe profile is shown in the Figure 7-13. The diffusion coefficients of 1.16×10^{-20}, 1.44×10^{-20},1.83×10^{-20} and 5.56×10^{-20} m^2s^{-1} at 1200, 1300, 1400 and 1500 ^oC respectively were determined for Xe-360 keV-RT samples while the diffusion coefficients of 7.92×10^{-21}, 1.44×10^{-20}, 2.59×10^{-20} m^2s^{-1} at 1400, 1500 and 1600 ^oC respectively were determined for Xe-360 keV-RT+SHI. From the Arrhenius plots shown in Figure 7-14(a) and (b) activation energy of 1.4 eV and pre-exponential factor (D_o) of 5.2×10-17 m^2s^{-1} were obtained for Xe-360 keV-RT and 1.6 eV and 5.2×10^{-16} m^2s^{-1} for Xe-360 keV-RT+SHI.

The difference in activation energy in the two samples indicate a slightly different mechanism governing the diffusion of Xe in Xe-360 keV-RT samples and in Xe-360-RT+SHI samples.

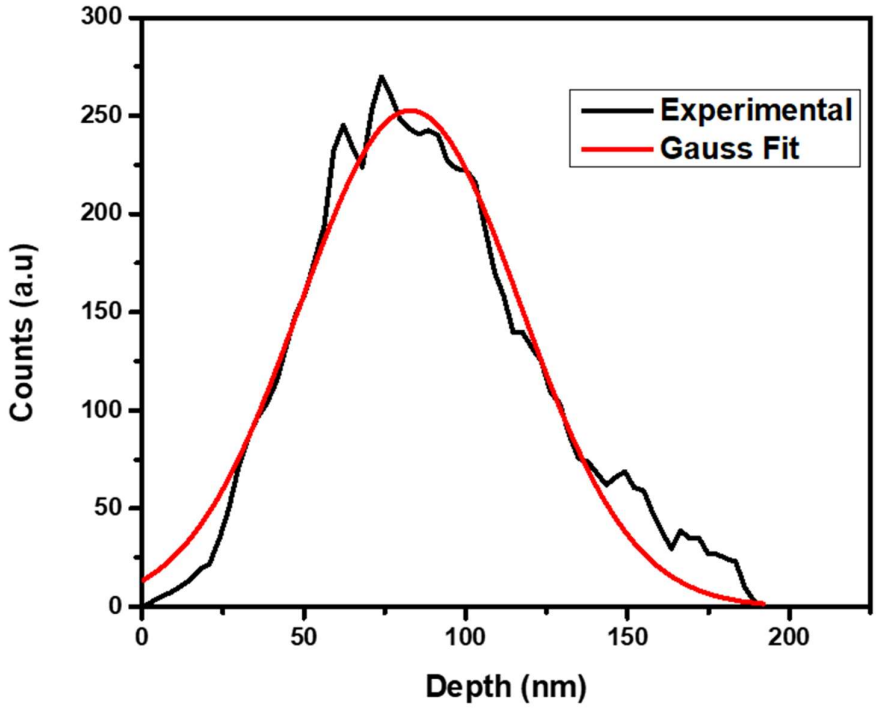

Figure 7-13: *The MATLAB program fitted to Xe-360 keV-RT- TiC sample after implantation.*

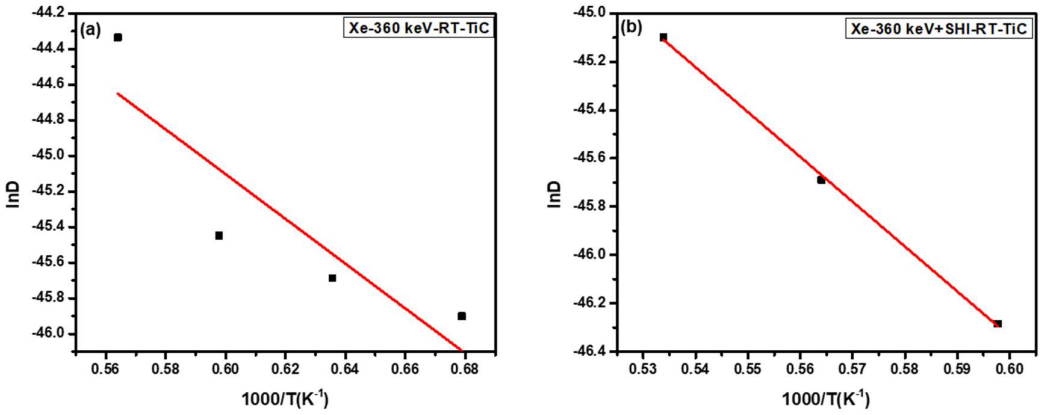

Figure 7-14: *the plot of lnD versus 1/T(K^{-1}) to calculate D_0 and E_a for (a) Xe-360 keV-RT and Xe-360 keV RT +SHI-. The plot was fitted to a linear equation.*

7.4 References

[1] Cullity, B. D., and Stock, S. R., 1978. Principles of X-ray diffraction. Rading, MA: Addison-Wesley, pp. 90-95.

[2] Barshilia, H.C. and Rajam, K.S., 2004. Raman spectroscopy studies on the thermal stability of TiN, CrN, TiAlN coatings and nanolayered TiN/CrN, TiAlN/CrN multilayer coatings. *Journal of Materials Research*, *19*(11), pp.3196-3205.

[3] Klein, M.V., Holy, J.A. and Williams, W.S., 1978. Raman scattering induced by carbon vacancies in Ti C_x. *Physical Review B*, *17*(4), p.1546.

[4] Pellegrino, S., Thomé, L., Debelle, A., Miro, S. and Trocellier, P., 2014. Radiation effects in carbides: TiC and ZrC versus SiC. *Nuclear Instruments and Methods in Physics Research Section B: Beam Interactions with Materials and Atoms*, *327*, pp.103-107.

[5] Bertoti, I., Mohai, M., Sullivan, J.L. and Saied, S.O., 1995. Surface characterisation of plasma-nitrided titanium: an XPS study. *Applied surface science*, *84*(4), pp.357-371.

[6] Krzanowski, J.E. and Leuchtner, R.E., 1997. Chemical, Mechanical, and Tribological Properties of Pulsed□Laser□Deposited Titanium Carbide and Vanadium Carbide. *Journal of the American Ceramic Society*, *80*(5), pp.1277-1280.

[7] Shimada, S., 1996. A thermoanalytical study of oxidation of TiC by simultaneous TGA-DTA-MS analysis. *Journal of materials science*, *31*(3), pp.673-677.

[8] Zhang, L. and Koka, R.V., 1998. A study on the oxidation and carbon diffusion of TiC in alumina–titanium carbide ceramics using XPS and Raman spectroscopy. *Materials chemistry and physics*, *57*(1), pp.23-32.

[9] Ziegler, J.F., Ziegler, M.D. and Biersack, J.P., 2010. SRIM–The stopping and range of ions in matter (2010). *Nuclear Instruments and Methods in Physics Research Section B:*

Beam Interactions with Materials and Atoms, *268*(11-12), pp.1818-1823.

[10] Gavarini, S., Millard-Pinard, N., Garnier, V., Gherrab, M., Baillet, J., Dernoncourt, L., Peaucelle, C., Jaurand, X. and Douillard, T., 2015. Elaboration and behavior under extreme irradiation conditions of nano-and micro-structured TiC. *Nuclear Instruments and Methods in Physics Research Section B: Beam Interactions with Materials and Atoms*, *356*, pp.114-128.

[11] Pellegrino, S., Trocellier, P., Thomé, L., Miro, S., Costantini, J.M. and Jouanny, E., 2019. Raman investigation of ion irradiated TiC and ZrC. *Nuclear Instruments and Methods in Physics Research Section B: Beam Interactions with Materials and Atoms*, *454*, pp.61-67.

[12] Gavarini, S., Bes, R., Millard-Pinard, N., Cardinal, S., Peaucelle, C., Perrat-Mabilon, A., Garnier, V. and Gaillard, C., 2011. A comparative study of TiN and TiC: Oxidation resistance and retention of xenon at high temperature and under degraded vacuum. *Journal of Applied Physics*, *109*(1), p.014906.

[13] Malherbe, J.B., Selyshchev, P.A., Odutemowo, O.S., Theron, C.C., Njoroge, E.G., Langa, D.F. and Hlatshwayo, T.T., 2017. Diffusion of a mono-energetic implanted species with a Gaussian profile. *Nuclear Instruments and Methods in Physics Research Section B: Beam Interactions with Materials and Atoms*, *406*, pp.708-713.

Chapter eight

8. Conclusions and future studies

In this work, TiN and TiC powders were successfully sintered using SPS at 1900 ºC. RS, XPS and XRD analysis for both TiN and TiC revealed polycrystalline structures with structural defects and oxidized surfaces.

For TiN samples SEM showed uniform surface having few pores confirming densification, which agrees well with the obtained density of 5.31 gcm^{-3} compared to theoretical density of 5.39 gm^{-3}. Some of the as-sintered samples were implanted with Xe ions of 360 keV at RT to a fluence of 1.1×10^{16} cm^{-2}, while others were first irradiated with Xe ions of 167 MeV to a fluence of 3.4×10^{14} cm^{-2} at RT then implanted with Xe ions of 360 keV to a fluence of 1.1×10^{16} cm^{-2} also at RT. Both treatments resulted in the increase in intensity Raman peaks accompanied by slight combination of TA and LA modes indicating accumulation of defect concentration. This accumulation of defects was more pronounced in the implanted samples. Sequential annealing of both samples resulted in annealing of defects. This annealing of defects was enhanced in the irradiated then implanted samples compared to the implanted samples. Furthermore, grain boundaries with crystallites were observed in the annealed samples and were more pronounced on the irradiated then implanted samples.

Migration of implanted Xe was governed by trapping and de-trapping of implanted Xe through defects in the implanted samples annealed at the temperatures below 1200 °C and was mainly through grain boundary diffusion towards the surface accompanied by loss at temperatures above 1200 ºC. About 90% of implanted Xe was lost after annealing at 1500 °C. In the irradiated then implanted samples, the migration of Xe was mainly via fast grain boundary diffusion towards the surface accompanied by a loss in all annealing temperatures. Almost all implanted Xe was lost after annealing at 1600 °C. Therefore, defects concentration and structure of TiN are vital in the migration of implanted Xe. The diffusion coefficients of

1.90×10^{-21}, 6.21×10^{-21}, 51×10^{-21} and 1.25×10^{-20} m^2s^{-1} at 1100, 1200, 1300, and 1400 °C were determined in the implanted samples while the diffusion coefficients were below the detection limit in the irradiated then implanted samples. From these diffusion coefficients the activation energy of Ea = $(2.2 \pm 0.5) \times 10^{-19}$ J = 1.4 eV and pre-exponential factor of $D_o = (1.4 \pm 0.5) \times 10^{-16}$ m^2/s were determined.

SEM micrographs of as-sintered TiC samples showed uniform surface having few pores confirming densification, which agrees well with the obtained density of 4.31 g/cm^{-3}. Some of the samples were implanted with Xe ions of 360 keV at RT to a fluence of 1.1×10^{16} cm^{-2}, while others were first irradiated with Xe ions of 167 MeV at RT at a fluence of 3.4×10^{14} cm^{-2} then implanted with Xe ions of 360 keV. RS results showed a slight combination of the TA and LA modes and increase intensity indicating the accumulation of defects with no amorphization in both samples. Sequential annealing of both samples up to 1600 °C caused a progressive healing of defects resulting to a TiC structure that is different from the as-sintered TiC.

The migration of implanted Xe was governed by trapping and de-trapping of implanted Xe through defects in the implanted samples at annealing temperature below 1200 °C and a fast grain boundary diffusion towards the surface accompanied by loss at temperatures above 1200 °C. About 75% of implanted Xe was lost after annealing at 1600 °C. In the irradiated then implanted samples, the migration of implanted Xe was due to grain boundary diffusion towards the surface accompanied by the loss throughout the annealing process. About 60% of implanted Xe was lost after annealing at 1600 °C. The diffusion coefficients of 1.16×10^{-20}, 1.44×10^{-20},1.83×10^{-20} and 5.56×10^{-20} m^2s^{-1} at 1200, 1300, 1400 and 1500 ^oC respectively were determined for implanted samples while the diffusion coefficients of 7.92×10^{-21},1.44×10^{-20}, 2.59×10^{-20} m^2s^{-1} at 1400, 1500 and 1600 ^oC respectively were determined for irradiated then implanted samples. From these diffusion coefficients, an activation energy of 1.4 eV and pre-exponential factor (D_o) of 5.2×10^{-17} m^2s^{-1} were obtained for implanted samples while 1.6 eV

and 5.2×10^{-16} m^2s^{-1} were obtained for irradiated then implanted samples.

Comparing TiN and TiC results, it is quite clear that these two ceramics are more radiation tolerant compared to other nuclear ceramics such as SiC, which is advantageous for nuclear systems applications. However, TiC seems to be retaining more implanted Xe up to 1600 °C which is an added advantage compared to TiN and SiC. More investigation needs to be undertaken to attest to these findings.

8.1 Future work

Even though the presented results are promising for the use of TiN/TiC in nuclear reactor systems, further investigations in the migration of Xe in TiN/TiC need to be undertaken to validate these findings. These includes but not limited to structural investigation of the treated samples with the state-of-the-art equipment like transmission electron microscope (TEM). This will also allow the investigation on the migration behavior of Xe in an atomic scale. Isochronal annealing at different temperatures need to be investigated to compare with the sequential annealing presented this thesis. The latter will give more insight in the role of radiation damage in the migration behavior of implanted Xe. Since in nuclear reactors, TiN/TiC will be exposed to excessive alpha irradiation, the migration of Xe in the presence of alpha particles need to be investigated.